RARE-EARTH ION DOPED DIELECTRIC WAVEGUIDE AMPLIFIER DEVICES

Doctor of Philosophy Thesis

Mustafa DEMİRTAŞ

Eskişehir 2019

RARE-EARTH ION DOPED DIELECTRIC WAVEGUIDE AMPLIFIER DEVICES

Mustafa DEMİRTAŞ

DOCTOR OF PHILOSOPHY THESIS

Department of Electrical and Electronics Engineering
Supervisor: Assoc. Prof. Dr. Feridun AY

Eskişehir
Anadolu University
Institute of Graduate Programs
October 2019

This work was supported by the Scientific and Technological Research Council of Turkey (TÜBİTAK), project number 114E594 and University Scientific Research Project Council (BAP), project no BAP1606F569.

FINAL APPROVAL FOR THESIS

This thesis titled "**Rare-earth Ion Doped Dielectric Waveguide Amplifier Devices**" has been prepared and submitted by **Mustafa Demirtaş** in partial fulfillment of the requirements in "Anadolu University Directive on Graduate Education and Examination" for the Degree of Doctor of Philosophy (PhD) in **Electrical and Electronics Engineering** Department has been examined and approved on 10/04/2019.

Committee Members		**Title, Name and Surname**	**Signature**
Member (Supervisor)	:	Assoc. Prof. Dr. Feridun AY	……..
Member	:	Prof. Dr. Cem SEVİK	……..
Member	:	Assoc. Prof. Dr. Nihan KOSKU PERKGÖZ	……..
Member	:	Assoc. Prof. Dr. Serkan ATEŞ	……..
Member	:	Assist. Prof. Dr. Faruk DİRİSAĞLIK	……..

Prof. Dr. Murat TANIŞLI
Director
Institute of Graduate Programs

ÖZET

NADİR TOPRAK İYON KATKILI DİELEKTRİK DALGA KILAVUZU YÜKSELTEÇ AYGITLAR

Mustafa DEMİRTAŞ

Elektrik ve Elektronik Mühendisliği Anabilim Dalı
Anadolu Üniversitesi, Lisansüstü Eğitim Enstitüsü, Ekim 2019

Danışman: Doç. Dr. Feridun AY

Bu tez, aktif entegre optik devrelerde erbiyum katkılı Al_2O_3 düzlemsel dalga kılavuzları uygulamateknolojilerinin geliştirilmesine odaklanmıştır. Al_2O_3 katmanlar, düşük kayıp için başarıyla optimize edilmiş; 1.55 μm'de şu ana kadar 0.04±0.02 dB/cm olarak bildirilen en düşük kayıp değerlerinden biri elde edilmiştir. Erbiyum katkılı Al_2O_3 filmlerinin Atomik Katman Kaplama cihazı kullanılarak büyütülmesi için yöntem geliştirilmiştir. Aynı büyütme parametreleri kullanılarak erbiyum konsantrasyonunun tekrarlanabilirliği, yüksek kaliteli filmler elde edilmesi ve cihazlar için standart silikon alttaşlar üzerine geniş bir alanda yüksek film homojenliği elde edilmesi hedeflenmiştir. Erbiyum, $Er(thd)_3$ ve O_2 plazma öncülleri kullanılarak Al_2O_3 katmanları arasına Er_2O_3 yapısında katkılanmıştır. Maksimum %2.29 atomik konsantrasyon değerine sahip farklı konsantrasyonlarda Erbiyum katkılı örnekler elde edilmiştir. Filmlerin karakterizasyonunda X-ışını Fotoelektron Spektroskopisi, elipsometre ve μRaman kullanılmıştır. Filmlerin derinlik profili de araştırılmıştır. Tepe tipi dalgakılavuzları üretiminde %85 H_3PO_4 kullanılarak yeni bir yöntem ortaya konulmuştur. Elde edilen dalga kılavuzlarının yapısal özellikleri, düzgün yan duvarlar, iyi desen çözünürlüğü ve uygun tepe tipi dalga kılavuzu özellikleri yeterli eşme derinliklerinin elde edilmesi için irdelenmiştir. C-bandındaki optik kazancı ve ömrü ölçmek için özgün ölçüm düzenekleri kurulmuştur. %1.18 Erbiyum konsantrasyon değerine sahip dalgakılavuzlarında 4.38±0.31 ms'lik kabul edilebilir ışık ömrü ölçülmüş ve aynı aygıtta literatürdeki birim uzunluk başına en yüksek optik kazanç değeri olan 13.72 dB/cm elde edilmiştir.

Anahtar Kelimeler: Tümleşik optik, Pasif/aktif dalga kılavuzları, Atomik Katman Kaplama, Al_2O_3, Er_2O_3, XPS, μRaman, Profilometre, Elipsometre, Fotolüminesans, Ömür süresi, Optik kayıp, Optik kazanç

ABSTRACT

RARE-EARTH ION DOPED DIELECTRIC WAVEGUIDE AMPLIFIER DEVICES

Mustafa DEMİRTAŞ

Department of Electrical and Electronics Engineering

Anadolu University, Institute of Graduate Programs, October 2019

Supervisor: Assoc. Prof. Dr. Feridun AY

This thesis focuses on development of fabrication technologies for Erbium-doped Al_2O_3 waveguides application for active integrated optical devices. The Al_2O_3 host layers were successfully optimized, resulting in one of the lowest loss values reported so far with a value 0.04±0.02 dB/cm at 1.55 μm. A novel procedure for deposition of Erbium-doped Al_2O_3 films by ALD was developed. The investigation concentrated on the repeatability of erbium concentration using identical deposition parameters, growing films of high quality and achieving excellent film uniformity over a large area on standard silicon substrates in order to have a large available area for devices. Erbium was successfully incorporated into the low-loss Al_2O_3 by ALD using $Er(thd)_3$ and O_2 plasma, resulting in atomic concentrations of up to 2.29 percent. X-ray Photoelectron Spectroscopy, ellipsometry and μRaman were used to analyze the films. The depth profile analysis of the films was also carried out. A new method for etching ridge waveguides by applying 85% H_3PO_4 was used. The structural properties of the resulting waveguides were investigated, with an emphasis on obtaining smooth sidewalls, good pattern resolution and sufficient etch depths for appropriate ridge waveguide properties. In order to validate these results, new experimental setups were realized to measure the optical gain and lifetime at C-band. For the current process, acceptable luminescence lifetimes of 4.38±0.31 ms obtained for waveguides with Er-concentrations of 1.18 atomic percent, and the highest reported optical gain per unit length of 13.72 dB/cm was demonstrated.

Keywords: Integrated optics, Passive/active waveguides, Atomic layer deposition, Al_2O_3, Er_2O_3, XPS, μRaman, Profilometer, Ellipsometer, Photoluminescence, Lifetime, Optical loss, Optical gain

STATEMENT OF COMPLIANCE WITH ETHICAL PRINCIPLES AND RULES

I hereby truthfully declare that this thesis is an original work prepared by me; that I have behaved in accordance with the scientific ethical principles and rules throughout the stages of preparation, data collection, analysis and presentation of my work; that I have cited the sources of all the data and information that could be obtained within the scope of this study, and included these sources in the references section; and that this study has been scanned for plagiarism with "scientific plagiarism detection program" used by Anadolu University, and that "it does not have any plagiarism" whatsoever. I also declare that, if a case contrary to my declaration is detected in my work at any time, I hereby express my consent to all the ethical and legal consequences that are involved.

……

Mustafa DEMİRTAŞ

ACKNOWLEDGMENTS

First and foremost I would like to thank my supervisor Assoc. Prof. Dr. Feridun Ay for providing me with the opportunity to study in this field and complete my Ph.D. work. I am extremely grateful for many discussions which helped guide me in the right direction, his motivating attitude, his availability as a supervisor and his many insightful suggestions.

I would also like to thank Micro/Nano Devices and Systems (MIDAS) Research Group members for their help.

Most importantly I would also like to thank my family for their encouragement and support.

Last but not least, I would also like to thank my wife who is Gökben for her love that has been invaluable for me.

Mustafa DEMİRTAŞ

October 2019

CONTENTS

LIST OF FIGURES

LIST OF TABLES

LIST OF ABBREVIATIONS

ALD	: Atomic Layer Deposition
CVD	: Chemical Vapor Deposition
CR	: Cross-relaxation
DRAM	: Dynamic Random Access Memory
ETU	: Energy Transfer Upconversion
ESA	: Excited State Absorption
FET	: Field Effect Transistor
GSA	: Ground State Absorption
MOSFET	: Metal Oxide Field Effect Transistor
PEALD	: Plasma Enhanced Atomic Layer Deposition
PECVD	: Plasma Enhanced Chemical Vapor Deposition
REE	: Rare Earth Element
tALD	: Thermal Atomic Layer Deposition
TIR	: Total Internal Reflection
PL	: Photoluminescence
SNR	: Signal to Noise Ratio
TE	: Transverse Electric
TM	: Transverse Magnetic
TRPL	: Time Resolved Photoluminescence
XPS	: X-ray Photoelectron Spectroscopy

1. INTRODUCTION

1.1. Integrated Optics

Electron-based technology, electronic devices, has started to confront many limitations in the mid-20th century. Composed of the Si element (silicon), semiconductors are now used as input to develop and produce the two devices in a particular size. Downsizing of transistors is constrained by an absolute lower limit caused by the elemental quantity. This factor also inhibits the acceleration of electrical signals on inter- and intra-movement for both devices. On the other hand, optical technologies are offering many new possibilities that can solve many of the problems that electronics encounter. The use of optics has become widespread especially after lenses, filters and other components for aiding vision began to be developed [1]. Then, optical methods have come to be applied not only to the visible but also extensively to the invisible spectrum such as X-rays, ultraviolet, infrared and microwaves. The need to use more than one optical component in the same circuit and the field of integrated optics has emerged. Basically, the integrated optic is built with the primary objective of developing and embedding as many miniaturized, compact, high-speed, light-weight and low-powered optical devices on a flat rigid substrate as of the 1980s [2]. Integrated optics consist of micro-scale optical sources, waveguides, resonators, modulators, wires, splitters, couplers and interferometers on chips or on modular boards to perform different functions like sensing, switching, modulating, processing, transporting and routing of optical signals.

1.2. Integrated Optical Waveguides

Integrated optics' main building blocks are waveguides, which are the basic component of any optical circuit that connects different optical systems. Basically, an optical waveguide consists of multilayered planar structures parallel to one another [3]. To build an effective waveguide, high light confinement is compulsory. Light propagation must satisfy Total Internal Reflection, or TIR, which is the reflection of the total amount of incident light at the boundary between two media [3]. Light tends to confine in the highest refractive index layer in one dimension known as the guiding layer. The cover or cladding layer is placed on top of the guiding layer, and the substrate layer is below the guiding layer. Light will be degraded by attenuation and dispersion while it propagates through a material.

1.2.1. Waveguide Modes

A waveguide works at different velocities for each or all phases and has ways of cross-sectional intensity distribution and polarization. In a waveguide mode typical with an invariant transversal intensity profile and an effective refractive index n_{eff} the propagation of electromagnetic waves occurs through the device. The phase velocity rate can be defined as $^{c}/_{n_{eff}}$, where c is the light speed in vacuum. With this, you may identify the resistance capacity of the optical power to entrapment into its core.

As we have no ability to quantify modes, it is useful to make a hypothetical prediction, and for this imagine an only two-dimensional waveguide with step indices and an incident coherent light while the wave normal sets an angle with the normal to the interface, denoted as θ (see Figure 1.1). There will critically become different angles for the interface, $\theta_c = \sin^{-1}\left(^{n_c}/_{n_f}\right)$ above and $\theta_s = \sin^{-1}\left(^{n_s}/_{n_f}\right)$ below, $n_s < n_c$ [3, 4].

(1) Guided modes ($\theta_s<\theta<90°$): These optical modes have higher effective index than the largest cladding index. Its alternating reciprocal reflections between both interfaces have an impediment effect on the wave movement.

(2) Substrate radiation modes ($\theta_c<\theta<\theta_s$): These are the optical modes with lower effective index. The radiation contributes to the transfer of part of its optical power to the cladding sections. The overall reflection of an optical wave to the upper interface allows for an incident wave from the core to refract at the lower side, or one from the substrate.

(3) Substrate-cover radiation modes ($\theta<\theta_c$): There occurs no overall reflection but the refraction at the upper or the lower. The transverse journey of the incident wave through infinity starts from the two sides of the waveguide.

(4) Evanescent modes: The field impairment realizes with an exponential function across the z-axis. Radiating energy follows a transverse trajectory from the lossless waveguide.

Formation of which waveguide mode is based on its dimensions. They are mostly compatible with the two separate polarization modes, whether the field component is predominantly magnetic (TM) or electric (TE) across the transversal plane. As chosen in a great number of operations, reducing those factors down to the basic mode produces a single mode to acquire radiation exposure, regardless of polarization. [3, 4].

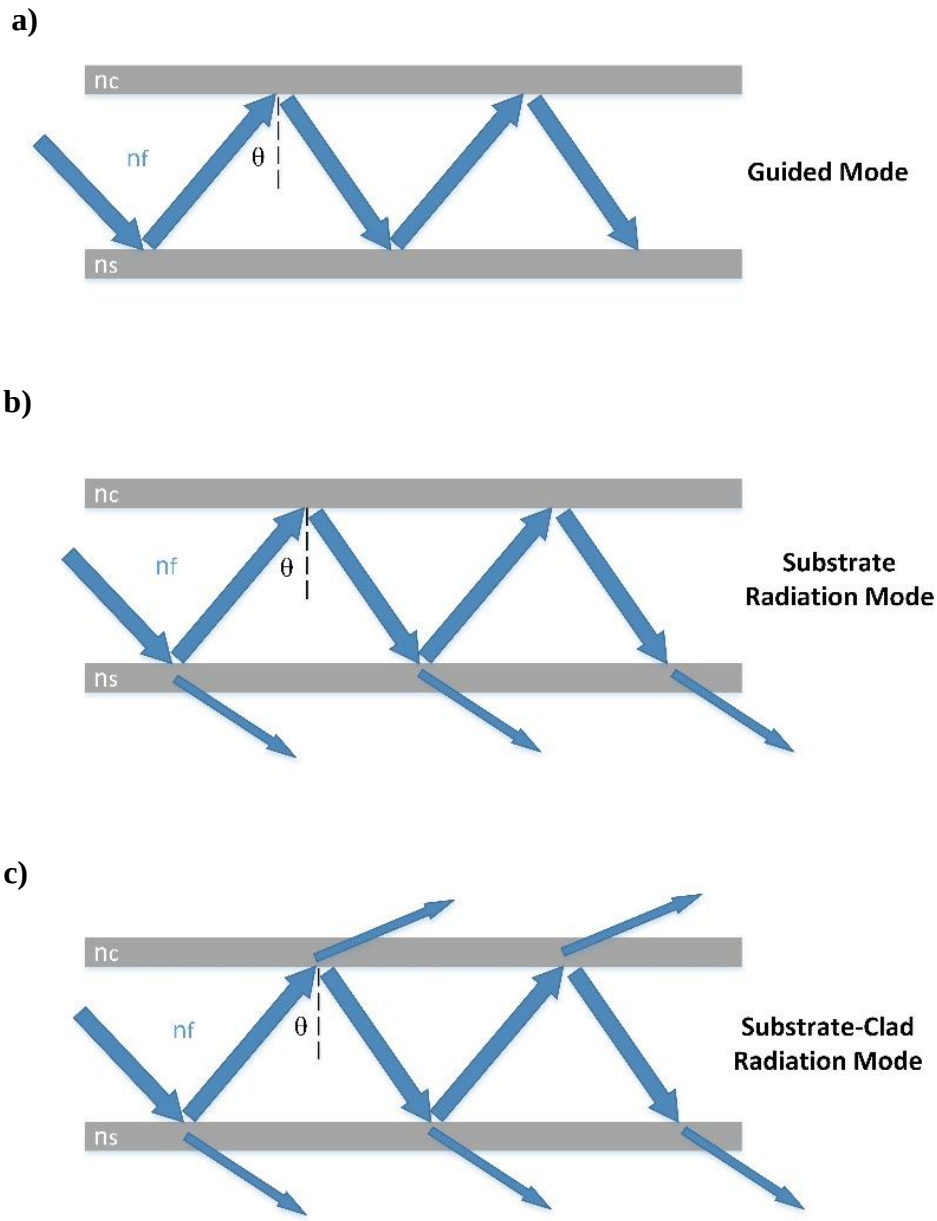

Figure 1.1. *Optical modes propagating in an optical waveguide (adapted from [4]).*

Light propagates in any mode, results in varied performance and provides different applications. When the waveguide mode is monolithic, a single light mode instantly goes through the device because of its guiding layer. Unlike multi-mode operation, this is favorable thanks to less deficiency and better signal stretch needed for farther routes. Nevertheless, its installation is less efficient as well as its expensive connectors for a single-mode, whereas a multi-mode waveguide is further capable of data transmission in that the traveling light in a higher quantity is potential due to its hugely greater breadth [3, 5].

1.2.2. Optical Losses in Waveguides

Scattering, absorbing or radiating light photons is observable with the advancement of the optical beam through the waveguide, declining the overall power transmission. For the case of absorption, their elimination is experienced losing their energy in favor of the absorbing material, that's its atoms or subatomic particles (often electrons). For the other cases, those simply shift direction in traveling without identity loss, maybe with alteration in their energy (e.g. Raman scattering). On the other hand, the overall energy decreases in transmission because the scattering of radiation allows for photons to separate from the optical beam.

Waveguides have major losses in different situations including scattering, absorption, and radiation. For an optical device, volume scattering or surface scattering produces inefficiency. Voids, contaminant atoms, and crystalline defects are found within its volume, leading to volume scattering loss per unit length proportional to the number of such imperfections or scattering centers. [1].

Surface scattering for higher-order modes, in particular, may significantly damage even if the waveguide surface is smoother due to its strong interaction with the waves. Absorption typically causes trivial losses in amorphous thin films and crystalline ferroelectric materials, with the absence of contaminant atoms and however significant losses in semiconductors for types of interband or band edge and free carrier. In a waveguide mode, the encircling media collects the photons that emit during radiation and remain out of the guidance, which can eliminate optical energy. When we confined modes are far from the cutoff, there becomes little energy loss whereas total energy is delivered to substrate radiation modes at cutoff. To determine the energy losses for waveguiding, we supply a certain optical power from one end of the device and quantify the output power at the other end. The measurement units are decibel per medium length (dB/cm, dB/km, etc.), and the transmission equation has loss coefficient equal to the slope of the curve (corresponding to length),

$$\alpha = \frac{\ln\left({}^{P_1}/_{P_2}\right)}{(d_2 - d_1)},\ for\ \ d_2 > d_1 \tag{1.1}$$

where P_1 and P_2 are the transmitted power for waveguides of two different lengths d_1 and d_2.

1.2.3. Waveguide Types

With material configurations, optical waveguides can be geometrically designed in two types [6]. By its planar geometry slab waveguides let light move only transversely. These are advantageous because of simple setup and lack of scattering between the modes of transverse and lateral wave guidance [7] (Figure 1.2a). As for channel waveguides, we see 2D optical confinement and functionality as a tube through which the light is guided. As seen in Fig. 1.2b-g, these may have a variety of configurations [8]. A buried waveguide placed on the substrate is fully encircled by the cladding material, which may spoil sensitivity of a biosensor even if it is appropriate for light guidance. The diffused waveguide has the high-index substrate area in which ions are exchanged, or dopants (i.e. Ti) are diffused so that the film boundaries are blurred [9]. For a strip-loaded waveguide that can make the transverse optical confinement, a dielectric or metal strip is used to install a planar waveguide in order to promote the lateral one. The strip has a section of the film to waveguide underneath, where the film and the strip should be equal in width. In addition, the film shields hinder its suitability for biosensors [10]. A ridge waveguide is structurally similar to the strip waveguide except that the ridge is itself used as a film to waveguide itself. These devices are encircled by low-index material on three sides (air, substrate, or cladding) and has a strong optical confinement. When it comes to a rib waveguide, the refractive index and the high index planar layers are the same under the strip or the ridge as a part of the waveguiding film.

The field of optical planar waveguide biosensors includes popular topics of the ridge and rib waveguides [11]. Instead of the rib waveguide, we can use the Anti-Resonant Reflecting Optical Waveguide (ARROW) for waveguiding in the rib because of overall reflection at the air film inside and greatness of anti-resonant reflection (>99.9%) from the impediment cladding layers, acting as Fabry-Perot resonators with their own anti-resonant wavelengths. The waveguide film is separated from the substrate on these devices that effectively behave as a single-mode waveguide. The modes are graded by loss amounts, and the higher order modes opt as the ARROWs show lower losses for the basic mode, for which thicker films are loaded, parameter tolerance higher in fabrication, and energy losses lower, unlike the overall internal reflection waveguides [12, 13].

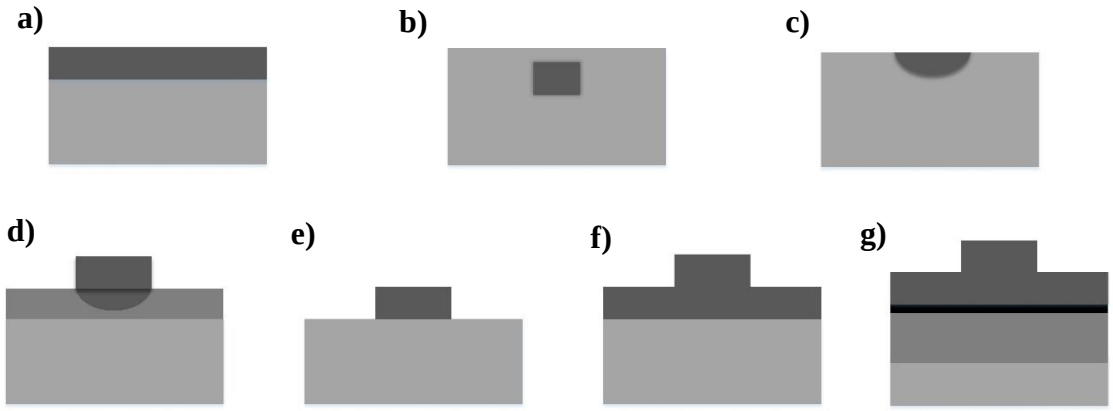

Figure 1.2. *Representation of different waveguide types a) slab b) buried c) diffused d) strip-loaded e) ridge f) rib g) ARROW waveguide*

The refractive index profile is used for classification, and the slab and channel waveguides fall into the categories of step-index, graded index, and photonic crystal waveguides. A step-index waveguide is the refractive index abruptly changing between the waveguide film and the cladding, and a graded-index waveguide refers to the refractive index has gradual changes smoothly transitioning to the cover or the substrate. For step-index waveguides, Ta_2O_5, TiO_2, Si_3N_4, Al_2O_3 or SiON are commonly utilized to create the thin layer whose refractive index is high [14, 15]. Light and heavy ions can be inputted into the production of graded-index waveguides using the methods of photolithography, etching and ion exchange together. Femtosecond laser pulses make the glass product of good quality graded-index waveguides [16, 17]. Step-index waveguides have better conditions for guidance with formation of highly discriminated refractive indices, optimal evanescent field distribution, and then better sensitivity than graded-index waveguides [18]. Refractive index variations in step-index and graded-index waveguides are presented in Figure 1.3.

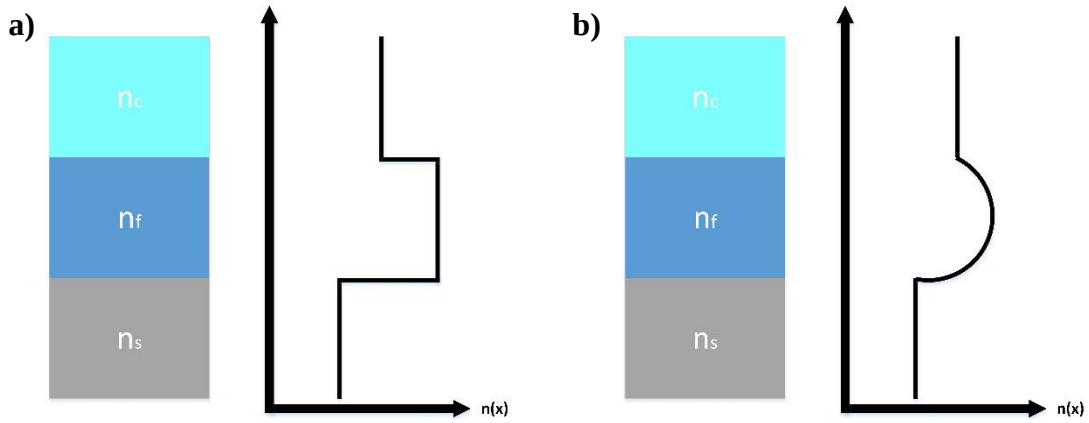

Figure 1.3. *Index variations in waveguides a) step-index b) graded-index*

A wide range of materials like silicon, silica glass, some metal oxides, semiconductors, and polymers have been used to provide propagation in optical waveguides. Polymer materials do not have sufficient reliability and thermal stability for long periods. In semiconductor waveguides, propagation losses are relatively high in comparison to others because of its crystalline structure [3, 5]. A dielectric material has some advantages like isotropic structure, low cost and is an excellent host for rare earth dopants.

1.3. Optical Amplification

The optical amplification process is a phenomenon that is based on the interaction between light and matter. This process is explained by two main steps: light absorption and light emission. In the light absorption mechanism, an electron on the lower energy level absorbs the energy of a photon and moves to an upper energy level. The energy absorbed here is the difference between the two energy levels. Light emission can occur in two different forms which are spontaneous or stimulated [19]. These can occur either consecutively or simultaneously. In spontaneous emission, the electrons that rise to the upper energy level by absorbing light (excited electron) lose their energy by converting into photons moving in a random direction. This emission does not directly contribute to light amplification, but it can indirectly contribute to different emission mechanisms like up-conversion. In stimulated emission, the excited electron stimulated by another photon which has the energy of the difference between the lower and upper energy level. As a result of this excitation, the excited electron emits another photon with the same energy, direction, and phase as the photon that stimulates it as it passes to the lower energy level.

Stimulated emission can only occur for incoming photons that have photon energy close to the energy difference of the upper and lower energy level [19]. Therefore, light amplification occurs only for optical wavelengths within a limited bandwidth. The schematic illustration of the mechanism of absorptions and emissions is given in Figure 1.4.

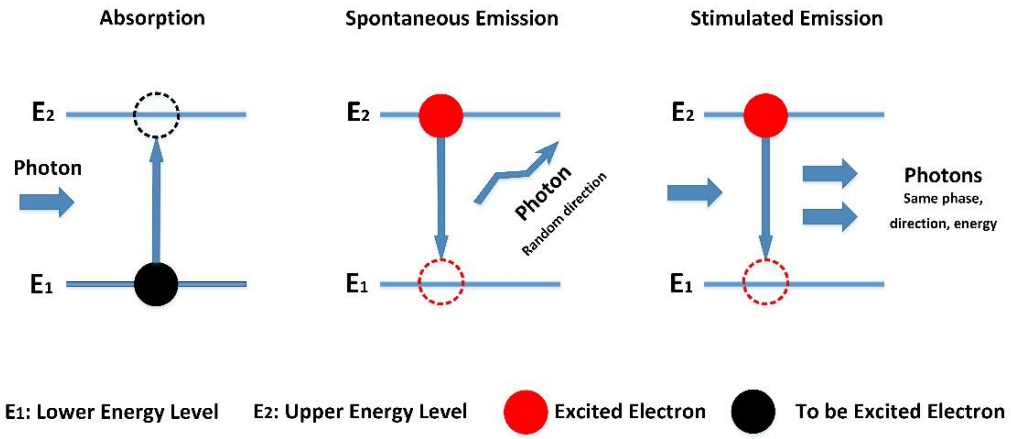

Figure 1.4. *Schematic illustration of light absorption, spontaneous emission, and stimulated emission*

The stimulated emission mechanism in Figure 1.4 shows the 2-level photon amplification process. In the 2-level system proposed, the amplification of light occurs when the stimulated emission rate exceeds the light absorption rate. This occurs when the number of upper level atoms is higher than the number of lower level atoms. It is known as population inversion. It is understood that such a mechanism cannot provide light amplification or gain, because the number of excited atoms is half of the total number of the electrons in the system [20]. This is due to the fact that, if the number of atoms on the upper level is equal to the number of atoms on the lower level. It may be concluded that the possibility of light absorption and the probability of the stimulated emission decrease to half. That is, when the atom is excited to the upper level, the chance of releasing an electron from the upper level is equally likely [21]. Therefore, most lasers and optical amplifiers operate using 3- or 4-level configurations.

1.4. Designing an Optical Waveguide Amplifiers

Basically, an optical amplifier is used to compensate for optical losses, one of the biggest problems of optical devices [19]. In integrated optics applications, there are three types of optical waveguide amplifiers that can be used to amplify light which are rare-

earth doped amplifiers, semiconductor amplifiers and Raman amplifiers [22]. However, one of them is much more effective than the others, which is rare-earth doped amplifiers, because rare-earth elements (REEs) possess unique optical properties [23]. Rare-earth doped elements are therefore of most interest for the production of fully integrated emission sources and drive electronics for local area telecommunications, along with optical communication within and between chips. Rare-earth doped glasses are predominantly used to produce fiber- or waveguide-based gain elements for longer-haul communications, or perhaps for laser sources. Rare-earth doped wide-bandgap semiconductors are principally, though not wholly, of interest for visible emission. In all cases, the rare-earth ion can serve as a sensitive probe of the electronic and structural properties of the host material.

REEs, also known as active ions, which are a group of 15 transition metals from the periodic table of the elements with atomic numbers 57 (lanthanum) through 71 (lutetium) known as lanthanides or lanthanoids. They can emit light with either very narrow or wide bandwidth in the visible and infrared spectrum when active ions are embedded/doped in a proper host material [24]. Moreover, this emission can be controlled by the host material in which rare-earth ions are doped [25].

The proper functioning of an optical waveguide amplifier is a crucial issue that depends on the guiding material and doped REE that is used. While designing an optical amplifier, it is obligatory to have learned on the accompanying parameters of the gain medium at any rate [19]:

- Energy levels of the gain material
- Lifetimes of the energy levels
- Optical cross-sections between each pair of levels
- Spectral responses of the allowed transitions
- Thermal stability of the gain material
- Suitable host material

In this thesis, a waveguide amplifier device that operates at 1.55 μm which is frequently alluded to as the third telecommunication window was studied. Therefore, it is very important to choose an REE to incorporate into a host material that must have gain characteristics to this band. Erbium is a good candidate, which has an emission band that coincides with the third telecommunication window [22, 26]. The key difference between

Er-doped fiber amplifiers and Er-doped waveguide amplifiers is that much higher concentrations are required to achieve the same gain due to the much shorter lengths. This has led to the investigation of many different materials which have high Er solubilities.

1.4.1. Energy Transition in Erbium

The 4f electron shell is shield by the greater 5s and 5p orbitals, and hence the ion's atomic-like energy structure remains unchanged that the shelf potentially experiences different internal energy transitions. Russell-Saunders notation $^{2S+1}L_J$ is used to represent the levels, where 2S+1 represents the spin angular momentum, L the orbital angular momentum, and J the total angular momentum [27]. For a few earth ions a linear combination of $^{2S+1}L_J$ states is typically considered as the eigenstates of the electronic system. Nevertheless, for simplification purpose each level is differently defined using the leading term of the Russell-Saunders coupled states. Figure 1.5 displays only the related levels to Er-doped amplifier operation for a signal around 1.55 μm, and however extra higher energy levels exist for the 4f shell. That also includes the approximate lifetime (for Er ions in oxide glasses), the wavelength versus the ground-state transition, and the approximate energy in cm-1 relative to the ground state for each level [28]. The Erbium ion has absorption lines including those centered at 530 nm, 650 nm, 800 nm, 980 nm, and 1480 nm as well as ground-state emission lines [29, 30]. Furthermore, potential emission transitions into excited state of the erbium ion are at 850 nm, 1200 nm and 2800 nm [31] using 980nm and 1480 nm pump wavelengths [29, 32].

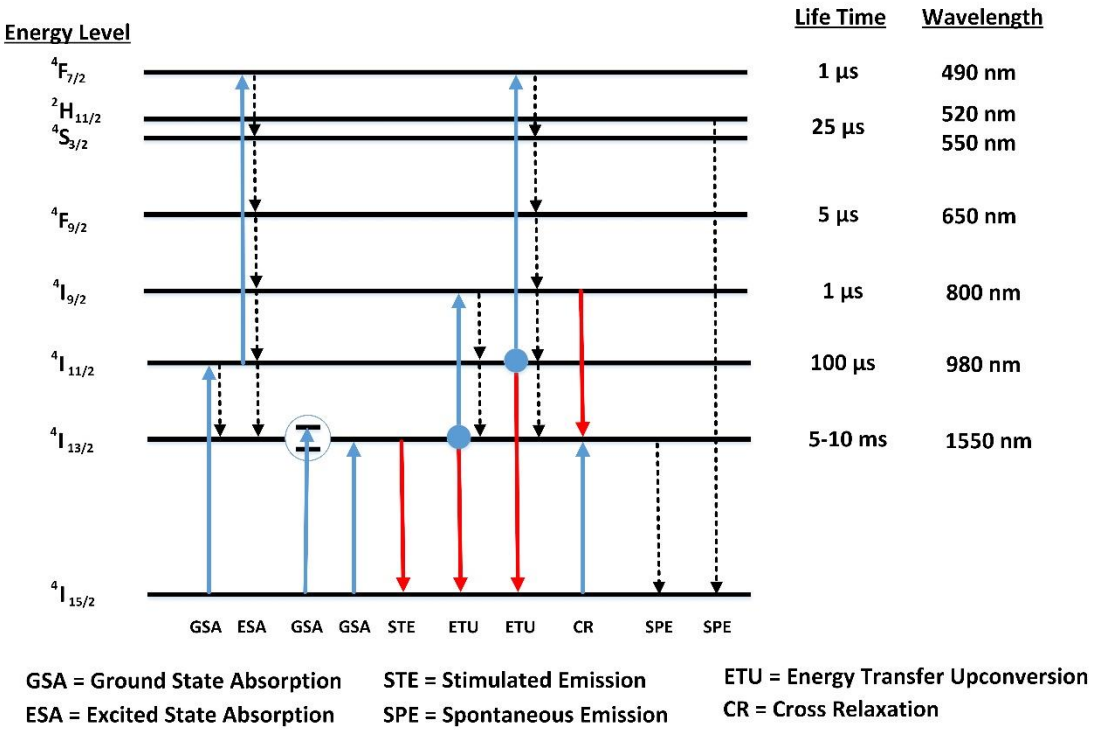

Figure 1.5. *Schematic of energy levels, selected transitions, and lifetimes relevant for Er^{3+} amplifier operation (adapted from [28]).*

In Figure 1.5, you can see the transition of ground-state absorption (GSA) pump light on the $^4I_{15/2} \rightarrow {}^4I_{11/2}$ transition at the first inset, of excited-state absorption (ESA) of 980 nm pump light from the $^4I_{11/2}$ level to the $^4F_{7/2}$ level at the second, of GSA of 1480 pump light directly into the broadened $^4I_{13/2}$ level at the third and of GSA and stimulated emission of ~1530 nm signal light on the $^4I_{15/2} \leftrightarrow {}^4I_{13/2}$ transition at the fourth and the fifth. The sixth and seventh transitions have two energy transfer upconversion (ETU) processes significantly influencing amplifier performance. Then a cross-relaxation (CR) process comes in which an ion in the $^4I_{9/2}$ excited state interacts with another ion in the ground state resulting in both ions running out in the $^4I_{13/2}$ state. Nevertheless, there exists very low population density or a very rare CR process since oxide glasses have extremely short $^4I_{9/2}$ lifetime.

1.5. Deposition Techniques of Optical Waveguide Amplifiers

Determination of the growth method which according to the used area of the device and the material is critical to the success of the application. Different techniques have been employed for waveguide amplifier devices as plasma-enhanced chemical vapor deposition (PECVD) [33-38], high vacuum chemical vapor deposition (HV-CVD) [39],

vapor phase deposition [40, 41], the sol-gel process [42-51], RF-sputtering [52-58], flame hydrolysis [59, 60], dip coating [61], pulsed laser deposition [62-65], reactive co-sputtering [66-72], and atomic layer deposition [73, 74]. Among these techniques, CVD is commonly used to grow high quality crystalline thin films with large uniformity and composition stoichiometry. However, the high substrate temperature for deposition is undesirable in many cases [75].

A comparison of growth methods is given in Table 1.1. All growth techniques have their own superior properties. The choice of the growth method depends on the final device. In active photonic devices such as host doping, uniformity and surface roughness are quite important.

Table 1.1. *Comparison of growth methods [76].*

Method/Property	***ALD***	***CVD***	***Sputter***	***MBE***
Surface Roughness	good	varies	good	fair
Film Density	good	good	good	good
Step Coverage	good	varies	poor	varies
Interface Quality	good	varies	poor	good
Low Temp. Dep.	good	varies	good	good
Deposition Rate	fair	good	good	fair
Doping Capability	good	poor	good	good
Safety	good	poor	good	good
Cost	varies	good	good	fair

For amplifier device applications, with an aim of obtaining high quality erbium-doped waveguiding thin films. Surface roughness contributes to optical losses, because of that CVD and MBE techniques are less desired. MBE is also very expensive tool and requires ultra-high vacuum. Sputtering does not give sufficient interface quality, particularly for multilayer structures it can have negative effects [33]. Sputtering also has not very good uniformity. As for CVD, doping capability is poor. Particularly, doping of active is very important for active device applications. ALD stands out for its features except low growth rate. It can be tolerated by using a large chamber that contains many substrates [34]. ALD will be further discussed in the following sections.

1.6. Al_2O_3 as an Optical Waveguide Amplifier Material

Aluminum oxide (Al_2O_3) thin films have been used as dielectric materials, protective coatings and corrosion-resistance barriers [75]. Recently, Al_2O_3 materials have been extensively used as optical lenses and windows, refractory coatings, anti-reflection coatings, optical waveguides, amplifiers, lasers microelectronic devices, humidity sensors, heat sinks in integrated circuits and for passivation of metal surfaces [77]. In microelectronics, since SiO_2, as the traditional gate dielectric material in field effect transistors (FETs), approaches its ultimate thickness limit, further development of device performance needs new dielectric materials and deposition methods [78]. In this manner, Al_2O_3 has been regarded as a high-k material to replace such SiO2 layers in DRAMs and MOSFETs owing to its excellent dielectric properties, good adhesion to many surfaces and thermal and chemical stability. Additionally, the attention of several researchers has been directed towards using single-mode integrated optical waveguides instead of attenuated total reflection elements due to the requirement of high sensitivity and extremely low limit of detection in biological and chemical sensors. Due to the high refractive index and host material, amorphous Al_2O_3 is suitable for optical waveguide amplifier devices. It is also compatible with Si-based photonics applications.

1.7. Er^{3+}:Al_2O_3 Optical Waveguide Amplifiers

It has been reported that amorphous, crystalline and polymer materials are host for Er doped waveguide amplifiers and lasers, mainly including lithium niobate [79] [51], phosphate glass [52], fluoride glass [80], tellurite glass [81], Y_2O_3 [66], and Al_2O_3 [70, 82-87]. There is a piece of evidence that it is potential to gain up to 2 dB/cm depending on wavelength at the range of 1530 to 1610 nm following optical pumping at 1480 nm with Erbium-doped lithium niobate waveguide lasers [79].

Moreover, the ring lasers in Er^{3+}:$LiNbO_3$ are new instruments that can be utilized as optical gyroscope devices. According to the first experiments, output power up to 150 μW is adequate to produce lasing at 1603 nm, pumping at 1480 nm. Erbium-doped phosphate glass waveguide is fabricated through rf sputtering [52]. The erbium-doped phosphate glass waveguide was pumped at 980 nm with a power of ~21 mW to achieve a net optical gain of 4.1 dB for 10 mm long waveguide at 1.535 μm. As reported, the Er concentration was 5.3×10^{20} cm^{-3}. The erbium-doped fluoride glass waveguides fabricated using spin-coating was introduced [80]. Doping the waveguides of 50 μm in thickness

with up to 3 mol % erbium, it was observed that scattering loss was 0.2 dB/cm at 975 nm and strong green emission was at 520 – 550 nm. Er-doped Tellurite glasses planar waveguide was conventionally formed through melt quenching for power amplifier [81]. In addition, pumping wavelengths at 974 nm gained 0.9 dB/cm at a wavelength of 1535 nm. The signals were enhanced by 10 dB at 1535 nm using a low launched pump power of 1mW at 1480 nm for Y_2O_3: Er^{3+} [66]. Er^{3+}:Al_2O_3 planar waveguide amplifiers have widely been studied and many devices have been reported by several research groups [70, 82-87]. 5.4 dB/cm optical net gain was demonstrated at 1553 nm [70], and lossless power splitters with loss compensation were achieved [88-91]. Pumping at a 977 nm as opposed to 1480 nm total internal net gain of up to 9.3 dB was measured, an internal net gain was obtained over a wavelength range of 80 nm (1500–1580 nm), and a peak gain of 2.0 dB/cm was measured at 1533 nm [85]. An integrated continuous wave laser was demonstrated [92-95]. These results show that Al_2O_3 is well suited as a host material for rare-earth ions.

In this thesis, we report the optimization of ALD growth parameters for the fabrication of amorphous Al_2O_3 host materials to obtain the minimum propagation loss. Then, the growth optimization process of Er_2O_3 was completed. The doping process was precisely controlled using Al_2O_3 and Er_2O_3 recipes, both optimized. Ridge waveguide amplifiers supporting a single-mode were fabricated by lithography from the active planar structures. The optical gain and lifetime measurements of the fabricated devices were characterized by using an optical setup.

2. PASSIVE AL_2O_3 WAVEGUIDE DEVICES: GROWTH AND LOSS MEASUREMENTS

2.1. Al_2O_3 Planar Waveguide Fabrication Using Atomic Layer Deposition

2.1.1. Atomic Layer Deposition

Atomic layer deposition (ALD) is a type of chemical vapor deposition technique where sequential exposures of gas-phase reactants are used to deposit thin films with atomic layer accuracy and appears so far to be the most promising method for the growth of high-k materials with excellent qualities. ALD has several advantages because of its self-controlled growth mode. The thickness of the films may be controlled in a simple way by controlling the number of reaction cycles, therefore enabling the controlled growth of ultra-thin films at a relatively low substrate temperature. This results in a unique self-limiting film growth mechanism with many advantageous features, such as excellent conformity, large area, and accurate film thickness control. The self-limiting growth mechanism also ensures good reproducibility and relatively straightforward scale-up [80, 102]. As a result, ALD is a powerful growth method with a very high potential for waveguide applications and doping. The basic schematic diagram of ALD process is given in Figure 2.1. There are four steps in one ALD cycle can be listed as follows;

1) First precursor vapor pulse
2) Purging the unreacted first precursor's vapors,
3) Second precursor vapor pulse
4) Purging the unreacted second precursor's vapors and by-products

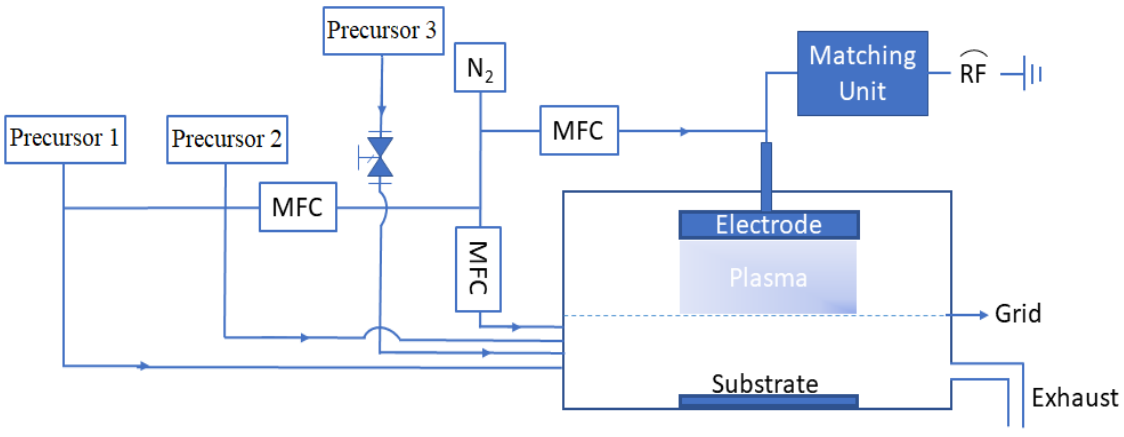

Figure 2.1. *Schematic diagram of used ALD system*

The above steps are repeated until the desired thickness. The accessible thickness of per cycle can be experimentally determined for different temperatures. Cycle duration depends on the used precursors and deposition temperature. An illustration of one ALD cycle is given in Figure 2.2a.

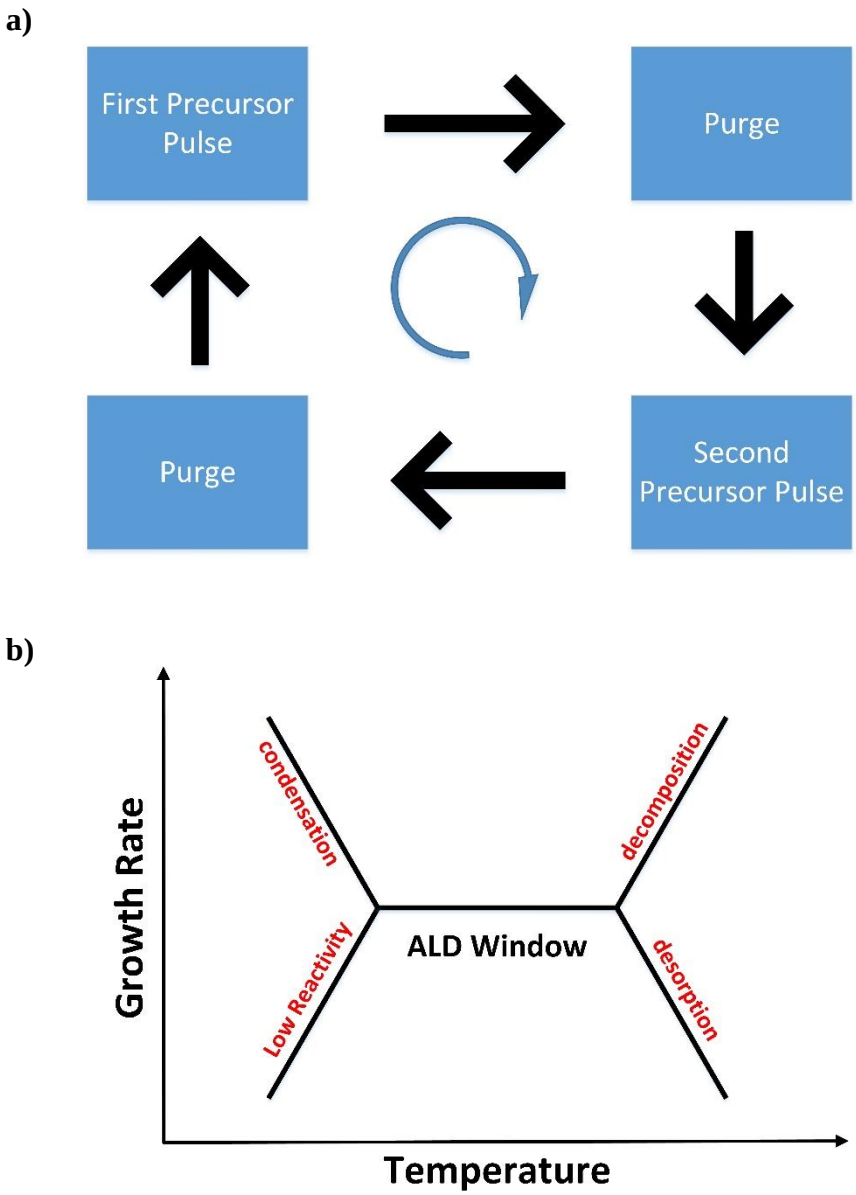

Figure 2.2. *a) Schematic illustration of ALD cycle b) Illustration of ideal ALD deposition window*

The idealized temperature window of the ALD process, indicated by the growth per cycle as a function of temperature in Figure 2.2b. In the case of ALD behavior, self-limiting growth is obtained and ideally, a weak or no dependence on temperature is

observed, while outside the window the ALD behavior is lost due to one of four effects. Condensation: precursors can condense on the surface preventing effective purging; low reactivity: low temperatures can prevent complete reactions from taking place; decomposition: when precursors decompose, a (parasitic) CVD component can be added to the growth; desorption: the film itself or the precursor can desorb, thereby reducing growth. All the below advantages show that ALD is a suitable method for active and passive integrated optical device deposition. The advantages of ALD can be summarized as follows,

- Nanometer level thickness control
- Processes scalable over very large areas
- Potential for rare-earth doping
- Gentle deposition for sensitive substate
- Multilayer growth capability
- Low defect density
- Insitu thickness measurement capability
- Plasma enhanced process capability
- Good thickness uniformity
- Excellent reproducibility
- Good film density
- Low temperature growth
- Good step coverage

2.1.2. Deposition process

The fabricated passive planar waveguide core was 0.5-μm-thick a-Al_2O_3. TMA and di-water were used to fabricate a-Al_2O_3 by using thermal Atomic Layer Deposition (tALD). As a result of the optimization of the Al_2O_3 growth processes by using tALD, the samples that were grown at 300°C were found to be superior to the samples grown at other temperatures [96].

If we list some of these advantages,

1) The ellipsometry measurements had the highest refractive index according to the result.
2) The XRD results showed that it still protected the amorphous structure and thus prevented possible losses that could occur because of birefringence

3) The FTIR results showed that the OH concentration, which is one of the causes of optical losses, was lower.
4) It had the best stoichiometry structure according to the XPS results.

Since these properties are known to tend to reduce optical losses for waveguide applications, the passive planar waveguide growth was performed at growth parameters with a temperature of 300 °C.

2.1.3. Optical loss measurement

The passive planar waveguide growth process was concentrated on three different Al_2O_3 thicknesses which were 0.5, 0.75 and 1 μm. 7-μm SiO_2 on p-type silicon was used as the substrate. The optical modes were excited using a prism coupler. The accuracy of the thickness and refraction index obtained from the prism coupler increased with an increase in the number of excited modes. Passive planar waveguide with a thickness of 0.5 μm Al_2O_3 supported only one optical mode at 633, 829 and 1549 nm. Since 0.75 and 1 μm waveguides had two and three optical modes at 633 nm, respectively, thickness and refractive indices can be measured with a prism coupler with high accuracy. Since the refractive indices of the grown Al_2O_3 layers were not dependent on the thickness, it was observed that the refractive indices measured in the thicker samples were compared to the refractive indices in the thin samples, and the two methods complement each other. The optical path of the laser of the prism coupler is given in Figure 2.3.

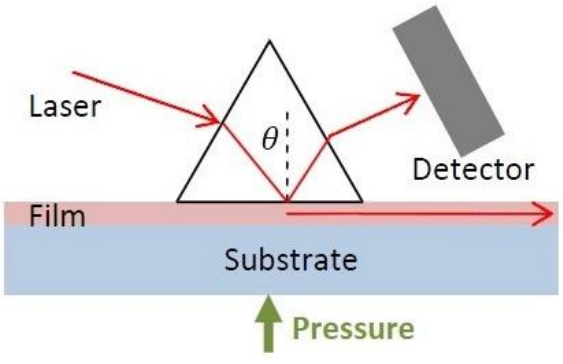

Figure 2.3. *Schematic of mode measurement setup*

The excited optical mode measurements using the 633, 829 and 1549 nm of the $Si/SiO_2/Al_2O_3$ structure with 0.5 μm Al_2O_3 are shown in Figure 2.4. The modes for TE and TM polarization at λ = 633, 829 and 1549 nm are given in Figure 2.4a-b, Figure 2.4c-

d and Figure 2.4e-f, respectively. To briefly explain optical mode excitation, the prism coupler was connected to a motorized system that can rotate. With the help of a pneumatic system, the surface of the planar waveguide and the surface of the prism were fixed to each other. The corresponding laser reaches this prism with the help of mirrors. Fine tuning on the mirrors brings the laser onto the coupling spot for entering the laser to the waveguide. After this, the incident angle of the laser was changed by the motorized system. When the corresponding coupling angle was reached, a photodetector which was at the end of the laser optical path does not detect the laser. At this time, a local dip is observed at the photodetector. This dip means the optical mode is supported, that is, the prism coupler position was where the light travels through the waveguide. In Figure 2.4, TE_0 is the fundamental mode for TE polarization, and TM_0 is the fundamental mode for TM polarization.

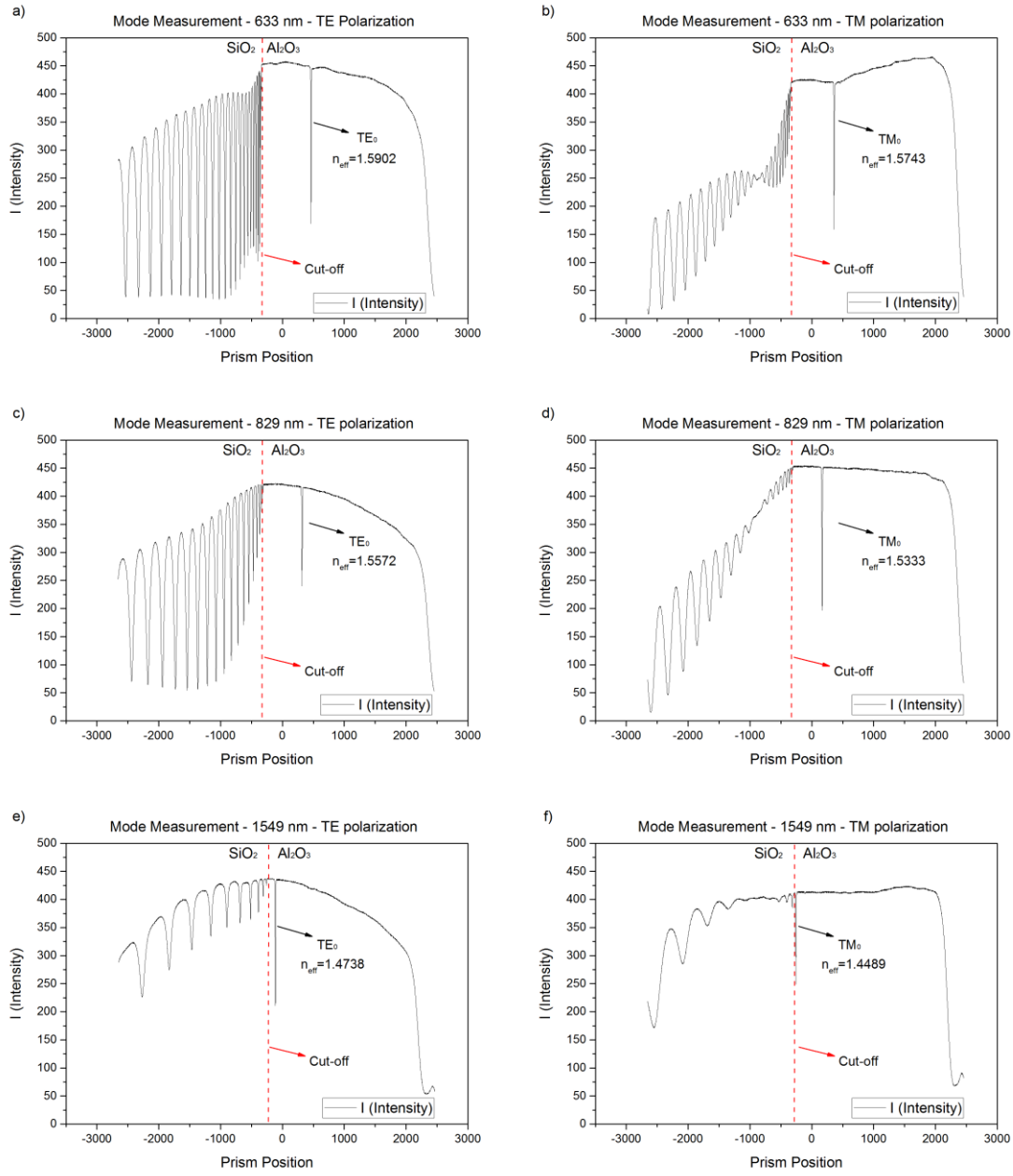

Figure 2.4. *Excited optical modes at different wavelengths of Si/SiO_2/Al_2O_3 planar waveguides with 0.5 μm guiding layer a) TE polarization at λ=633 nm b) TM polarization at λ=633 nm c) TE polarization at λ=829 nm d) TM polarization at λ=829 nm e)TE polarization at λ=1549 nm f) TM polarization at λ=1549 nm*

The effective index that measures the mode is written under the relevant modes. The red line indicates the mode cut-off. The right side of the cut-off shows the modes supported in the Al_2O_3 layer and the left side shows the modes supported in the SiO_2 layer. The modes supported in the SiO_2 layer were leakage modes. These modes are not important in terms of light guidance, but it is important to measure the SiO_2 substrate thickness and index of refraction and make the overall measurement highly sensitive. The

fact that the mode supported in the Al_2O_3 layer was close to the cut-off leads to the mode to be distinguished as well as to mixing of the mode profile with the SiO_2 layer. This causes additional optical loss. For this reason, it was important that the mode supported was away from the cutting point. The supported mode effective indices were measured respectively as 1.5902 and 1.5743 for TE and TM polarization at 633 nm laser, 1.5572 and 1.5333 for TE and TM polarization at 829 nm laser, 1.4738 and 1.4489 for TE and TM polarization at 1549 nm laser. As the wavelength increased, the supported mode approaches the cut-off. It means the effective index of the supported mode decreased. The TE and TM modes supported at 1549 nm wavelength were very close to the cut-off. In particular, optical loss measurements in the TM mode does not provide the actual value of loss. Therefore, this measurement was not taken into account in the optical loss measurements.

Table 2.1. *The measured and calculated effective index values for waveguides with 0.5, 0.75 and 1 μm Al_2O_3 film thicknesses. The observed number of modes are given in the last column of the table*

Thick. (μm)	**λ (nm)**	**Polarization**				**Number of Mode**	
		TE_0		**TM_0**		**TE**	**TM**
		Meas.	**Theo.**	**Meas.**	**Theo.**	**Meas.**	**Meas.**
0.5	**633**	1.5902	1.5898	1.5743	1.5758	1	1
	829	1.5572	1.5546	1.5333	1.5325	1	1
	1549	1.4738	1.4747	1.4489	1.4491	1	1
0.75	**633**	1.6188	1.6169	1.6114	1.6111	2	2
	829	1.5951	1.5903	1.5826	1.5796	2	1
	1549	1.5223	1.5311	1.4930	1.4931	1	1
1	**633**	1.6314	1.6291	1.6271	1.6262	3	3
	829	1.6130	1.6077	1.6056	1.6021	2	2
	1549	1.5533	1.5518	1.5318	1.5321	1	1

The theoretical values were calculated by using the MATLAB-based 1-D wave equation solver. It was important that the effective indices were close to each other in order to support the accuracy of the measurement. The comparison of the theoretical calculations and measurements are given in Table 2.1. In the theoretical calculations, the refractive indices of Al_2O_3 and SiO_2 were respectively 1.65 and 1.458 for the 633 nm wavelength, 1.64 and 1.45 for the 829 nm wavelength, 1.63 and 1.444 for the 1549 nm

wavelength. The refractive index values of Al_2O_3 were taken as the result of the measurement of the prism coupler. As shown in Table 2.1, the measured and calculated effective index values of the supported optical modes were very close to each other. From these results, the supported mode was exactly where we expected it to be, and our measurements were correct. Optical loss measurements were performed after the accuracy of the measurements was supported. The prism coupler's position for optical loss measurements was set to support the fundamental mode (TE_0 or TM_0). The photodetector was disassembled and replaced with a fiber detector. This fiber detector acts as a single axis, measuring the amount of light emitted from the Al_2O_3-air interface as it passes through the waveguide. Thus, it was possible to measure light intensity according to the position while the light travels in the waveguide. The schematic representation of the optical loss measurement is shown in Figure 2.5.

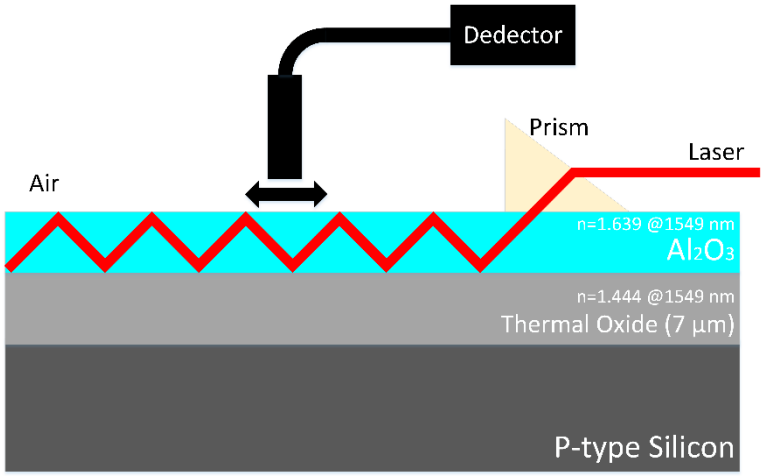

Figure 2.5. *Schematic of optical loss measurement setup (adapted from [97])*

After collecting propagation data, the optical loss was calculated in dB/cm by using the following Equation 2.1. In the given equation, I_0 is the measured laser power at d_1, I is the measured power at d_2, α is the propagation loss, and $d_1 - d_2$ is the loss measurement length.

$$I = I_0 e^{-\alpha(d_1 - d_2)} \tag{2.1}$$

The optical loss measurements were performed for the 0.5-μm-thick Al_2O_3 passive planar waveguide with a total of 5 different combinations. These were the TE polarization of 633,829 and the 1549 nm wavelength and the TM polarization of 633 and the 829 nm wavelength. The TM polarization of the 1549 nm wavelength was not measured because its supported mode was very close the cut-off. This causes the optical loss to be much higher than the actual value due to its influence on the mode profile. The measurement of each combination was repeated at different points. The optical loss measurement for TE_0 at the 1549 nm wavelength is given in Figure 2.6. The results obtained from all measurements are given in Table 2.2.

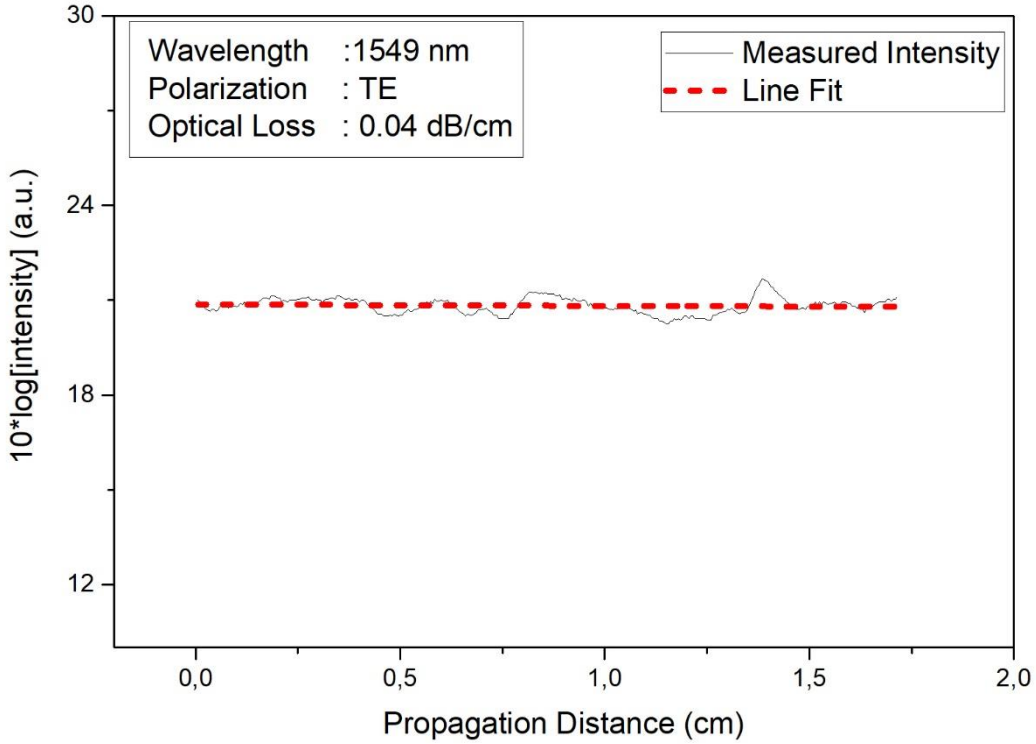

Figure 2.6. *Optical loss measurement of TE_0 at λ=1549 nm wavelength*

The TE and TM polarizations of the 633 nm wavelength were measured as 0.10 ± 0.01 and 0.21 ± 0.04 dB/cm, respectively. The TE and TM polarizations of the 829 nm wavelength were measured as 0.07 ± 0.01 and 0.16 ± 0.03 dB/cm, respectively. The TE polarization of the 1549 nm wavelength was measured as 0.04 ± 0.02 dB/cm. When the optical loss in the TE and TM polarization was examined, it was seen that the optical loss decreased as the wavelength increased. When the optical losses in different polarizations of the same wavelength were examined, it was observed that the losses in the wavelengths

with the TE polarization were lower. The lowest optical loss value was 0.04 ± 0.02 dB/cm obtained with the TE polarization of the 1549 nm wavelength. The Al_2O_3 passive planar waveguide with the lowest loss in the literature was fabricated [98].

Table 2.2. *All optical loss measurements*

Wavelength (nm)	Polarization	Measurement Length (cm)	Calculated Optical Loss (dB/cm)	Measured Optical Loss (dB/cm)
633	TE	2.33	0.12	0.10 ± 0.01
		2.22	0.09	
		2.92	0.09	
		1.36	0.11	
		2.31	0.09	
		2.42	0.1	
	TM	2,73	0,19	0.21 ± 0.04
		1,65	0,17	
		1,34	0,23	
		2,74	0,26	
		2,2	0,21	
		2,94	0,17	
829	TE	2,57	0,07	0.07 ± 0.01
		2,1	0,05	
		1,71	0,05	
		0,89	0,07	
		0,37	0,08	
		1,75	0,07	
	TM	2,16	0,11	0.16 ± 0.03
		2,23	0,15	
		2,33	0,17	
		2,3	0,19	
		2,72	0,16	
		1,44	0,19	
		1,08	0,18	
1549	TE	1,95	0,02	0.04 ± 0.02
		1,91	0,05	
		1,22	0,02	
		1,47	0,03	
		1,49	0,06	
		1,92	0,02	
		1,64	0,05	
		1,61	0,03	

2.2. Al_2O_3 Ridge Waveguide Fabrication

2.2.1. Waveguide Design

The ridge waveguide mode analysis was performed for $\lambda = 1.55$ μm to identify the region where with single-mode propagation only. Depending on the geometry of the waveguide n_{eff} changes where n_{eff} values smaller than substrate refractive index result no light propagation. BPM is a valid technique to investigate effect of the ridge height, ridge width, wavelength and polarization to the mode number and mode size [99]. Design parameters for targeted properties are computed for the ridge width ranging from 0 to 8 μm, and for etch depth ranging from 0 to 0.45 μm. It is apparent from Table 2.3 that there exists a range of etch depth values for the fixed-width where the waveguide has a single-mode character.

Table 2.3. *Optical mode mapping of ridge waveguides at 1.55 μm*

<table>
<tr><td></td><td colspan="6">Etch Depth (μm)</td></tr>
<tr><td>Width (μm)</td><td>0.2</td><td>0.25</td><td>0.30</td><td>0.35</td><td>0.40</td><td>0.45</td></tr>
<tr><td><1</td><td colspan="6">No Propagation</td></tr>
<tr><td>1</td><td>TE-SM</td><td colspan="5">No Propagation</td></tr>
<tr><td>1.5</td><td colspan="6" rowspan="3">TE- Single Mode Propagation
TM- No Propagation</td></tr>
<tr><td>2</td></tr>
<tr><td>2.5</td></tr>
<tr><td>3</td><td colspan="6">TE- Single Mode Propagation
TM- Single Mode Propagation</td></tr>
<tr><td>3.5</td><td>TE-MM
TM-SM</td><td colspan="5">TE- Single Mode Propagation
TM- Single Mode Propagation</td></tr>
<tr><td>4</td><td colspan="3">TE-Multi Mode Propagation
TM-Single Mode Propagation</td><td colspan="3">TE- Single Mode Propagation
TM- Single Mode Propagation</td></tr>
<tr><td>4.5-8</td><td colspan="6">TE-Multi Mode Propagation
TM-Single Mode Propagation</td></tr>
<tr><td>>8</td><td colspan="6">TE-Multi Mode Propagation
TM-Multi Mode Propagation</td></tr>
</table>

As an example, W=1.5-2.5 μm and D=0.2-0.45 μm is one of these geometries that supports only TE single-mode and does not support TM mode. If we change the width of the ridge waveguide to 3 μm for same range of the etch depth, we end up with a waveguide

that has single mode for both TE and TM. Width values below 1 μm have no optical mode propagation for both polarization. Width values above 8 μm have multi-mode propagation for both polarizations.

2.2.2. Mask design

The design of the mask to be used for the passive ridge waveguide was completed. Our previous results [100, 101] were used as a road map. The calculated ridge widths to fabricate wavelength- and polarization-insensitive waveguides that support the fundamental mode for 3 different thicknesses will be obtained by lithography using this mask. It was aimed to cover all ridge widths on the safe fabrication line calculated for 3 different wavelengths with a single mask. Thus, the desired passive ridge waveguide can be produced with a single mask and the cost will be reduced. The mask that was designed and manufactured as shown in Figure 2.7.

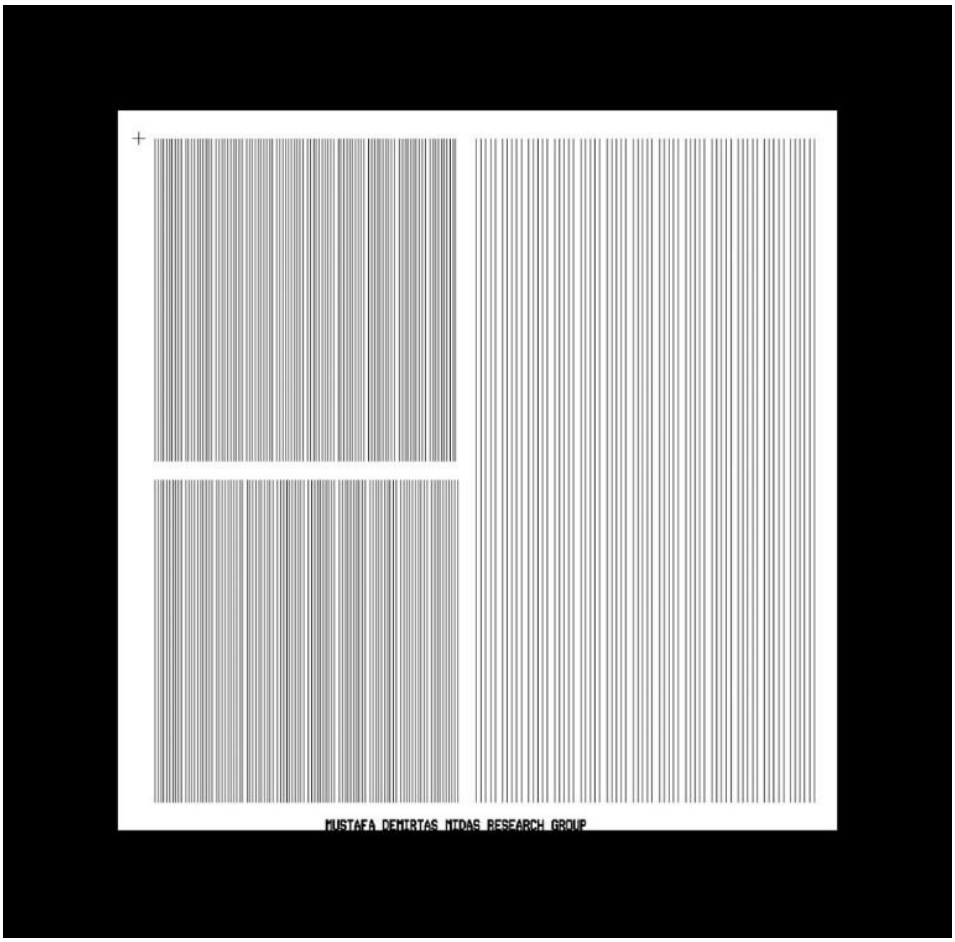

Figure 2.7. *Mask designed to fabricate passive ridge waveguide*

The designed mask consisted of two parts. These were for the fabrication of a passive ridge waveguide with a length of 3.4 cm (short) and a passive ridge waveguide with a length of 7 cm (long). The main reason for choosing a passive ridge waveguide with a length of 3.4 cm was to fit all the needed ridge widths into a single mask. The passive ridge waveguide with a length of 3.4 cm was drawn 10 times for each designed ridge width. There was a gap of 300 μm between each passive ridge waveguide. Thus, when at least 2 and up to 10 waveguides are fabricated on a single chip, optical mode interference would be avoided between passive ridge waveguides. For better visualization under the microscope, a marker of 500 μm spacing, a marker at each half cm, reminders for the amount of the current peak width, markers indicating the quality of the lithography process were placed between each pair of the 10-piece set. Short passive ridge waveguides were drawn with a total of 20 different ridge widths between 1.2 and 5 μm and an increasing step of 0.2 μm. There is a 500 μm gap between the long passive ridge waveguides and 5 pieces for each ridge width. The gap between each set was 750 μm. Long passive ridge waveguides were drawn between 1.2 and 4 μm ridge width and an increasing step of 0.2 μm. Like the short passive ridge waveguides, markers are added between the sets, length indicators, and reminders that showed the current ridge width.

2.2.3. Device fabrication using photolithography

Prior to the lithography experiments with the doped structure, the initial experiments were carried out with a passive structure with 1 μm of thickness. Lithography experiments were performed with an AZ5214E photoresist and an AZ351B developer. Optical printing was performed using the "Image reversal" technique.

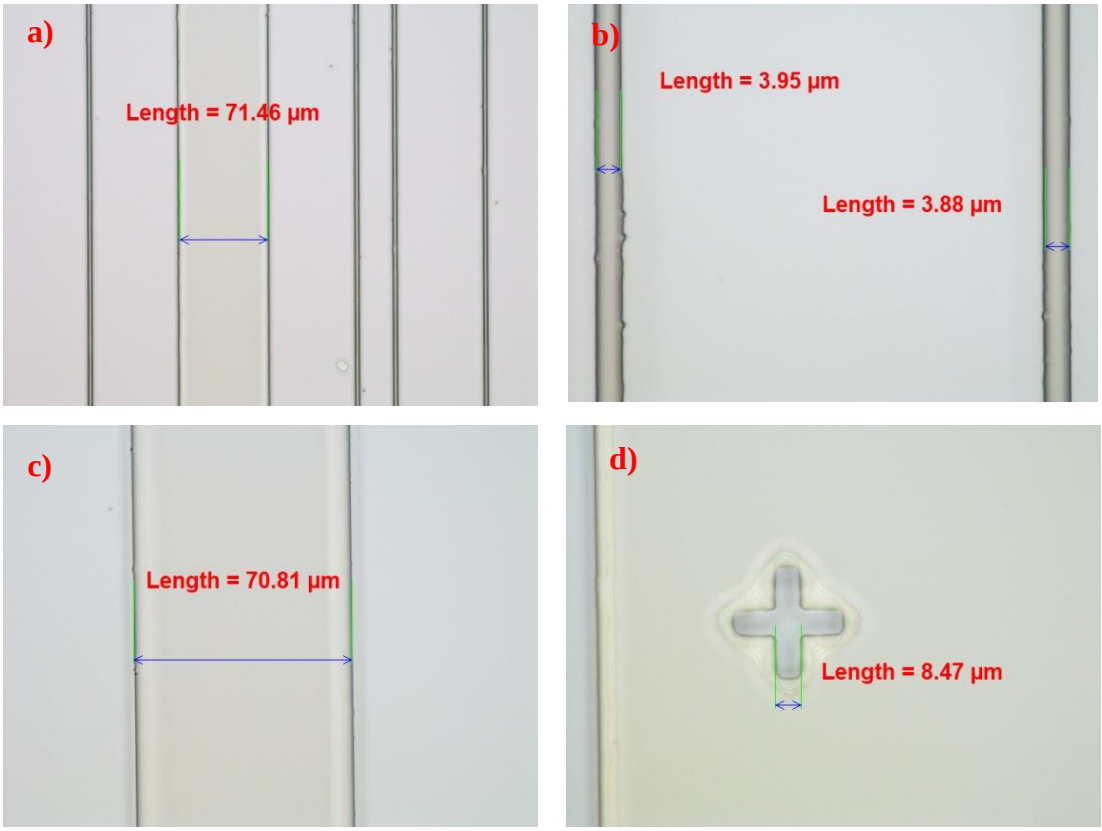

Figure 2.8. *Images from the top of the photoresist layer printed by the mask with lithography operations a) Photoresist image at different widths from the top b) Photoresist image printed with 4 µm width c) Photoresist image printed with 70 µm width d) Marker image printed with 8.5 µm width*

The photoresist was coated at 4000 rpm for 60 seconds. The coated sample was baked at 110 ° C for 50 seconds. The mask aligner was UV-cured for 50 seconds with the part of the mask that we want. The photoresist was inverted by baking again at 120 °C for 2 minutes. Again, the mask aligner was UV-cured for 50 seconds without masking. The sample was dipped into the solvent mixture with a 1:4 ratio for 50 seconds, which is awaited 5 minutes. After the developer process, the sample was baked at 140 °C for 75 minutes.

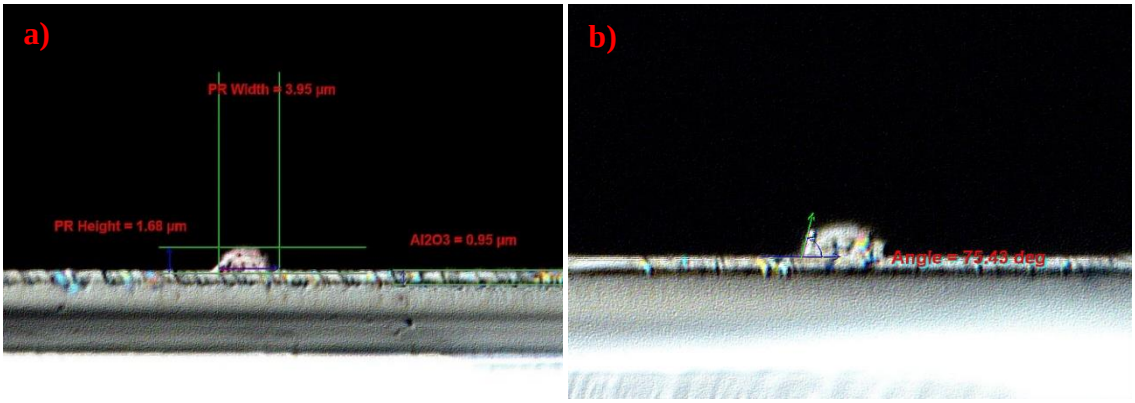

Figure 2.9. *Cross-sectional views of photoresist layer printed by mask a) Photoresist width, height and thickness of Al_2O_3 layer b) Photoresist rib angle*

The printed sample was viewed for the width and height measurements from the top and the cross section using an optical microscope. Figure 2.8 shows the optical images of the printed photoresist with width measurements. Figure 2.8a shows the photoresist ribs printed at different widths taken with the x50 objective lens. The images in Figure 2.8b, c and d were taken with the x100 objective lens. Figures2.8b and c show photoresist ribs printed with widths of 4 and 70 µm, respectively. Figure 2.8d shows a marker image printed at a 8.5 µm width. The results show that images printed with image reversal were usable for fabrication. The images taken from the cross-section of the samples are given in Figure 2.9. The photoresist height and width were measured as 1.68 and 3.95 µm, respectively. The angle of the photoresist rib was measured as 75°. The photoresist width, height, and thickness of the underlying Al_2O_3 layer are shown in Figure 2.9a, and the photoresist rib angle is shown in Figure 2.9b. The similarity of the colors was due to the similarity of the refractive indices of the photoresist and Al_2O_3.

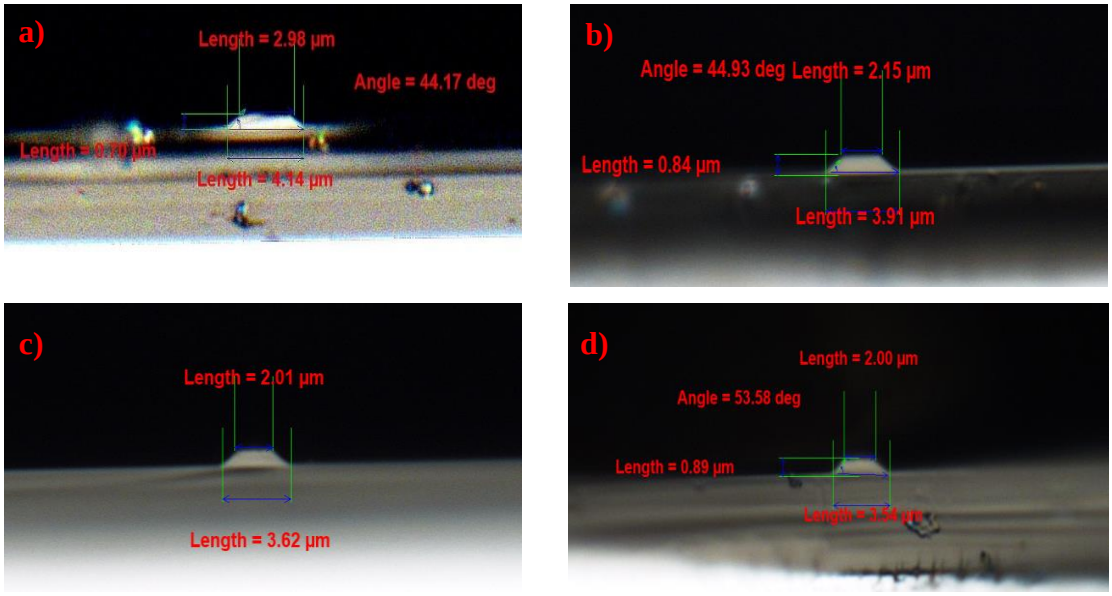

Figure 2.10. *Cross-sectional views of the samples resulting from the chemical etching a) 15 min etch b) 20 min etch image 1 c) 20 min etch image 2 d) 20 min etch image 3*

The sample was immersed in 85% H_3PO_4 that was kept on a 75 °C hot plate for 30 minutes. The etching experiments were carried out for 15 and 20 minutes. After wet etching, the photoresist was removed and the cross-section image was taken with an optical microscope. Figure 2.10 shows a cross-sectional view of the fabricated passive device. Since chemical etching was isotropic, the top and bottom widths of the top were different. The device geometry obtained for the 15 minutes result is given in Figure 2.10a. The passive device had a rib top width of 2.98 µm and a rib bottom width of 4.14 µm. The rib height was 0.70 µm and the rib angle was measured as 44°. The etch rate was calculated to be 46 nm. The device geometries obtained for 20 minutes are given in Figures 2.10b, c, and d. The rib top width was measured between 2.00 and 2.15 µm and the rib bottom width was measured between 3.54 and 3.91 µm. The rib height was measured between 0.84 and 0.89 µm and the rib angle was between 44 and 53°. The etch rate was calculated as 43 nm. As the etch time increased, the width of the top and bottom of the rib decreased. This is an indication that the result was an isotropic etching.

2.2.4. Numerical Modeling of Fabricated Waveguides

Simulation of the fabricated passive waveguides was carried out for the TE and TM polarizations at λ=1550, 1480 and 980 nm. The confinement factor was calculated for the fundamental mode. The results are given in Table 2.4 for single-mode operation at λ=1480 and 1550 nm and multiple mode operation at λ= 980 nm for both the TE and TM

polarizations. As expected, the confinement factor value decreased as the operation wavelength increased. TE confinement starts from 65.17% for smallest single-mode dimension and increases up to 82.77% as wavelength decreases. TM confinement starts from 56.08% for smallest single-mode dimension and increases up to 79.95% as wavelength decreases.

Table 2.4. *Confinement factor and mode number results for different wavelengths and polarizations*

Wavelength (nm)	**Supported optical mode**		**Confinement Factor**	
	TE	**TM**	**TE**	**TM**
980	2	3	%82.77	%79.95
1480	1	1	%67.45	%59.23
1550	1	1	%65.17	%56.08

Mode profiles were given in Figure 2.11a and 2.11b depicts electric field profiles for TE and TM polarizations at λ=1550 nm. In the BPM method that we use, we always monitor the electric field profile. The electric field is along X direction (vertical direction) for TE polarization. In this direction, maximum boundary dimension that field encounters is the total waveguide height which is 0.5 μm thick. In the case of TM polarization, electric field is along Y direction (lateral direction). Lateral direction includes width, which is 5 to 6 times larger than total height. Therefore, the electric field of TM polarization is much larger than TE and to fulfill boundary conditions mode size has to be larger than TE polarization. The effective index method was also used to reach the same conclusion.

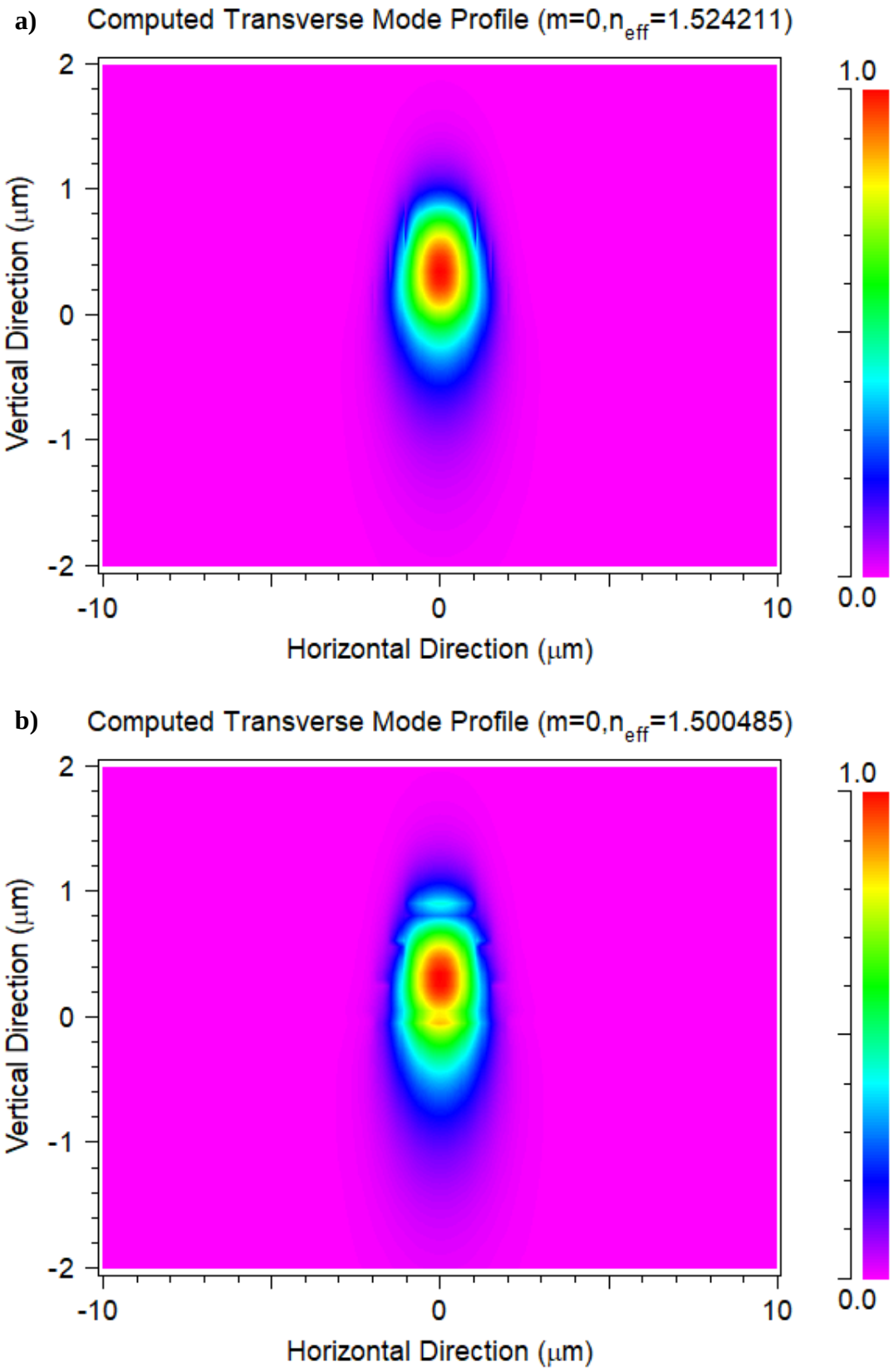

Figure 2.11. *Mode field profiles for λ=1.55 μm a) TE b) TM*

2.2.5. Measurement setup and mode excitation

The fabricated passive device was excited using the $\lambda = 632$ nm laser with the setup installed on the optical table. The single-mode laser was used. The images of the guided light are given in Figure 2.12 that shows the multi-mode propagation process. Work on the development of measures of the active structure was ongoing. To focus the laser beam, an x20 objective lens was used. Mode output clearly observable in Figure 2.12b. This measurement setup is revised for lifetime and gain measurements.

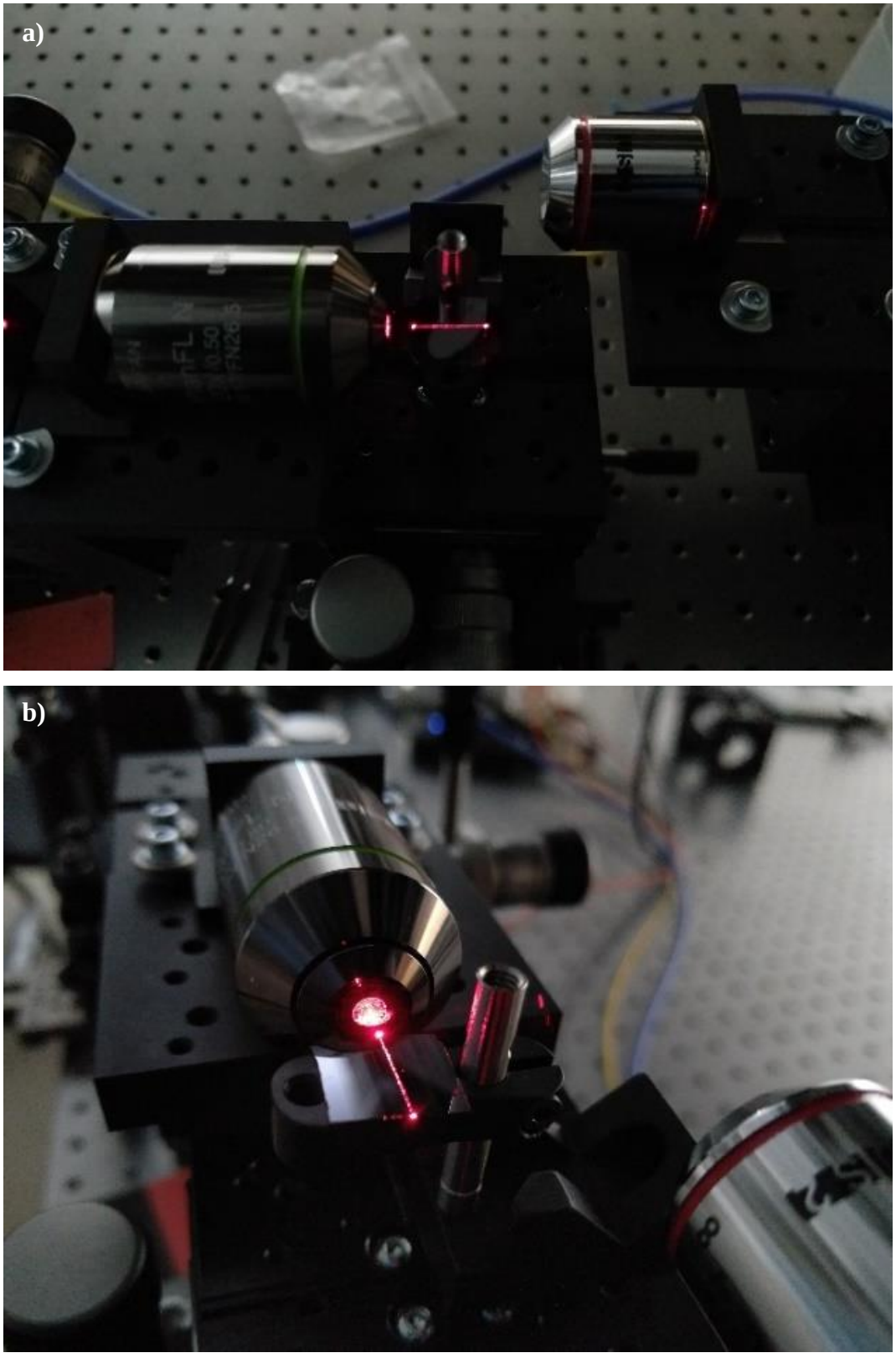

Figure 2.12. *Guided light on passive waveguide at λ=632 nm* a) side view b) front view

3. ERBIUM DOPED AL_2O_3 WAVEGUIDE AMPLIFIER: FABRICATION AND OPTICAL CHARACTERIZATION

3.1. Growth Optimization of Al_2O_3 using Plasma Enhanced ALD

Thermal and plasma growth operations could not be performed within the same growth process because the Beneq TFS200 ALD system, which is installed in our research laboratory, has separate physical apparatus removal/attachment operations for thermal and plasma processing. Due to this physical constraint, the Al_2O_3 layers grown by the thermal process described in the previous report could not be doped with the Er_2O_3 layers, which were grown with the $Er(thd)_3$ precursor using thermal ALD. Due to these scientific and physical constraints mentioned above, the thermal optimization of the Al_2O_3 growth process was achieved using Plasma Enhanced ALD (PEALD). The growth temperature was planned to be 300 °C again. Similarly, the positive effect of incensement of the growth temperature was supported by measuring the refraction index and growth rate.

In PEALD Al_2O_3 layer optimization, triaxial figures were used to see the effects of the experimentally changed parameters on the refractive index and the growth rate, as in the case of Er_2O_3 optimization. Each growth experiment had 500 ALD cycles. P-type <100> orientation silicon was used as the substrate. The measurements were made at 4 different points in each sample, 16 measurements were taken for each experiment in total, the accuracy and precision deviations of the Al_2O_3 layers were aimed to be minimized, and standard deviation values were determined. In the figures, the line indicated by blue shows the refractive index and the line indicated by black shows the growth rate. 500 ALD cycles were used for every optimization process.

3.1.1. Temperature optimization

Measurements of the thickness and the refractive index were made by growth samples at different temperatures. The experimental temperatures were 50, 75, 100, 150, 200, 250 and 300 °C. Other parameters and values that were held constant while the growth temperature was changed were the Plasma RF Power of 100 W, TMA pulse time of 180 ms and O_2 pulse time of 3 s. The thickness and the refractive index measurements of each growth sample were made. Since the measured refractive index values were independent of thickness, they were used directly. In order to calculate the growth rate, the measured thicknesses were divided by ALD cycles of 500, and the growth rate of each

sample was calculated. The measured refractive index and the calculated growth rates are given in Table 3.1.

Table 3.1. *Measured refractive index and growth rate in temperature optimization*

Growth Temp. (ºC)	Growth Rate (nm/cycle)	Standard Deviation	Refractive Index	Standard Deviation
50	0.1764	0.0007	1.587	-
75	0.1532	0.0006	1.594	0.001
100	0.1438	0.0003	1.608	0.002
150	0.1279	0.0006	1.619	0.001
200	0.1010	0.0007	1.635	-
250	0.0950	0.0004	1.635	0.001
300	0.0939	0.0008	1.636	0.001

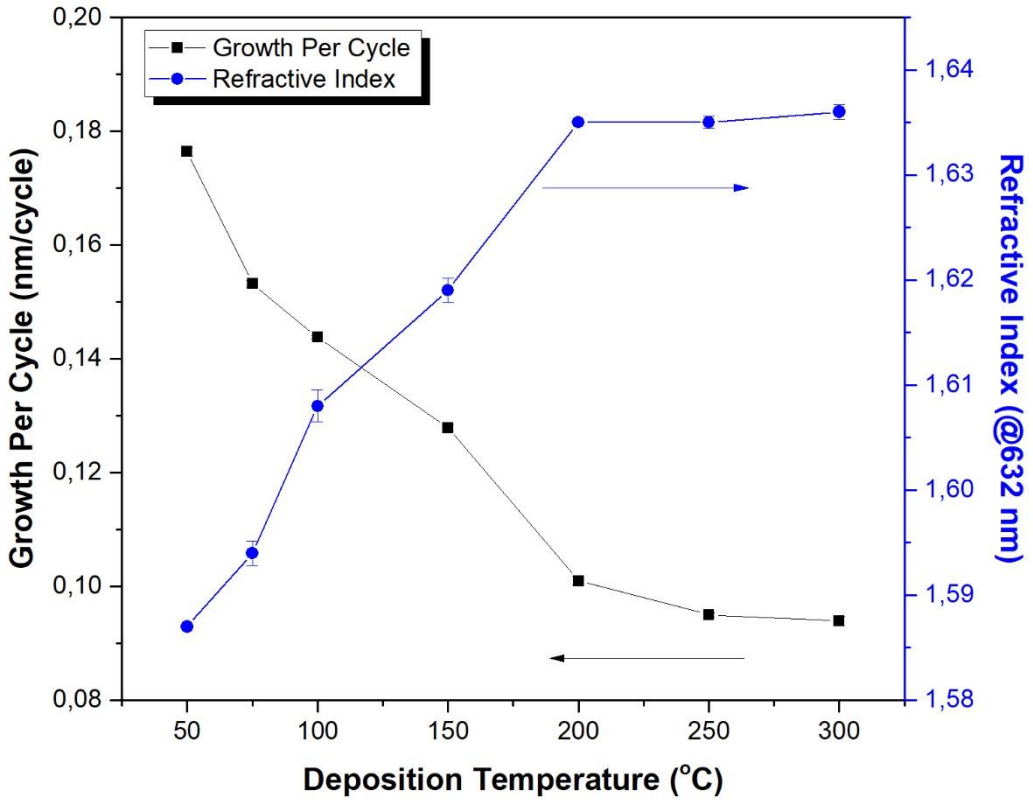

Figure 3.1. *Temperature optimization between 50 and 300 °C*

The growth rates were calculated as 0.1764 ± 0.0007, 0.1532 ± 0.0006, 0.1438 ± 0.0003, 0.1279 ± 0.0006, 0.1010 ± 0.0007, 0.0950 ± 0.0004 and 0.0939 ± 0.0008 nm/cycle for 50, 75, 100, 150, 200, 250 and 300°C, respectively. The refractive indices

were measured as 1.587, 1.594 ± 0.001, 1.608 ± 0.002, 1.619 ± 0.001, 1.635, 1.635 ± 0.001 and 1.636 ± 0.001 for 50, 75, 100, 150, 200, 250 and 300 °C, respectively.

Figure 3.1 shows the values given in Table 3.1. It may be observed in Figure 3.1 that, as the temperature increased, the growth rate decreased and the refractive index increased. Although the refractive index seemed to reach saturation after 200 °C, the continuing decrease in the growth rate may be an indicator of a more intense film. In the previous reporting period, the growth temperature was similarly selected as 300 °C. This is why, in other optimization processes, it is better to show the selected values and understand the change better.

3.1.2. Plasma RF power optimization

The effect of plasma RF power was investigated after the growth temperature was determined. RF power was selected as 50, 100 and 150 W. In the previous experiment, since the RF power was already 100 W for growth, it was aimed to analyze the effect by testing higher and lower RF powers. The parameters of the experiment were fixed at a temperature of 300 °C, TMA pulse time of 180 ms and O_2 pulse time of 3 s. The refractive index and the calculated growth rate obtained by changing the plasma power are given in Table 3.2. The growth rates were calculated as 0.0984 ± 0.0005, 0.0939 ± 0.0008, 0.0925 ± 0.0002 nm/cycle for the plasma RF powers of 50, 100 and 150 W, respectively. The refractive indices were measured as 1.638 ± 0.001, 1.636 ± 0.001, 1.636 ± 0.001 for the plasma powers of 50, 100 and 150 W, respectively. These values are shown in Figure 3.2.

Table 3.2. *Measured refractive index and calculated growth rate in plasma RF power optimization*

Plasma RF Power (W)	Growth Rate (nm/cycle)	Standard Deviation	Refractive Index	Standard Deviation
50	0.0984	0.0005	1.638	0.001
100	0.0939	0.0008	1.636	0.001
150	0.0925	0.0002	1.636	0.001

As a result, it was observed that as the plasma power is increased, the refractive index did not change within the deviation values, but the growth rate decreased. The plasma power of 150 W was chosen because the lower growth rate as we explained earlier may cause more dense film formation.

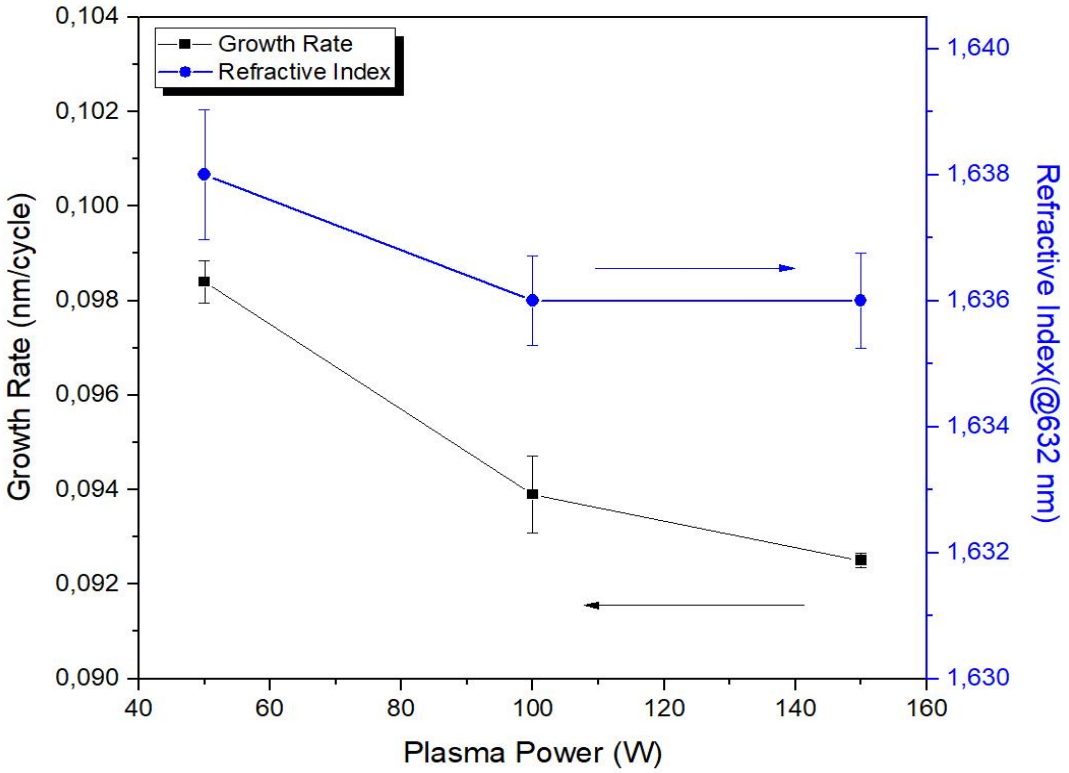

Figure 3.2. *Plasma RF power optimization between 50 and 150 W*

3.1.3. TMA pulse time optimization

TMA pulse times were tried for three different values of 100, 180 and 260 ms. The previous experiments were carried out using a 180 ms TMA pulse time, and the TMA pulse time was investigated by testing the lower and higher values of plasma RF power optimization. The values held constant in this experiment were 300 °C for growth temperature, 150 W for plasma power and 3 s for O_2 pulse time. The growth rates were calculated as 0.0920 ± 0.0002, 0.0925 ± 0.0002 and 0.0918 ± 0.0013 nm/cycle for the TMA pulse times of 100, 180 and 260 ms, respectively. The refractive indices were measured as 1.637 ± 0.001, 1.636 ± 0.001 and 1.635 ± 0.002 for the TMA pulse times of 100, 180 and 260 ms, respectively. These values are given collectively in Table 3.3.

Table 3.3. *Measured refractive index and calculated growth rate in TMA pulse time optimization*

TMA Pulse Time (ms)	Growth Rate (nm/cycle)	Standard Deviation	Refractive Index	Standard Deviation
100	0.0920	0.0002	1.637	0.001
180	0.0925	0.0002	1.636	0.001
260	0.0918	0.0013	1.635	0.002

Figure 3.3 shows the effects of the TMA pulse time on the refractive index and the growth rate. Although the refractive index seemed to decrease as the TMA pulse time increased, there was a higher standard deviation, especially in the 260 ms pulse time in comparison to the others. While emphasizing the growth rate, it may not be stated that there was no tendency, but similarly, as the pulse time increased, higher standard deviations were observed. When TMA is considered not to be a cheap material, the refractive index is higher and the value at which the growth rate does not change can be determined as the most appropriate scenario. For this reason, the TMA pulse time was chosen as 100 ms.

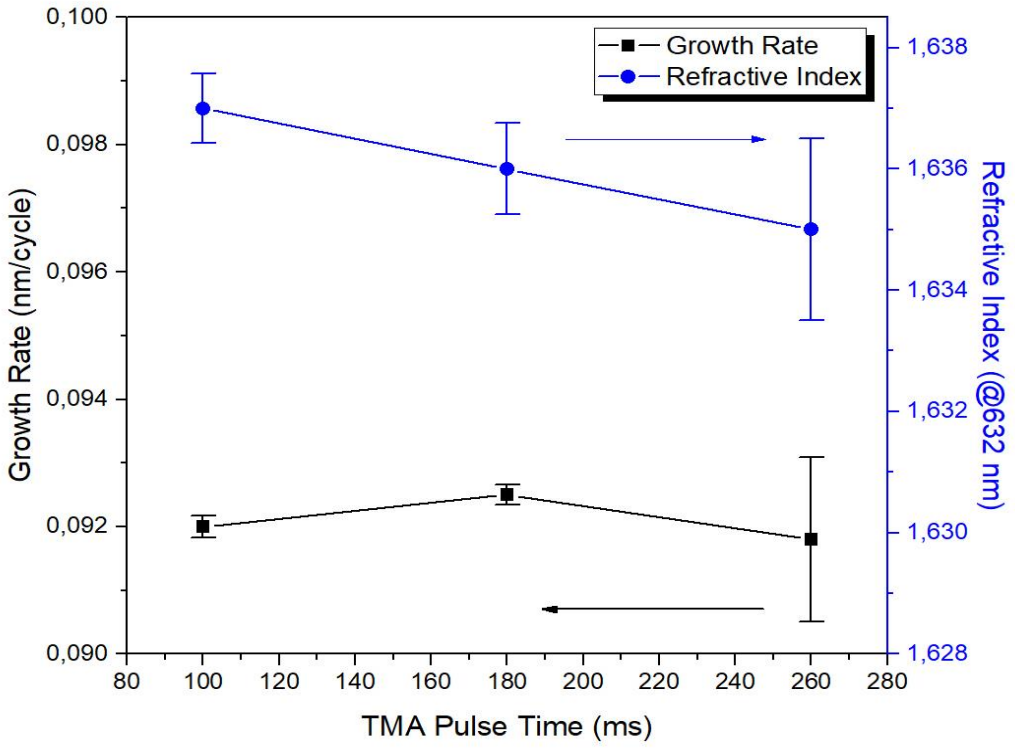

Figure 3.3. *Optimization of TMA pulse time between 100 and 260 ms*

3.1.4. O_2 Pulse time optimization

O_2 pulse time was examined as the last parameter. In the TMA pulse time experiments, the pulse time of O_2 was kept constant at 3 s. The chosen values determined up to now were 300 °C for the growth temperature, 150 W for the plasma RF power and 100 ms for the TMA pulse time. By keeping these parameters constant, the O_2 pulse time was varied as 1, 3, 6, 9 and 12 s. The growth rates were calculated as 0.0958 ± 0.0004, 0.0920 ± 0.0002, 0.0897 ± 0.0009, 0.0880 ± 0.0005 and 0.0869 ± 0.0011 nm/cycle for the O_2 pulse times of 1, 3, 6, 9 and 12 s, respectively. The refractive indices were measured as 1.6360 ± 0.0008, 1.6373±0.0006, 1.6376±0.0008, 1.6368±0.0009 and 1.6373±0.0009 for the O_2 pulse times of 1, 3, 6, 9 and 12 s, respectively.

Table 3.4. *Measured refractive index and calculated growth rate in O_2 pulse time optimization*

O_2 Pulse Time (s)	**Growth Rate (nm/cycle)**	**Standard Deviation**	**Refractive Index**	**Standard Deviation**
1	0.0958	0.0004	1.6360	0.0008
3	0.0920	0.0002	1.6373	0.0006
6	0.0897	0.0009	1.6376	0.0008
9	0.0880	0.0005	1.6368	0.0009
12	0.0869	0.0011	1.6373	0.0009

The values given in Table 3.4 are shown in Figure 3.4 to help observation of the trend. As the O_2 pulse time increased, the growth rate decreased. The refractive index reached saturation at the O_2 pulse time of 6 s. Similar interpretations could be made as to the previous optimizations, and the O_2 pulse time was determined to be 6 s.

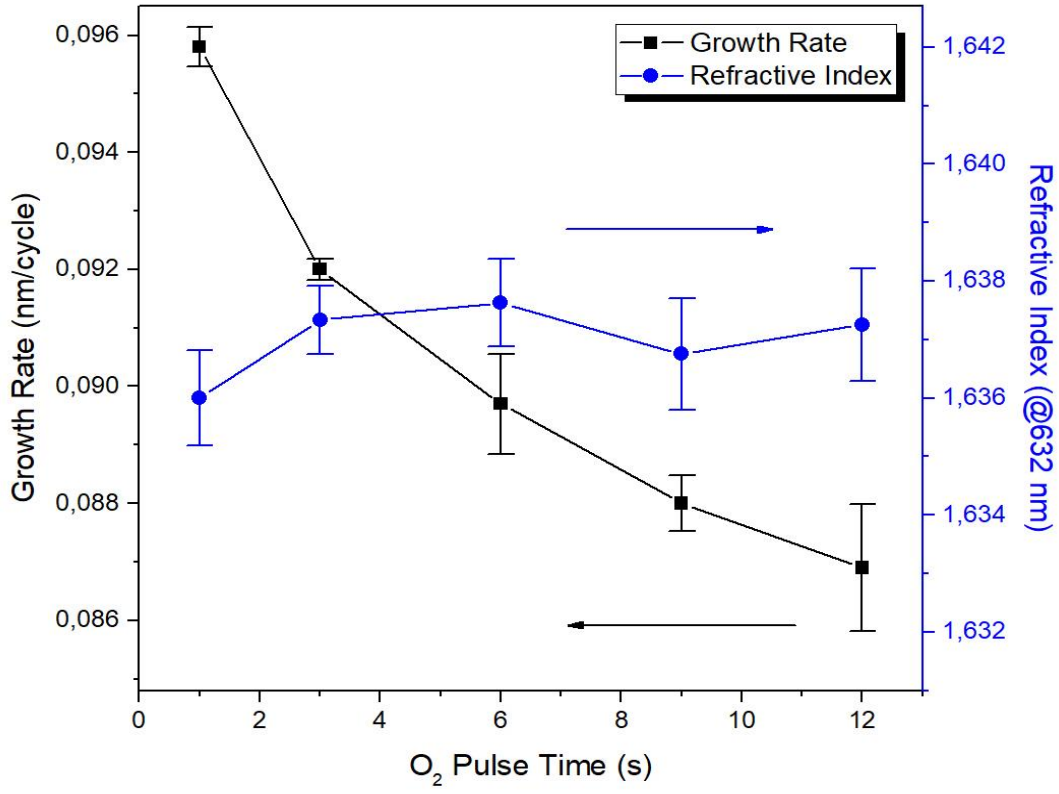

Figure 3.4. *Optimization of O_2 pulse time between 1 and 12 s*

3.2. Growth Optimization of Er_2O_3 using Plasma Enhanced ALD

3.2.1. Literature review

In order to fabricate high-gain optical waveguide amplifier devices, it is necessary to perform an erbium doping process between the passive Al_2O_3 layers. Within the scope of the study, it was decided to optimize the growth of Er_2O_3 prior to addition of pure erbium. For this purpose, a literature review for Er_2O_3 growth was performed by using ALD. Various Er_2O_3 structures have been fabricated in the literature by using plasma enhanced and thermal ALD. Er_2O_3 growth has been demonstrated by using PEALD [102] and, thermal ALD [103]. There are two precursors in the literature for Er_2O_3 growth. These are $Er(thd)_3$ and Er $(CpMe)_3$. These are solid at room temperature. Since they do not have sufficient vapor pressure, they have to be heated to a certain temperature. According to the results of the literature review, Er_2O_3 growth was performed by using $Er(thd)_3$ and O_2 [102], $Er(CpMe)_3$ and H_2O [103, 104] and $Er(thd)_3$ and O_3 [105]. In literature, the $Er(thd)_3$ precursor was heated between 130 and 145 °C. The reason for choosing 145 °C was that $Er(thd)_3$ starts to decompose at 150 °C [102]. $Er(CpMe)_3$ was heated to 120 °C. The pulse times of the erbium precursors were between 1 and 3 seconds

in previous studies [102, 104, 105]. However, in another study [103], the pulse time was given as 30 s. As the reason for it, the researchers pointed to the use of a bubbler system. A summary of the literature survey is given in Table 3.5.

Table 3.5. *Literature review of Er_2O_3*

Ref.	Precursors	Source Temperature	Pulse time	Growth temperature	Growth rate	Material
[102]	$Er(thd)_3$	145 °C	3 s	325 °C	0.2 Å/cycle	Er_2O_3
	O_2 (plasma)	RT	13 s			
	TMA	20 °C	0.2 s		0.85 Å/cycle	Al_2O_3
	O_2 (plasma)	RT	13 s			
[103]	$Er(CpMe)_3$	120 °C	30 s	200 °C	0.25 Å/cycle	Er_2O_3
	H_2O	RT	20 ms			
	TMA	20 °C	20 ms		1 Å/cycle	Al_2O_3
	H_2O	RT	20 ms			
[104]	$Er(CpMe)_3$	Not mentioned	1.6 s	250 °C	1.5 Å/cycle	Er_2O_3
	H_2O	RT	1.5 s			
[105]	$Er(thd)_3$	130 °C	1 s	250-375 °C	0.25 Å/cycle	Er_2O_3
	O_3	RT	2.5 s			

3.2.2. Erbium pulse time optimization and optical measurement

Different experiments were carried out for the pulse time effect of the erbium precursor at 1, 2, 4, 6, 8, 10, 12, 15, 18 and 25 seconds. The number of ALD cycles was 2000 in all experiments. The refractive index and thickness measurements of these experiments at λ=1550 nm were performed by a spectroscopic ellipsometer at National Nanotechnology Research Center (UNAM). Figure 3.5 shows these results.

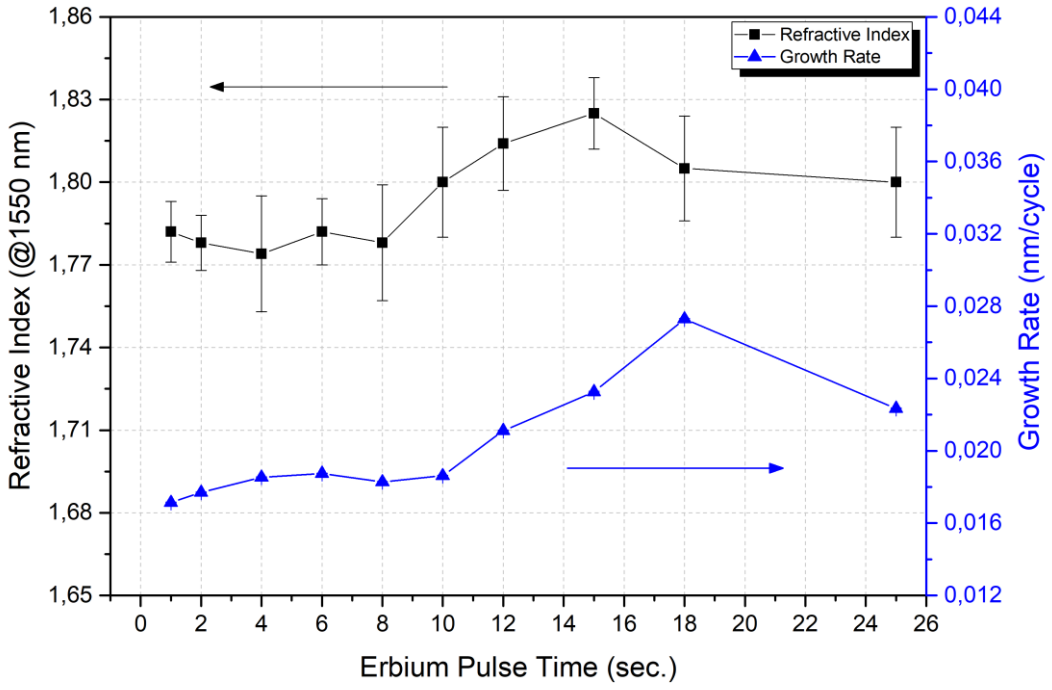

Figure 3.5. *Influence of the change in erbium precursor pulse time on the refractive index and growth rate*

The results of the thickness measurements were in the range of 34-55 nm. The growth rate of Er_2O_3 was very low. The highest growth rate was calculated as 0.027 nm/cycle for a pulse time of 18 seconds. The refractive indices were measured to be between 1.74 and 1.825. The standard deviations of the refractive indices were high as understood in Figure 3.5. The highest refractive index was measured as 1.825 ± 0.013 at a pulse time of 15 seconds. It is more important in electromagnetic waveguides due to the positive effects of the refraction index such as the increase in the confinement factor or the decrease in the total thickness. Therefore, the doping experiments were carried out again by selecting the pulse time of 15 seconds.

3.3. Erbium Doped Planar Waveguide Amplifier

3.3.1. Hetero-cycle definition and initial growths

Before the fabrication of the waveguide amplifier device, it was necessary to determine the variations of some of the parameters such as the thickness, refraction index and the successive growth rate of the Al_2O_3-Er_2O_3 layers according to the cycle ratios between these two materials, by growing them at a certain reference thickness.

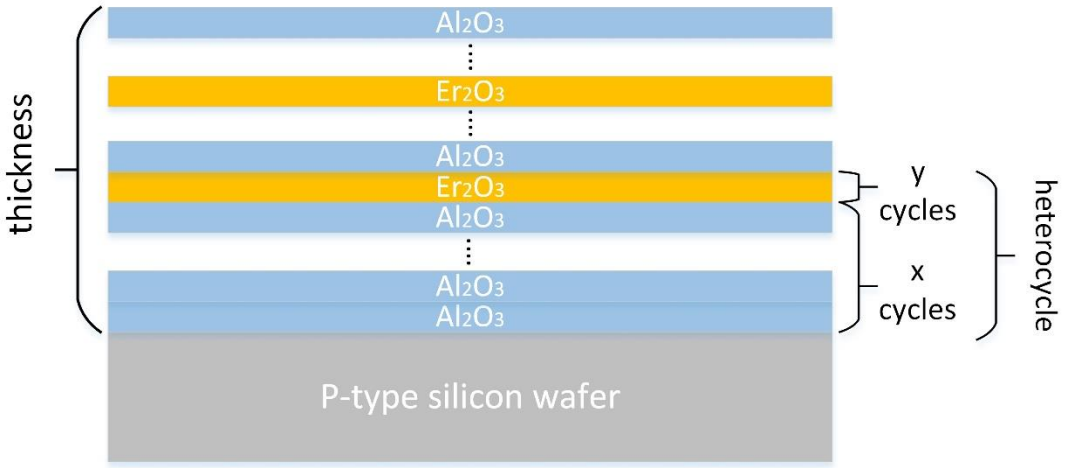

Figure 3.6. *Hetero-cycle for the growth of Al_2O_3:Er_2O_3 (x:y) films*

Figure 3.6 shows the representation of the hetero-cycle and thickness of the deposited film as a function of the number of ALD cycles. The hetero-cycle consisted of x Al_2O_3 cycles and y Er_2O_3 cycles. Active structures with various Er^{3+} concentrations were synthesized by changing the cycle ratio. The cycle ratio describes the ratio between the numbers of x and y cycles. Films with x:y cycle ratios of 5:1, 1:1, 1:5, 5:5 and 5:10 were synthesized. The PL in the visible spectrum was measured again by changing the cycle ratios.

Table 3.6. *Measurements of thickness and refractive index of samples grown at different cycle rates*

Cycle Ratio (Al_2O_3:Er_2O_3)	**Number of Cycle**	**Measured Thickness (nm)**	**Growth Rate (nm/cycle)**	**Refractive Index (λ=1550 nm)**
5:1	187	102,31	0,620	1,654
1:1	526	95,96	0,182	1,649
1:5	165	51,36	0,275	1,692
5:5	105	77,40	0,737	1,669
5:5	525	342,27	0,647	1,674
5:10	68	52,46	0,772	1,683

After the experiments were carried out, the calculations of the growth rates were investigated with ellipsometry measurements in UNAM. The results obtained for the determined grown samples are given in Table 3.6. The effect of the number of cycles was also investigated in the 5:5 sample. For the 5: 5 sample, the thicknesses of the samples with a cycle rate of 105 and 525 were measured at 77, 40 and 342.27 nm. There was a 5-

fold increase in the cycle rate at a 4.4-fold increase in the thickness value. This should be considered while expanding thick samples. However, this should be confirmed for each different doping. Since this situation will be lost both in terms of time and cost, PL measurements of these samples may be taken, and only this trend of the related sample may be taken into consideration. The refractive index and the growth rate variations of the Er^{3+}:Al_2O_3 layers are given in Figure 3.7.

The refractive index of the erbium doped Al_2O_3 layers showed an increase of 0.01 in comparison to the undoped Al_2O_3 (n_{Al2O3}=1.639 @1550 nm) grown by using PEALD. The reason for this was that the refractive index of the doped Er_2O_3 (n_{Er2O3}=1.830 @1550 nm) was higher than the refractive index of the Al_2O_3. Clearly, it was observed that the cycle ratio caused a significant change in the refractive index value. Furthermore, the highest refractive index was in the sample with the 1:5 cycle ratio possibly due to the high erbium concentration.

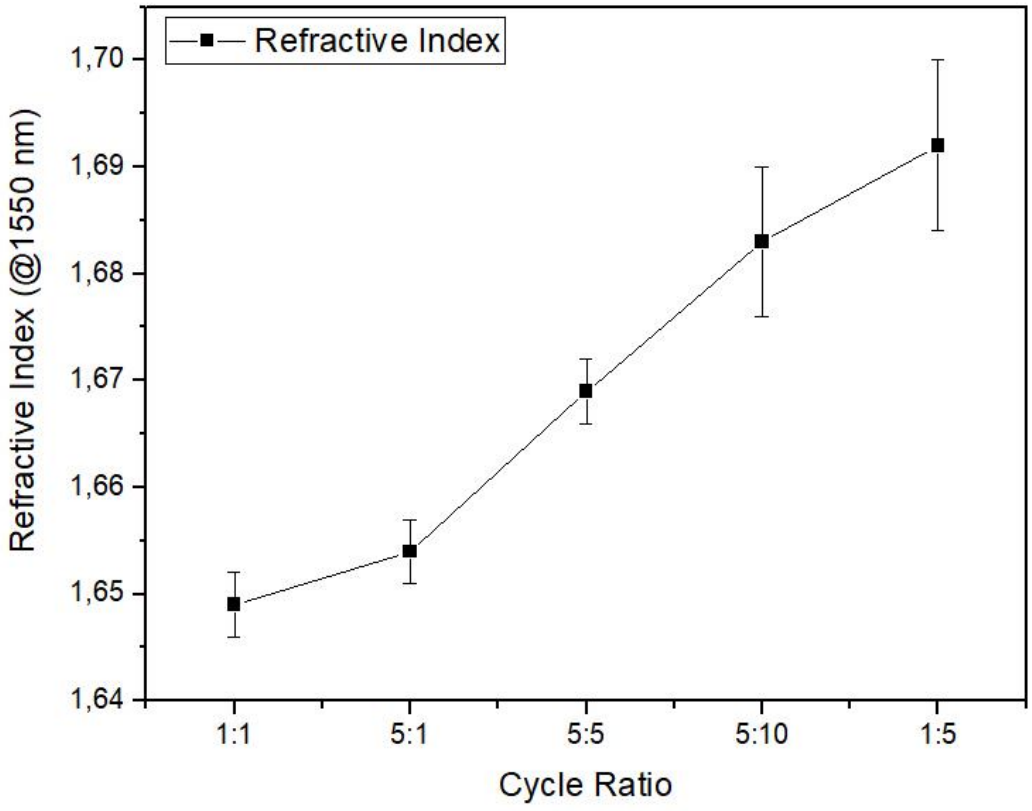

Figure 3.7. *Refractive index at λ=1550 nm versus cycle ratio*

3.3.2. PL Measurements in the visible spectrum

Once the characterization samples were fabricated, PL measurements in the visible spectrum were performed using Raman centered at 550 and 660 nm, which are previously known by the state transitions, and the relationship between the compositions is demonstrated. PL measurements are a guiding characterization technique that we use to prove the presence of active erbium ions in the structure and which energy state the electrons of these active ions pass through. Measurements were taken with a 30 mW 532 nm laser and 1 ms integration time for an average of 20 times. Considering the measurement limits of the Micro-Raman tool from which we measured the PL measurement, Er^{3+} ions were observed to emit at two different wavelengths, 535-570 and 630-720 nm. Er^{3+}: Al_2O_3 structures radiate probably at 1550 nm, but since the device limits are up to 800-850 nm, this emission was not observed. No radiation was observed under the excited wavelength. This result was proof that there is no up conversion mechanism, which explains that the radiation at frequencies higher than the excited frequency did not occur between energy states.

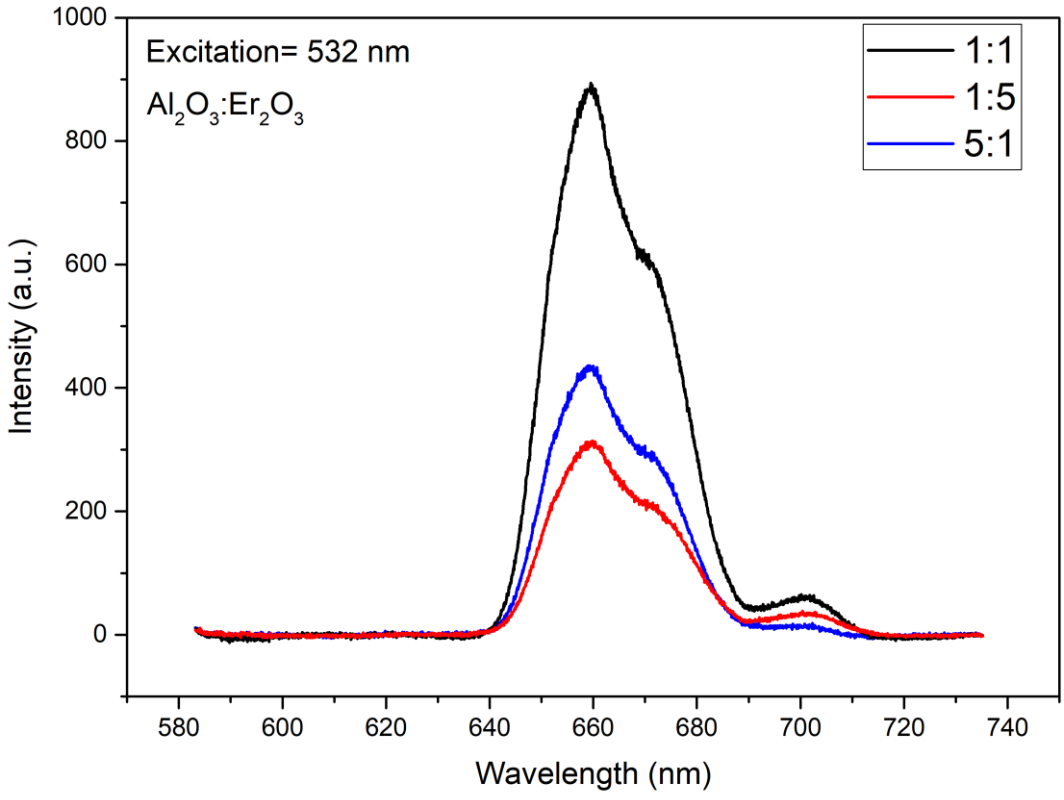

Figure 3.8. *PL measurements at 660 nm for 1:5, 1:1 and 5:1 cycle ratios*

The PL measurements of the 1:5, 1:1, and 5:1 samples are compared in Figure 3.8. These measurements were the result of having the highest PL intensity at the 1:1 cycle ratio. In order to further incensement in the PL intensity, the ratio was kept fixed, and the corresponding cycle numbers were increased. The sample at the 5:5 cycle ratio was grown. PL intensity increased in the sample grown with the 5:5 cycle ratio. Additionally, a sample with a 5:10 cycle ratio was used to try to maximize the PL intensity. This increase in the Er_2O_3 cycle rate resulted in a reduction in PL intensity of about four times. The PL comparisons of the samples with the 1:1, 5:5 and 5:10 cycle ratios are given in Figure 3.9.

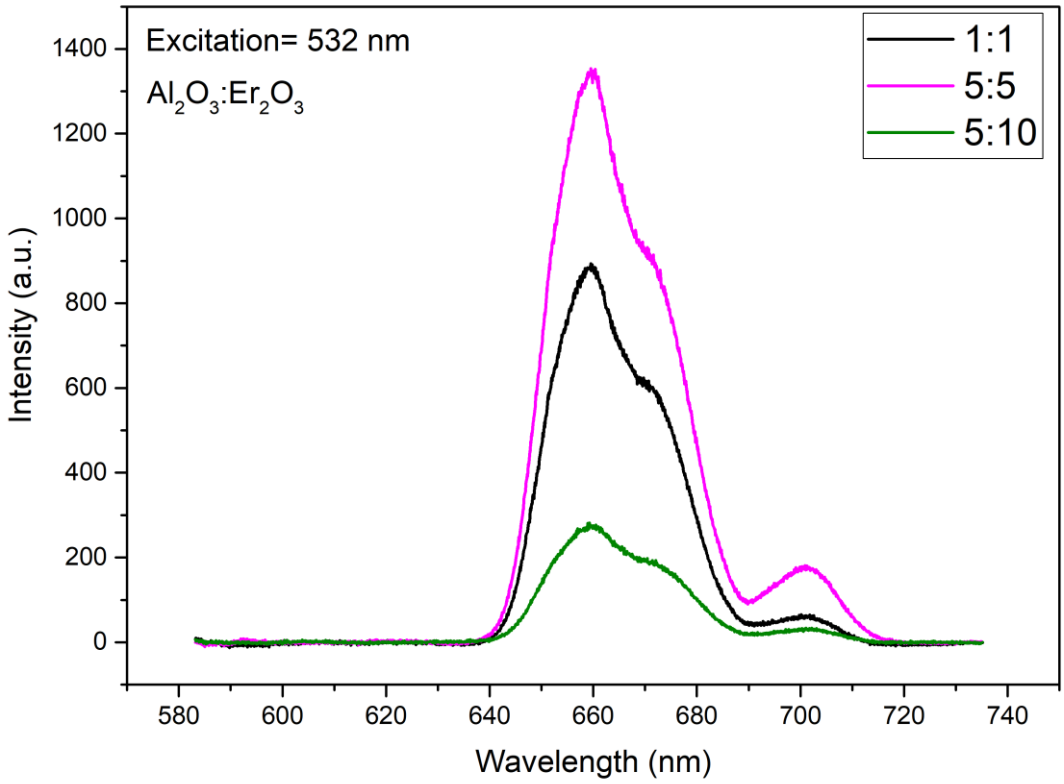

Figure 3.9. *PL measurements at 660 nm for 1:1, 5:5 and 5:10 cycle ratios*

Based on the results shown in Figure 3.9, the sample was selected for waveguide fabrication with a 5:5 cycle ratio at which the maximum PL intensity was obtained. A growth experiment with a number of 525 cycles was realized by setting 500 nm as the target thickness. The PL comparisons of the samples with the cycles of 105 and 525 with 5:5 cycle ratios are given in Figure 3.10. It was observed that, as the cycle rate increased,

the PL intensity also increased. A five-time increase in the cycle ratio would cause a two-time decrease in the PL intensity.

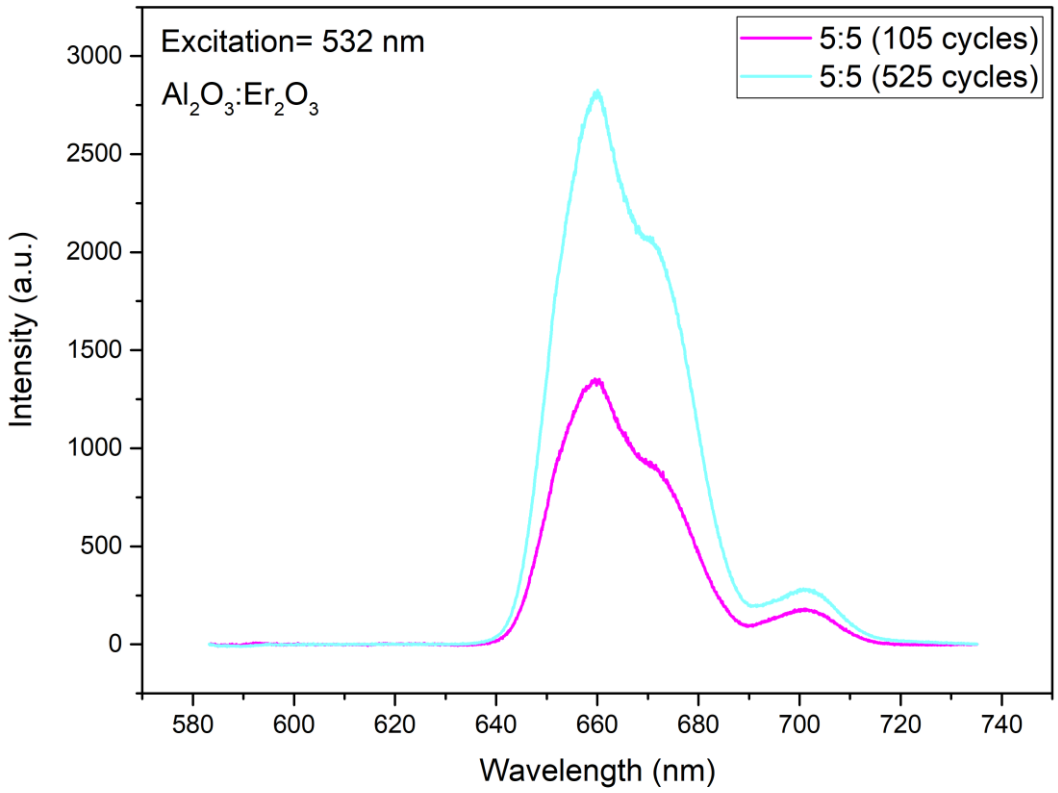

Figure 3.10. *PL measurements centered at 660 nm for samples with 5:5 cycle ratio grown by different numbers of cycles*

PL measurements centered at 550 nm of all the samples are given in Figure 3.11. Except in one case, where the results obtained with those centered at 660 nm showed a similar tendency. The PL at 660 nm increased with the number of cycles; however, there was no effect of PL on the samples centered at 550 nm of the increase in the cycle ratio.

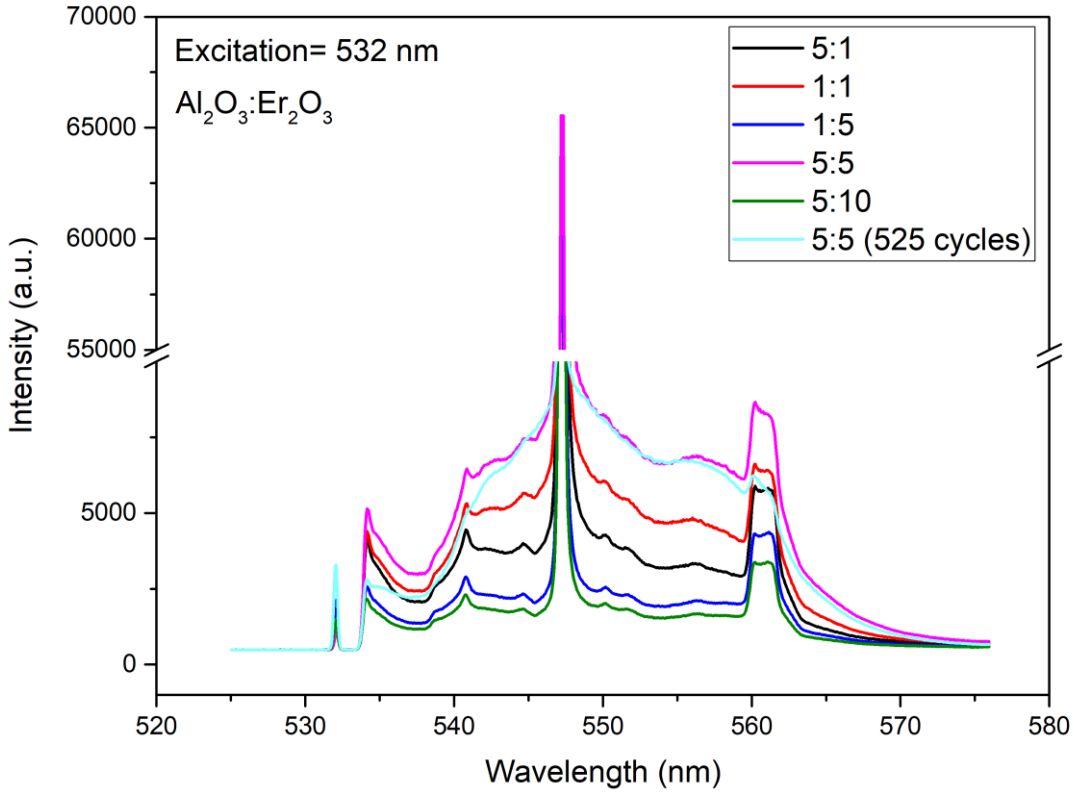

Figure 3.11. *PL measurements at 550 nm for 1:5, 1:1, 5:1, 5:5, and 5:10*

Al_2O_3:Er_2O_3 layers were grown on a 4-inch Si\SiO_2 substrate with 1050 cycles, and PL measurements were taken from the points determined on the sample given the homogeneity test results. These points were the same points as the thickness measurement points. The PL measurements at 660 nm are given in Figure 3.12. The highest PL intensity was measured at the input. The center, right and left were measured in close proximity to each other while the lowest intensity was at the output. The results showed that the intensity increased with thickness.

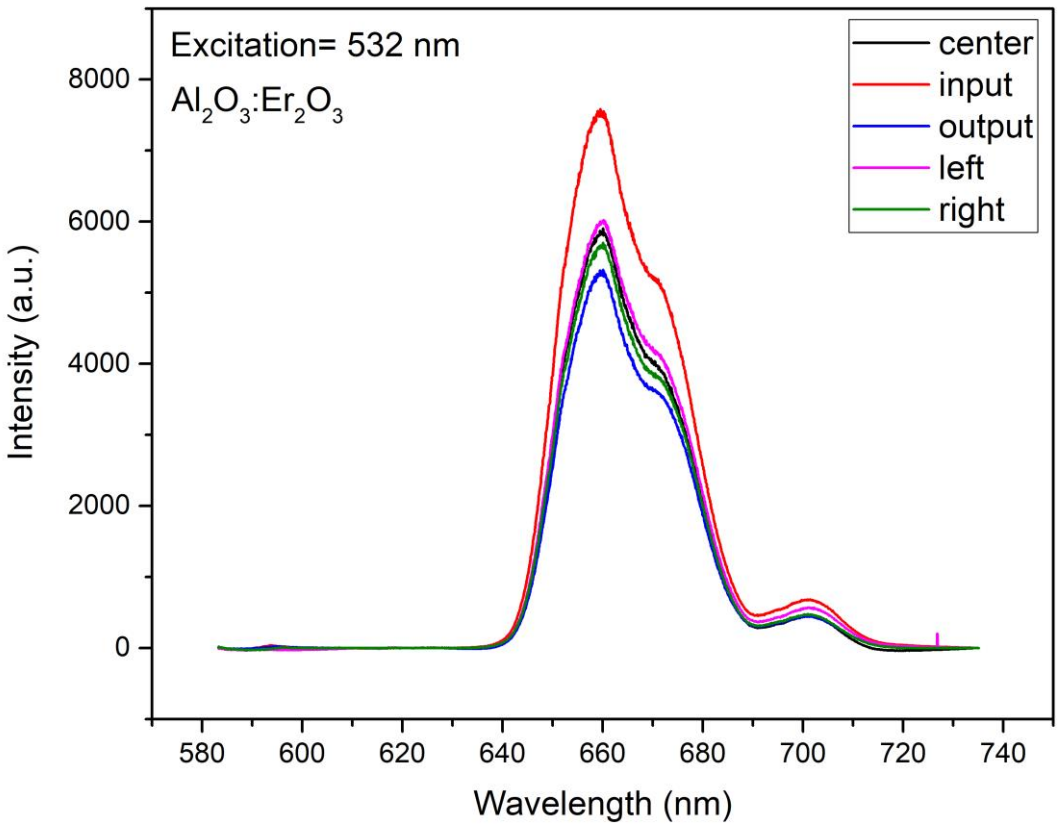

Figure 3.12. *PL measurements are taken from the input, output, center, right and left sides of the active structure grown on a 4-inch Si\SiO₂ substrate with a 5:5 cycle ratio and 1050 cycles*

The representation of the transitions between the energy bands which refers to emissions at the range of 630-720 nm is given in Figure 3.13. The upward green arrow indicates the excitation laser at 532 nm, which was used to activate the erbium ions. The downward black arrows indicate the non-radiative transition between energy bands. Consistent with the colors in the peak decomposition, 65x, 67x and 69x nm radiative transition is represented with the red, dark green and blue colored arrows, respectively. The doublet bands 656-657/671-672 nm and the singlet band 694-695 nm were assigned to the ${}^{4}F_{9/2} \rightarrow {}^{4}I_{15/2}$ and ${}^{2}H_{9/2} \rightarrow {}^{4}I_{11/2}$ transitions, respectively.

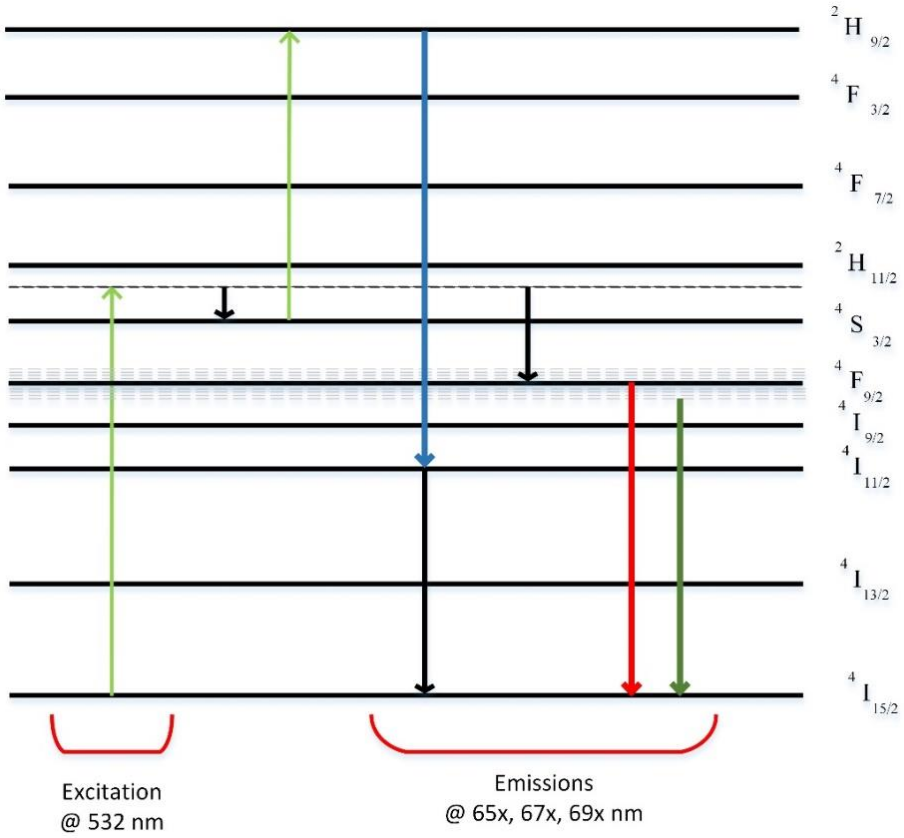

Figure 3.13. *Demonstration of the transition between energy states of three different centers at 65x, 67x and 69x nm*

The active erbium ions were excited by the 532 nm laser between the $^2H_{11/2} - {}^4S_{3/2}$ bands. They transited to the $^4F_{9/2}$ band without radiation (non-radiative transition). After this, they switched to $^4I_{15/2}$ (ground state) with radiation (radiative transition). These transitions may be described to be 65x and 67x nm centers, which were the result of peak decomposition. Another transition mechanism was that active ions that were excited between the $^2H_{11/2} - {}^4S_{3/2}$ states switched to the $^4S_{3/2}$ state without radiation. When the ions were in this band, they were excited again, with a 532 nm laser and they switched to the $^2H_{9/2}$ state. The active ions passed through $^4I_{11/2}$ by radiation of 69x nm light from $^2H_{9/2}$. Finally, they switched from this band to the ground state without radiation.

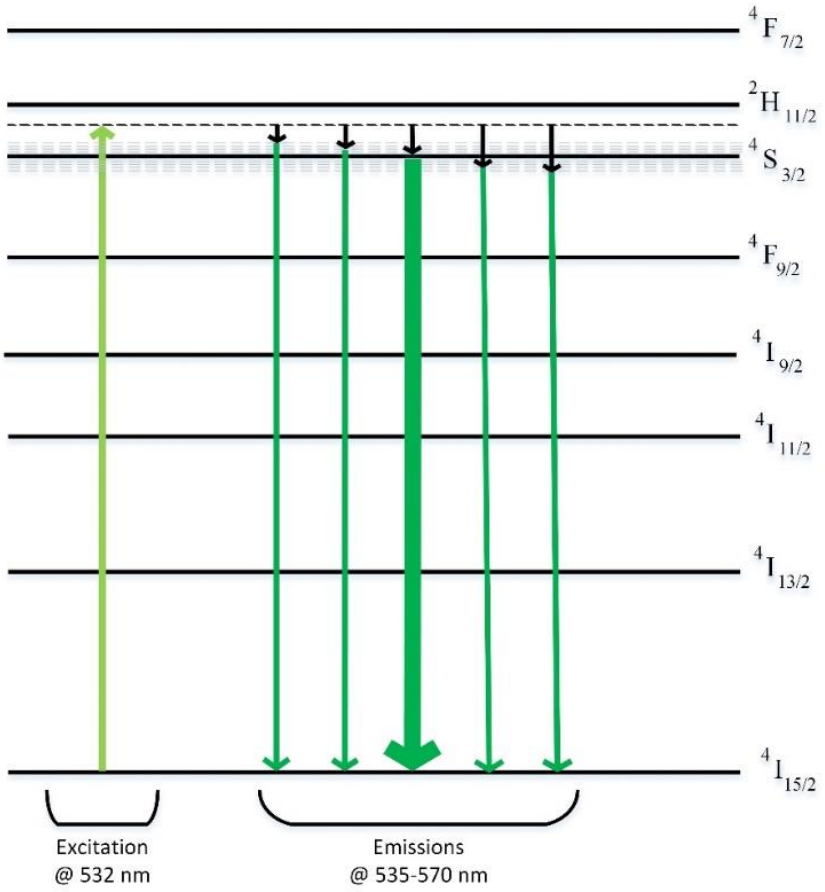

Figure 3.14. *Demonstration of the transition between energy states in the range of 535-570 nm*

According to the literature review, all the observed transitions could be related to the transition between the bands of $^4S_{3/2} \rightarrow {}^4I_{15/2}$. In general, only the 547 nm-centered radiation appears in the literature. The main reason for this is that the intensity of this transition is very high and it suppresses other transitions. If the vertical axis of Figure 3.11 had not had a break, it would not be possible to show low-intensity transitions. It already shows the transition between the same bands. Other low-intensity peaks are transitions between the low-probability bands around the $^4S_{3/2}$ band but belonging to the $^4S_{3/2}$ band. Figure 3.14 shows the representation of transitions between the states of the radiation given in Figure 3.11. The upward-pointing arrow, which is shown with a light green color, refers to the excitation laser, and the black down arrow, represents non-radiative transitions. The downward-pointing arrows, which are shown with dark green, refer to the transition between the bands of $^4S_{3/2} \rightarrow {}^4I_{15/2}$. The thick dark green arrow

indicates that the center of radiation was 547 nm, and it was about 8 times more severe than the others were.

The following results were obtained according to the PL analyses;

1. PL measurements were obtained in the intervals of 530-570 and 630-720 nm.
2. Compared to these measurements, the PL intensities in the range of 530-570 nm were higher than the PL intensities in the range of 630-720 nm.
3. When the radiation peaks at 630-720 nm were separated by the peak decomposition method, three peaks were separated for all cycle ratios, the centers of these peaks were 65x, 67x and 69x nm.
4. When the PL intensities were compared, it appeared that the highest intensity belonged to the 5:5 cycle ratio.

3.3.3. Annealing effect on visible PL

Planar samples with different doping ratios were annealed at different temperatures, and a comparison was based on the peak of their emission at 660 nm. The relationship between the annealing temperature and the doping ratio was investigated. By means of this relationship, it is possible to learn which doping ratio makes maximum emission at which temperature. However, the point to be considered is to obtain maximum emission without crystallization of the structure. Because when the structure crystallizes, birefringence occurs and causes an additional optical loss in the waveguide. The relationship between temperature and PL is shown in Figure 3.15. Annealing temperatures of 200, 400, 600 and 800 ° C were used.

The samples at the doping ratios of 1:5, 5:5 and 5:10 showed similar behaviors. The emission measured from these samples decreased to 600 °C and showed higher emission in the as-grown structures at 800 °C. The samples with the doping ratios of 1:1 and 5:1 exhibited a higher emission than the as-grown structures when annealed at 200 ° C. Then, a decrease of up to 600 °C was observed, and similar to the other samples, the maximum emission was at 800 °C. Achieving the maximum radiation at 800 °C may be related to the start of Al_2O_3 crystallization at 800 °C. The optical amplifier device was fabricated using a sample with the 5:5 doping ratio. The 5:5 doping ratio belonged to the highest PL in the as-grown structure obtained without crystallization. Therefore, the amplifier device was fabricated using the as-grown structures.

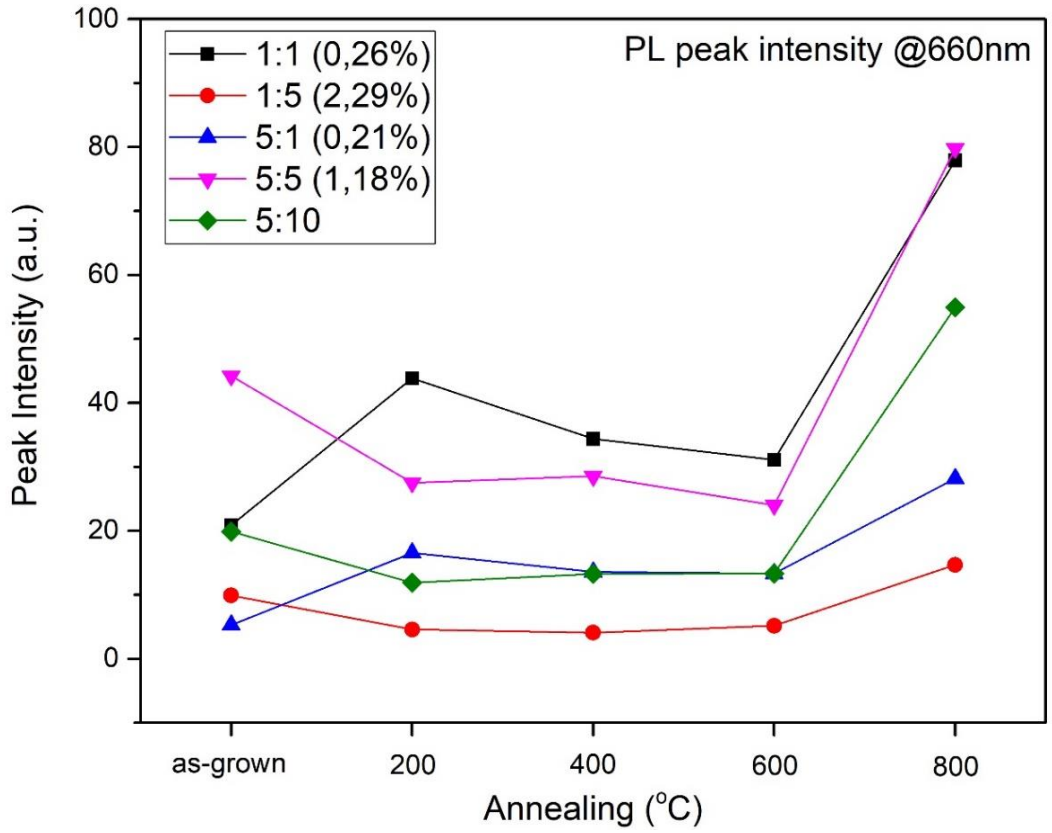

Figure 3.15. *Annealing effect on PL intensity*

3.3.4. The thickness, refraction index and uniform growth tests

Based on the PL measurements, it was decided to fabricate the active device with the 5:5 cycle ratio. With this cycle ratio, a growth was facilitated with 525 cycles for the target thickness of 500 nm that supports only the fundamental mode. A prism coupler needs one of the thickness or refractive index values as a reference to calculate the other parameters for single-mode measurement. The refractive index of the samples grown with the erbium pulse time of 10 seconds, which was at 50 nm, was measured as 1.645 with an ellipsometer. When it was considered, the thickness of the 525 cycles sample was measured as ~510 nm. In order to obtain accurate information on the thickness and refractive index measurements with the prism coupler, it is necessary to support more than one optical mode. For this purpose, the number of cycles was increased to two-times, which was 1050 cycles. Four-quarter p-type silicon, two 525 cycles grown samples and one 4-inch Si\SiO_2 substrate were placed into the reaction chamber. The placement scheme is given in Figure 3.16.

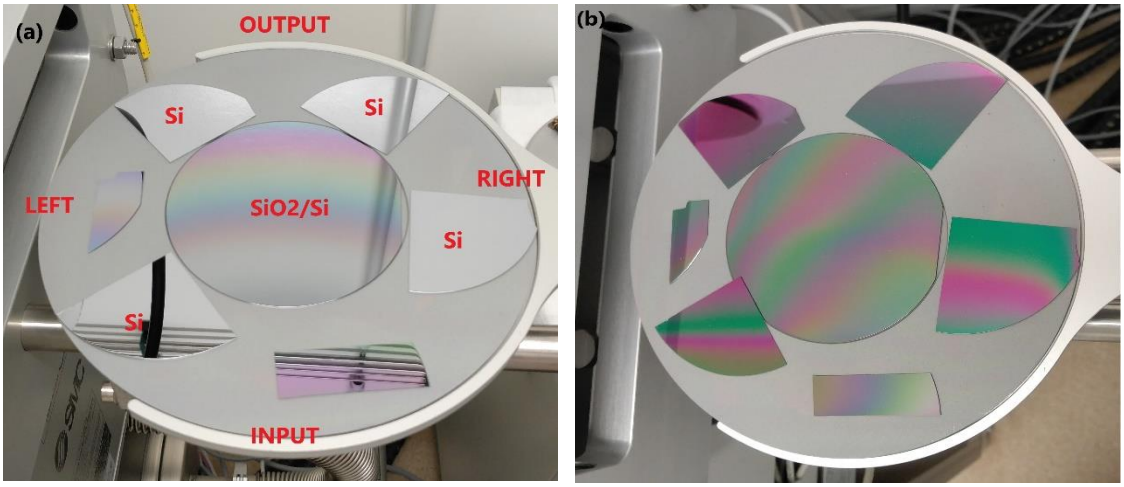

Figure 3.16. *The growth placement scheme for 1050 cycles a) before b) after*

One of the previously grew samples with 525 cycles was placed at the input, and the other was placed on the left side. The prism coupler could not measure the silicon samples because the refractive index did not satisfy the TIR conditions. The 4-inch all-in-one measurement was made at five different points: input, output, left, right and center. Measurements were taken at the input and on the left-hand side of the sample grown by 525 cycles. The results obtained with the prism coupler are given in Table 3.7.

Table 3.7. *The results of thickness and refractive index by prism coupler*

Substrate	**Location**	**Refractive Index (n)**		**Thickness (µm)**
		@633 nm	**@1549 nm**	
$Si\backslash SiO_2$	Input	1.687	1.673	~0.77
	Output	1.695	1.672	~0.64
	Left	1.695	1.676	~0.65
	Right	1.691	1.671	~0.70
	Center	1.689	1.673	~0.71
$Si\backslash SiO_2\backslash Al_2O_3{:}Er_2O_3$ (525 cycles)	Input	1.672	-	~1.40
$Si\backslash SiO_2\backslash Al_2O_3{:}Er_2O_3$ (525 cycles)	Left	1.692	-	~1.00

The high accuracy measurement results are given in Table 3.7 due to multi-mode support at λ=632 nm. The refractive indices at λ=632 nm for Si\$SiO_2$\$Al_2O_3$:$Er_2O_3$ were 1.687, 1.695, 1.695, 1.691 and 1.689 for the input, output, left, right and center, respectively. The refractive indices at λ=632 nm for Si\$SiO_2$\$Al_2O_3$:$Er_2O_3$ were 1.673, 1.672, 1.676, 1.671 and 1.673 in the same order. The thicknesses were respectively 0.77, 0.64, 0.65, 0.70 and 0.71 μm. It was observed that the precursor input of the reaction chamber was thicker than those in the other locations. Growth on the center and right could be included in this case. Moreover, in similar positions, lower refractive indices were measured in comparison to others. The refractive indices of Si\$SiO_2$\$Al_2O_3$:$Er_2O_3$ (525 cycles) were 1.672 and 1.692 for the input and left sides, respectively. The thicknesses were 1.40 and 1.00 μm in the same order. These results showed a similar tendency to the results obtained from the Si\$SiO_2$ substrate. The inlet of the reaction chamber was of higher thickness and lower index, while the left side was of lower thickness and higher index. The mean thickness was 0.694±0.052 μm and the mean refractive index was calculated as 1.691±0.004. Growth uniformity was calculated as 5.23% for thickness and 0.4% for the refractive index. Based on the results, the mean growth rate for the 5:5 cycle ratio was calculated to be 0.66 nm. In this case, the number of ALD cycles required for 1 μm of growth was calculated as 1510.

3.3.5. XPS analysis of active structures

The samples that were grown with the 1:1, 1:5, 5:1 and 5:5 cycle ratios were selected for atomic composition analysis which was performed by using X-ray photoelectron spectroscopy (XPS) available at Bilkent University in UNAM. The samples were etched with Ar^+ ions for 60 seconds after each step until the silicone was reached and composition analyses were performed at each step. Thus, the percentages of the elements were observed at different depths. Carbon (C 1s) was observed as expected from the first measurement taken from the surface and the carbon disappeared as a result of the 60-second etching process. Figure 1 shows the XPS energy spectrum taken from the surface of the 1:1 sample. Calculations on the percentage of atomic concentration were made by considering the peak areas by Er-4d for the Erbium, Si-2p for silicon, Al-2p for aluminum and O-1s for oxygen. The KLL peaks mentioned in the spectrum represent the energy of the electrons ejected from the atoms due to the filling of the O-1s

state (K shell) by an electron from the L shell associated with the ejection of an electron from the shell L of the respective element. Plasmon peaks can be observed for some elements. These peaks cause energy losses due to the interaction of photoelectrons with other electrons. Hence, these peaks are called elemental lost or Plasmon peaks. These peaks were encountered and indicated for Aluminum and Oxygen in the spectrum. Since the spectrum in Figure 3.17 belonged to the surface, the silicone peak did not appear. When the silicone was reached, it was observed that the silicon had a Plasmon peak and this peak partially overlapped with the Er-4d peak. This is a further confirmation that the silicon was reached, and the calculation of the concentration of erbium was taken into account in this computation due to the fact that the % concentration was calculated according to the scanned area. The spectra of the other samples were similarly evaluated.

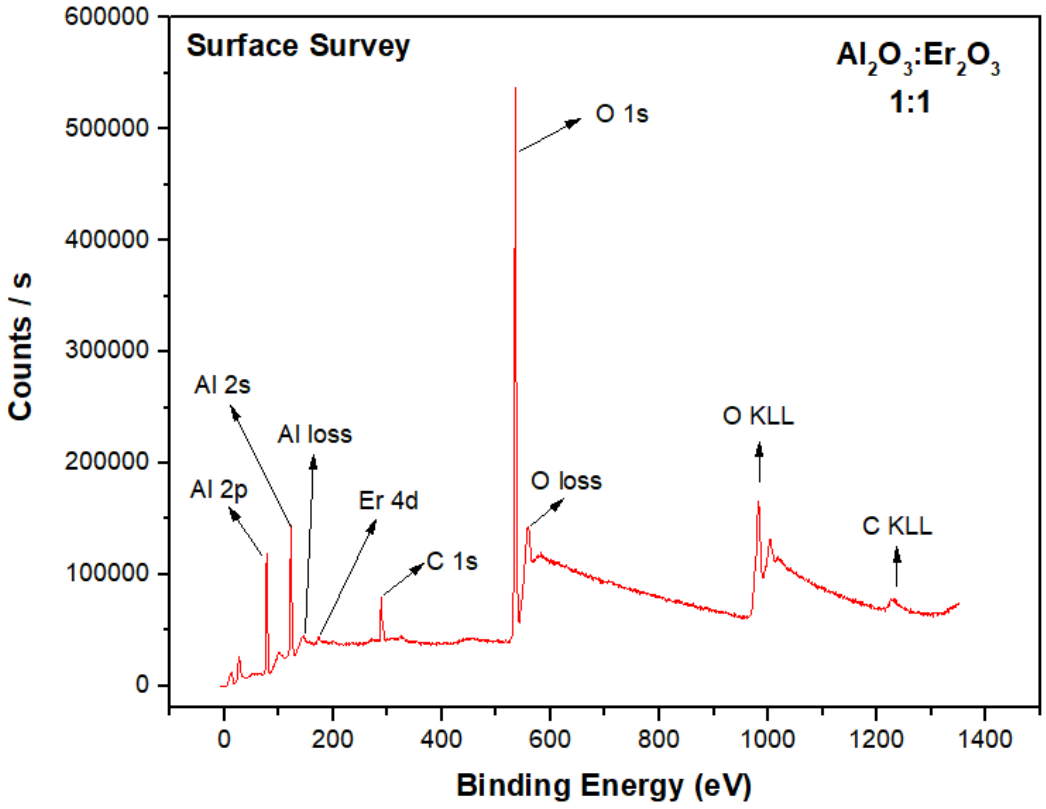

Figure 3.17. *Energy spectrum from the surface of the 1:1 sample*

For the 1:1 sample, the binding energies of each element in seconds were analyzed. These were measured from the surface, after the first two etching processes after the surface (60 and 120 seconds), two measurements at the time of reaching the silicone (1860 and 1920 seconds) and once the silicone was reached (2280 seconds). These

measurements are given in Figure 3.18. In general, when the peak position was examined, there was some shift in the first measurement taken from the surface, then only the peak amplitude was changed in the measurements taken. Figure 3.18a shows the peak used for the % concentration calculation for Er_2O_3. The binding energy for Er_2O_3 was in the range of 170-175 eV. As the etching approached silicon, this peak shifted to the 160-165 eV band. As a result of the literature research, it was understood that this shifted peak belonged to the previously mentioned silicon plasmon loss. Si plasmon and Er_2O_3 peaks overlapped. Since % concentration calculations were made according to the scanned area, this situation was considered in order to minimize the error caused by slippage. Figure 3.18b shows the peak change of the binding energy of the Si-2p peak. While this peak did not appear near the surface, it occurred in the case of progressive etching. Note that when it was about 1860 and 1920 seconds to reach the silicon, a weak peak appeared in the 103-105 eV band and then disappeared. Figures 3.18c and d show the peak of the elements Al and O, respectively. It is possible to say similar things regarding both. If the surface measurement were not taken into consideration, peak intensity decreased as the silicon approached. The ratio of oxygen to aluminum, due to the structure of Er_2O_3, could be said to have a slightly higher peak intensity.

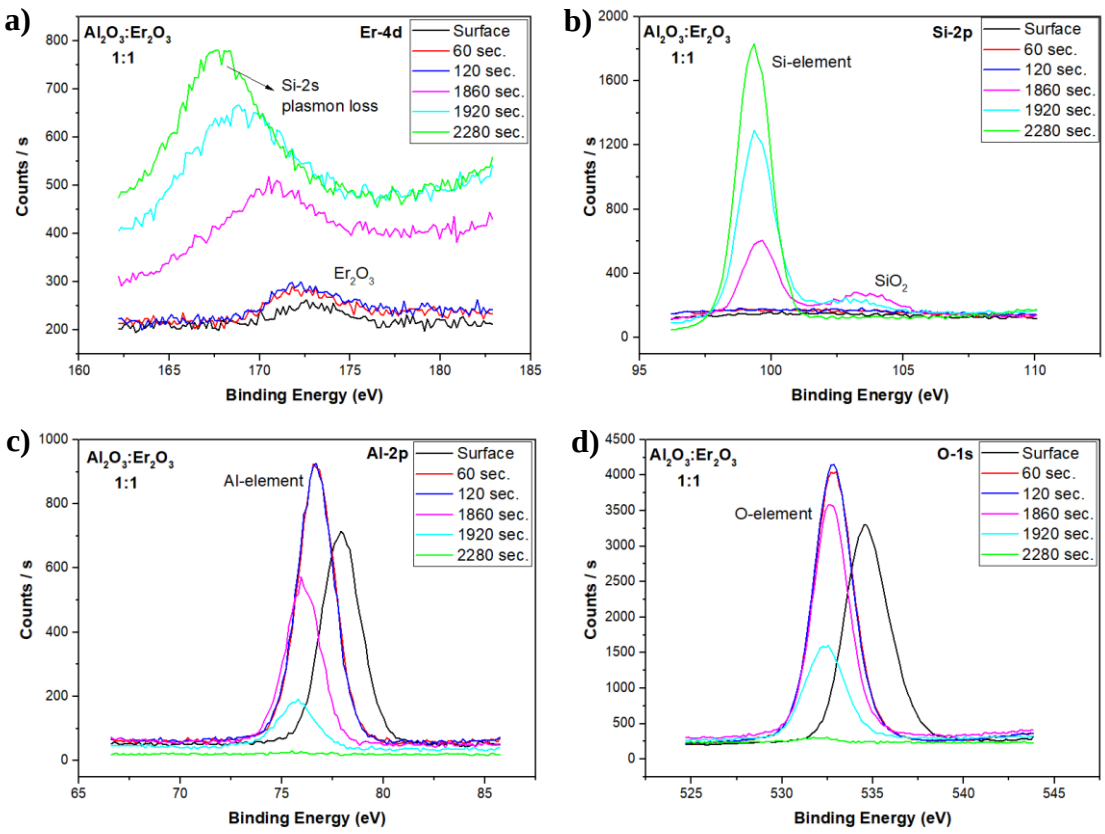

Figure 3.18. *Variation of the binding energy peaks at different etching times of 1:1 a) Er-4d b) Si-2p c) Al-2p d) O-1s*

Figure 3.19 shows the variation of the percentage change of the erbium-doped samples depending on the etch depth. After each etching process, the spectrum was analyzed to determine the % concentrations. The etching operations were continued until they reached the substrate. Thus, concentration measurements were made according to the etch depth profile. In general, oxygen and aluminum concentrations remained constant until they approached silicon. Erbium concentration showed an increase while approaching the silicon. Stoichiometry calculation of Er_2O_3 was not performed due to the fact that the Erbium concentration was very low, and the margin of error was high.

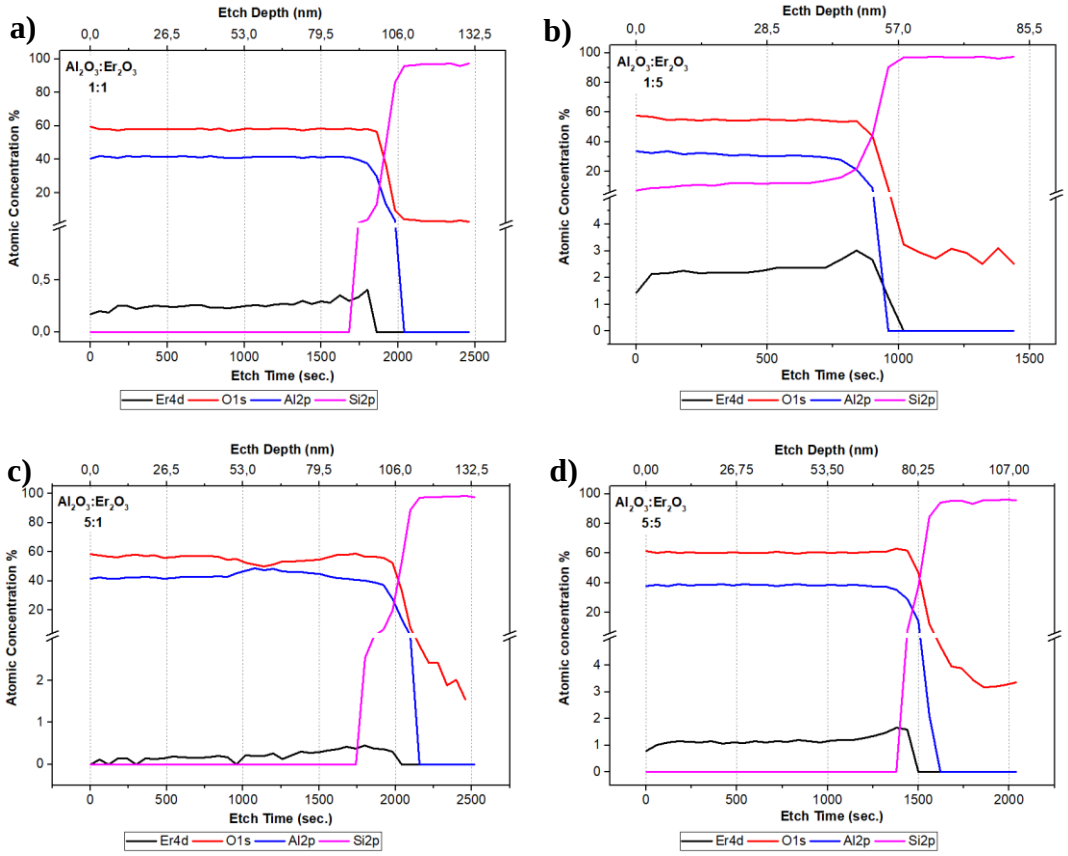

Figure 3.19. *% atomic concentration versus etch depth a) 1:1 b) 1:5 c) 5:1 d) 5:5*

The mean % atomic percentages were calculated without considering the surface and measurements after the silicon was reached. In the 1:1 sample, Erbium was found as 0.26%, Aluminum was found as 41.26%, and Oxygen had a share of 58.09%. In the 1:5 sample, Erbium was found as 0.21%, Aluminum was found as 43.26%, and Oxygen was found to be 55.78%. In the 5:1 sample, Erbium was found as 2.29%, Aluminum was found as 29.22%, and there was 55.78% Oxygen. In the 5:1 sample, Erbium was found as 1.18%, Aluminum was found as 37.90%, and Oxygen was found as 60.62%. A better understanding of these values is given in Table 3.8. The highest etch rate and the Erbium concentration belonged to the 1:5 ratio. The lowest etch rate belonged to the 1:1 ratio and the lowest Erbium concentration belonged to the 5:1 ratio.

Table 3.8. *Atomic concentration (%) and XPS etch rate of samples with different doping ratios*

		Al_2O_3: Er_2O_3			
		1:1	**5:1**	**1:5**	**5:5**
Atomic Concentration %	**Erbium**	0,26	0,21	2,29	1,18
	Aluminum	41,26	43,26	29,22	37,9
	Oxygen	58,09	55,78	54,27	60,62
	Silicon	-	-	14,21	-
	Etch Rate (nm/min)	3,17	3,2	3,4	3,21

The results showed that the erbium concentration increased as the erbium cycle rate increased. In the 1:5 sample which had the highest erbium concentration, unlike the other samples, the signal was received from all the elements at every moment of the measurement. This could be an indication of the complexity of a nested structure. When the PL measurements were examined again, and this sample with the lowest PL intensity could be associated with a more irregular structure in comparison to the other samples in transition between the states. A linear correlation was found between the % atomic and absolute concentrations of the RBS measurements in the data for erbium. The equation is given below. Equation 3.1 is based on the assumption that the erbium distribution is uniform [106]. Since uniformity is less than 1% in the ALD technique, the accuracy of the equation increases even more.

$$N_{Erbium} = (9.02 \times 10^{20}) \times N_{Erbium,atomic\,\%} \quad (3.1)$$

Using the equation above, the absolute erbium concentration (N_{Erbium}) in all samples was calculated. The results on the absolute concentrations are given in Table 3.9. The change of the observed refractive index and Al/O ratios with the absolute concentration value obtained in the structure were investigated. The Al/O ratio and change of refractive index as a function of the absolute concentration value are given in Figure 3.20 and Figure 3.21, respectively. Although a slight decrease was observed at low concentration values at an index value, the refractive index values at both 980 and 1550 nm increased as the erbium concentration increased. The reason for this was that the refractive index value of Er_2O_3 was higher than the refractive index of Al_2O_3. It is quite natural that the resulting structure was between these two refractive indices. Furthermore, the Al/O ratio decreased with the increasing erbium concentration.

Table 3.9. *Calculated absolute erbium concentration*

	Al_2O_3: Er_2O_3			
	1:1	**5:1**	**1:5**	**5:5**
Absolute Er Conc. (cm^{-3})	$23,5x10^{19}$	$18,9x10^{19}$	$20,6x10^{20}$	$10,6x10^{20}$

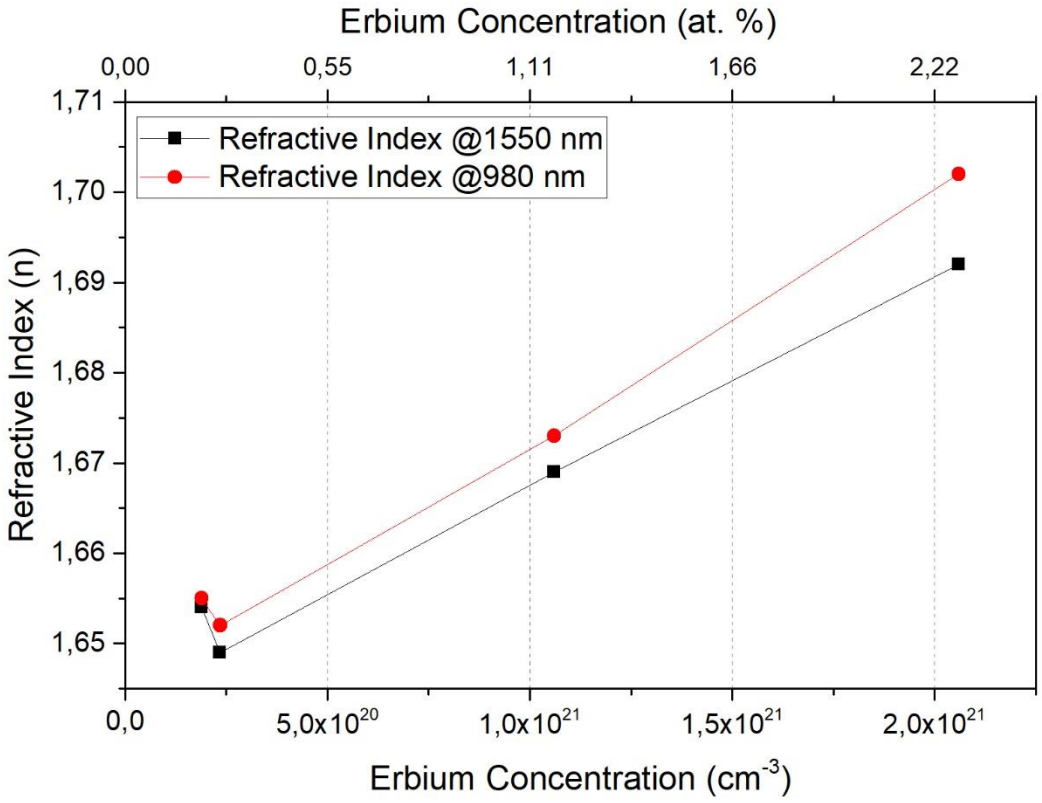

Figure 3.20. *Change of refractive index values at λ=980 and 1550 nm with an absolute concentration of erbium*

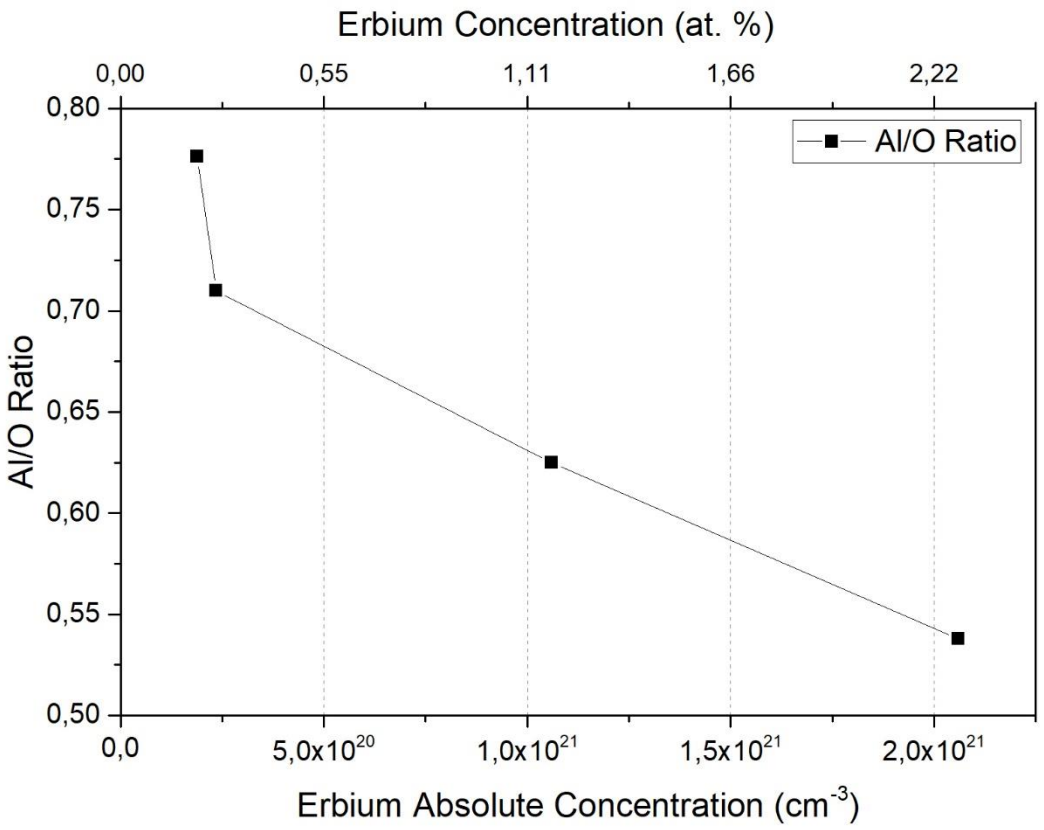

Figure 3.21. *Al/O ratio versus Erbium absolute concentration change*

3.4. Erbium Doped Ridge Waveguide Amplifier

3.4.1. Structuring of ridge waveguide

After fabrication of the passive waveguide device was carried out, experiments were conducted to fabricate an active waveguide device. A 1-μm-thick 5:5 Al_2O_3:Er_2O_3 sample was used. The lithography parameters used for the passive device were also used. After a few etching experiments, the result was that the active and passive structures had different etching ratios. The photoresist had risen earlier due to the higher etching rate in the horizontal plane of the active structure. The effect of photoresist removal caused it to be fabricated in triangles.

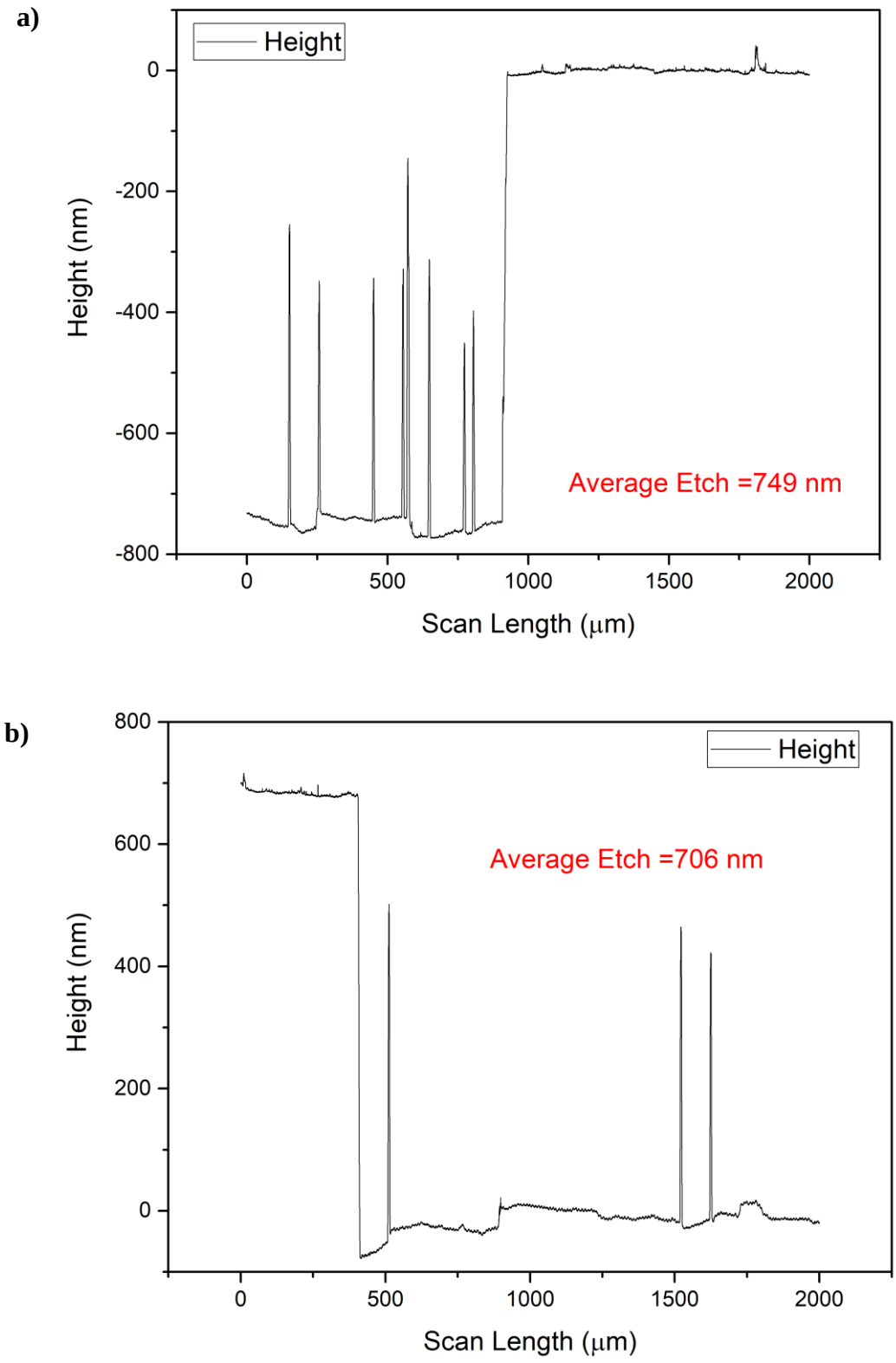

Figure 3.22. *Controlled etching result of the active structure using profilometer. a) and b) measurements were taken at different locations*

A controlled etching was performed, and the thickness of the etching was measured with a profilometer. The profilometer measurements are given in Figure 3.22. Figures

3.22a and b show the measurements taken from different locations of the same sample. The mean etch depth was found to be ~727 nm during the 14-minute period. The etch rate was calculated as 52 nm/min. It was seen that the active structure's etch rate was faster than that of the passive one. It was deduced that, with the same etching duration, the result was the removal of the active structure under the photoresist, and hence photoresist removal. The obtained triangular structure was optically modeled, and it was seen that it supported only the fundamental mode for λ=1550 and 1480 nm. The cross-sectional view of the fabricated device, the optical model and the supported fundamental mode cross-section at λ=1550 nm are given in Figures 3.23a, b, and c, respectively.

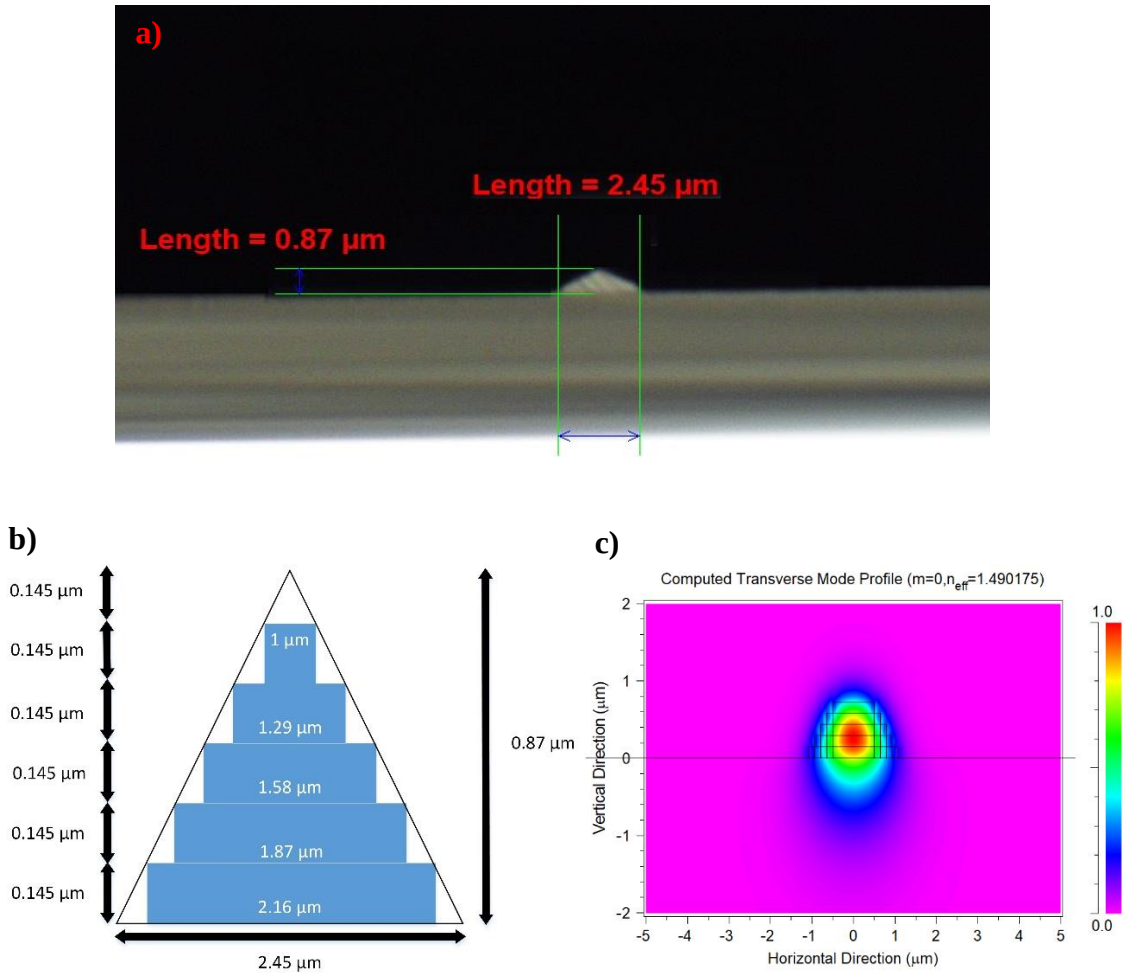

Figure 3.23. *Fabricated active waveguide and optical modeling a) Cross-sectional view of the fabricated waveguide b) Schematic of the active waveguide modeling c) Fundamental mode at λ = 1.55 µm.*

Lithography experiments were performed by using the active structure with a 5:5 cycle ratio with the help of the etch rate information obtained from this sample. The key

objective of these experiments was to save the structure from the triangular shape and increase the effective index value by increasing the confinement factor. For this purpose, the $Si/SiO_2/Al_2O_3:Er_2O_3$ active structure was cleaved systematically. The lithography parameters in these experiments were the same. The only difference was made in the chemical etching time. Different etching times of 5 and 7.5 minutes were applied, and the effects on the structures were examined. Additionally, optical cleaving processes were performed with the photoresist after etching these structures, and cross-section images were taken. The purpose of this process was to obtain the image of the aforementioned isotropic coupling process. Considering the measurements of the prism coupler, the thickness of these two samples taken from the center was expected to be ~0.71 µm. This value was verified from the optical images. The cross-sectional images of the ridge waveguides obtained as a result of 5 and 7.5 minutes of etching are shown in Figure 3.24.

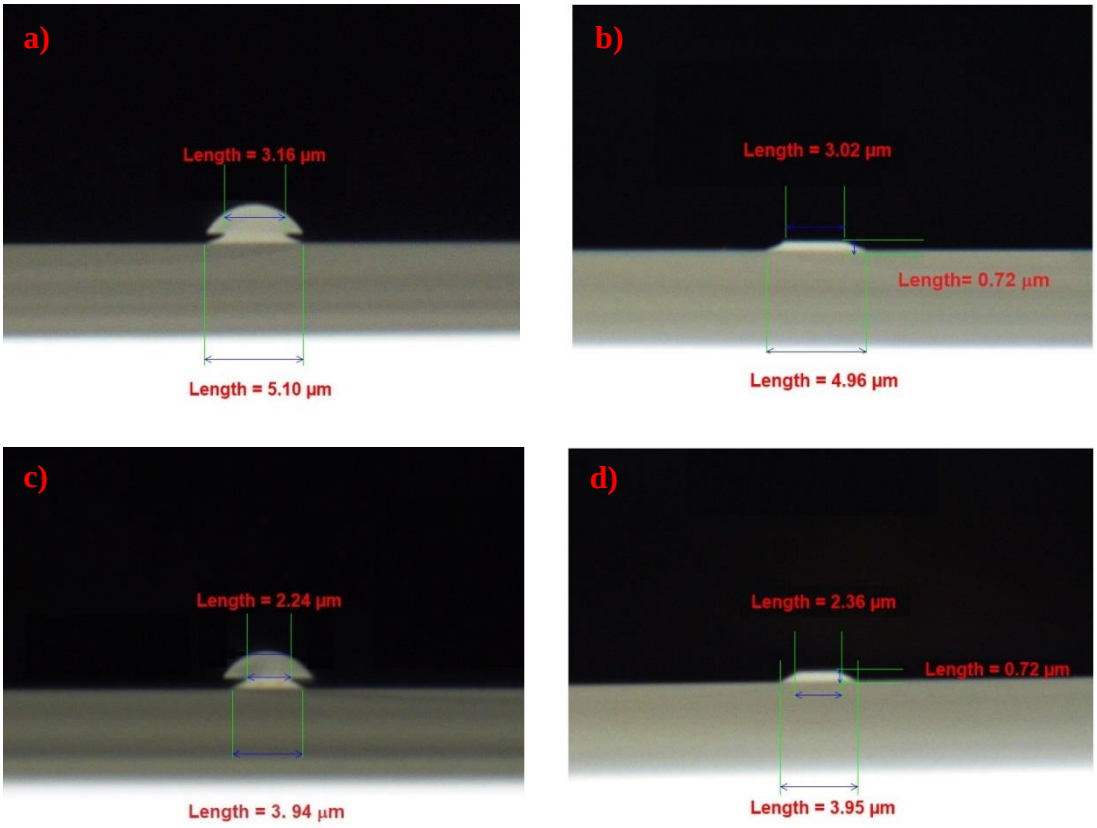

Figure 3.24. *The cross-sections of the device fabricated by photolithography of active structures with the growth of 5:5. a) After 5 minutes of etching b) After photoresist removal of "a" c) After 7.5 minutes of etching d) After photoresist removal of "c"*

In Figure 3.24, the peak widths of 5 and 7.5 minutes were measured. The top peak widths were measured as 3.16 and 2.24 µm, and the bottom peak widths were measured

as 5.10 and 3.94 μm, respectively. The top and bottom peak widths decreased as the chemical etching time increased. When the different device geometries on the device were examined, the peak widths differ by ±0.10 μm. When optical modeling was performed for these device geometries, it was seen that the device that was paired for 5 minutes supported multi-mode, and the device paired for 7.5 minutes supported single mode. These results were the same for both the TE and TM polarizations in terms of mode counts. When the results were compared to the triangular waveguide's previously given values, the effective index value was increased by 26.8%, and the value of 1.532 was achieved. According to these results, the most suitable geometry for the device was obtained with 7.5 minutes of etching. Thus, the device fabrication optimization processes were completed.

3.4.2. Time-resolved photoluminescence measurement

Lifetime measurements were made with the help of the time-resolved photoluminescence (TRPL) setup of the ridge waveguide amplifier device fabricated with the 5:5 cycle ratio. Then, the measurement setup was revised, and the optical gain was measured. The fabricated waveguide devices were characterized by optical properties at room temperature using two different experimental measurement setups. In the first measurement setup, the amplifier device for emitting erbium ions to emit ~1550 nm was excited with a 980 nm laser. The diagram of the TRPL measurement setup is given in Figure 3.25.

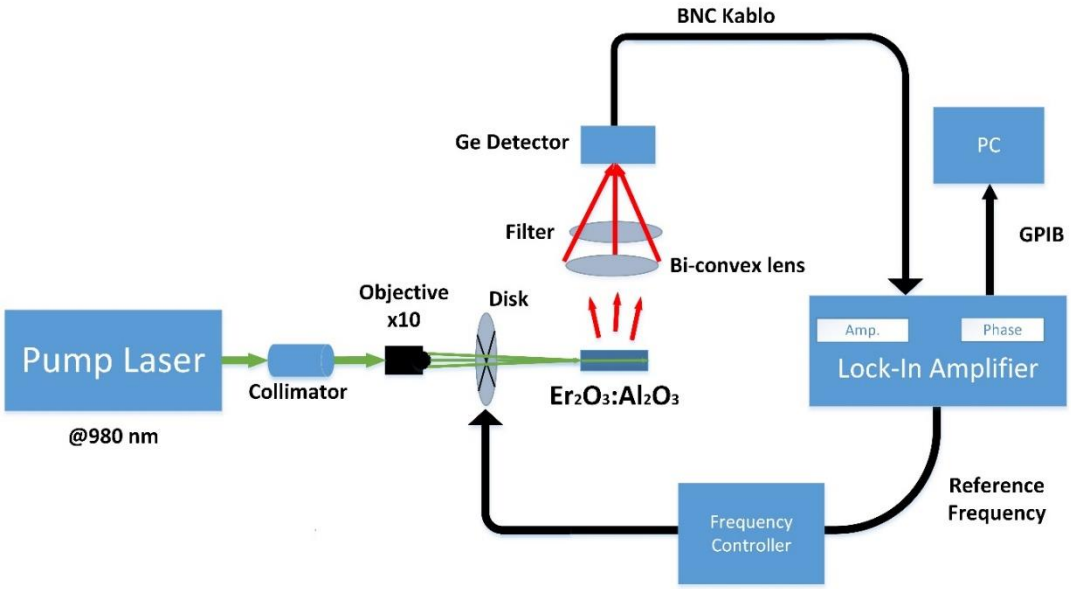

Figure 3.25. *Schematic of TRPL measurement setup*

The 980 nm diode laser, which can be modulated by temperature and current information, was used as the pump laser source. Since 980 nm was not visible, a 685 nm laser was used for alignment. A multi-mode FC/PC fiber with a range of 400-2000 nm was used to prevent alignment. The fiber was connected to the collimator and never removed. For alignment, a 685 nm laser was used first, and the 980 nm laser that was connected in the input after the mode guide was complemented. Measurements were taken assuming that the alignment did not shift. The laser beam emitted from the collimator passed through the rotating disk according to the reference frequency information from the Lock-in amplifier. This disk worked like a chopper by turning on and off the laser of the desired frequency to create an AC signal. The frequency information could be changed via the Lock-in amplifier. The light passing through the disc focused at a distance of ~15-20 mm using the x10 objective lens. The reason for using the x10 objective lens was to enable the 980 nm laser to be modulated as far as possible. Thanks to the focal length, the modulation disk could be inserted after the x10 objective lens. The device was placed where the laser is fully focused with the aid of XYZ stages. The optically cleaved edge of the device ensured that the light was inserted into the device more accurately without loss of reflection. In this case, the desired waveguide was properly excited using the top microscope. 1550 nm photons were emitted while the 980 nm laser was guiding the waveguide in. These photons focused on the active part of the Ge-detector at a distance of ~ 25.4 mm from the filter after the bi-convex lens, which

was placed at 1-2 mm above the device and compactly prepared to minimize loss. The Bias feature Ge detector generated current when a signal was received and the current was transmitted to the Lock-in amplifier using a BNC cable. In the current mode of the lock-in amplifier, phase-sensitive sensing was performed by applying some DSP operations between the modulated signal from the detector and the signal previously transmitted to the modulation disk. Because this signal was quite low, it was necessary to use a lock-in amplifier for increasing SNR. The pictures of the TRPL setup from different perspectives are shown in Figures 3.26, 3.27 and 3.28. Figure 3.26 shows the side of the excitation (front). Figure 3.27 shows the side with the amplifier device (rear). Figure 3.28 shows the setup from above. Some spacing in the modulating disc was covered with aluminum foil. This was because the duty cycle could be reduced to accurately measure the lifetime which was in the range of milliseconds. If it was not kept off position enough, the exponential decreasing function would not be able to take a correct measurement by going back to the on position without completing its period. Therefore the duty-cycle was set to 25%. Thus, one-on, three-off position measurements were taken in a period.

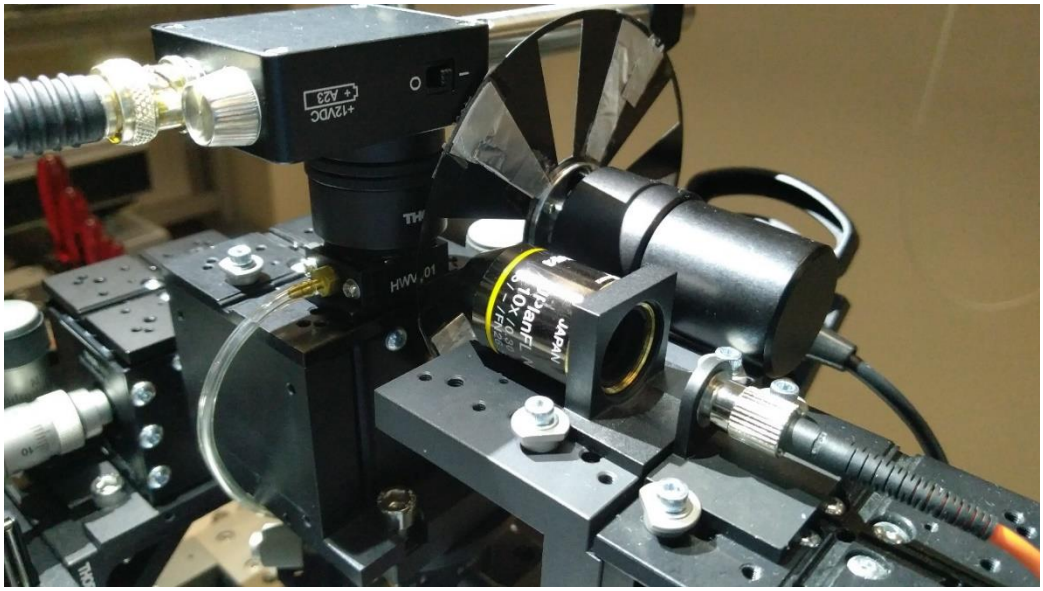

Figure 3.26. *TRPL measurement setup (front)*

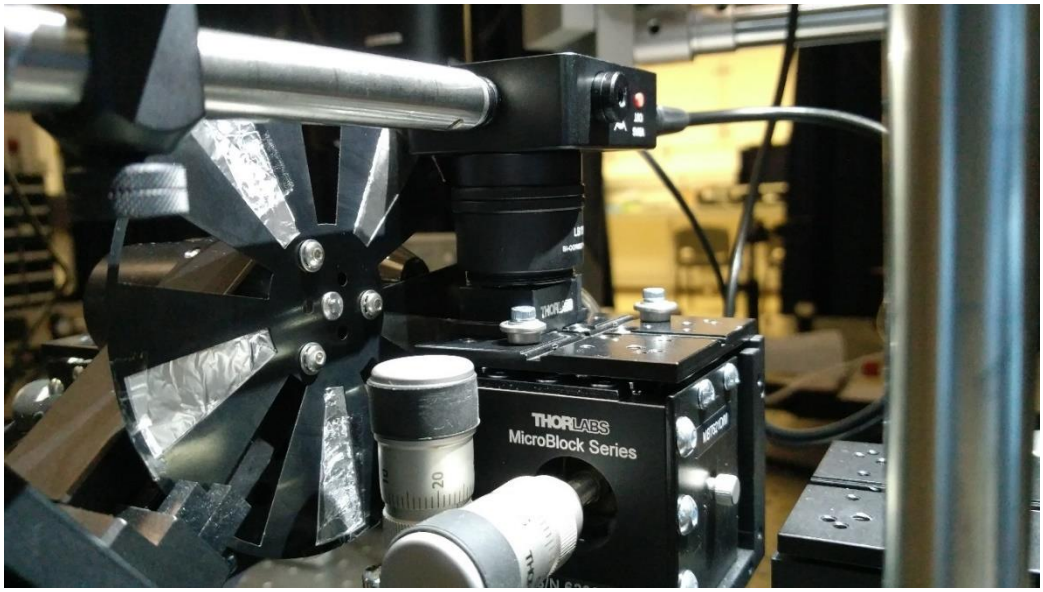

Figure 3.27. *TRPL measurement setup (rear)*

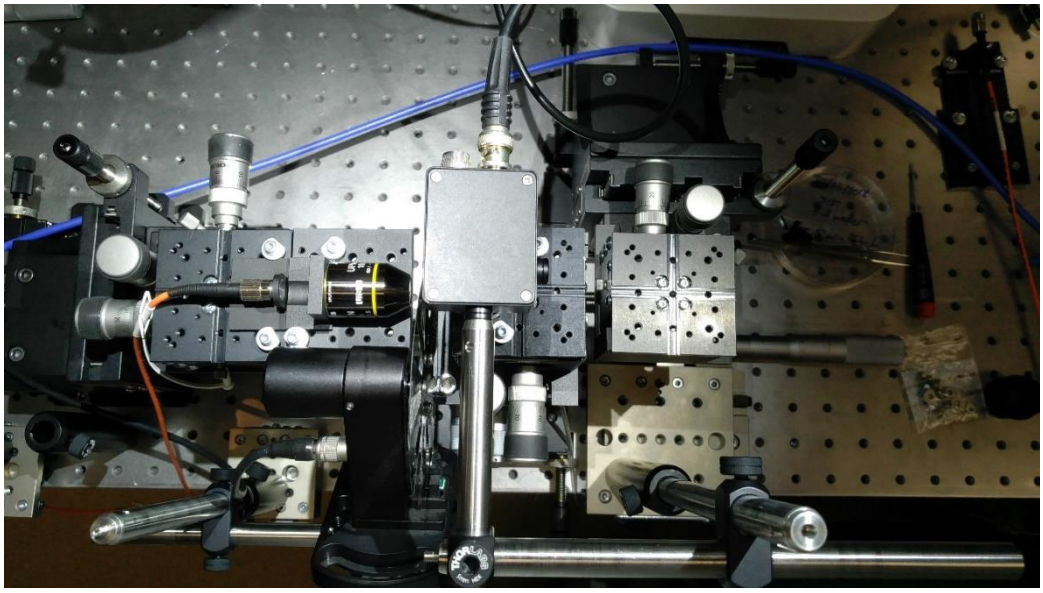

Figure 3.28. *TRPL measurement setup (top)*

When the lock-in amplifier detected the signal, it calculated the phase angle between constant amplitude and the signal between the reference signal and the detected signal. The phase angle is the value we used for the lifetime measurement of the emission. The constraint in the technique we used is the necessity of a single exponential function. That is, a single radiation signal must be present. If there is a single signal at a given frequency, the exponential reduction time, i.e. the lifetime, is calculated as follows.

$$\tau = \frac{\tan \theta_{\omega}}{\omega}, \qquad \omega = 2\pi f_{modulasyon} \tag{3.2}$$

In Equation 3.2; τ gives the lifetime, θ_ω represents the phase angle between the signals measured by the reference signal (i.e. the detected emission signal), and ω shows the circular modulation frequency. Derivation of the equation is given as follows. It is assumed that the excitation signal is light with sinusoidal modulation as follows,

$$L(t) = a + b \sin \omega t \tag{3.3}$$

Fluorescent emission is forced to respond at the same frequency (using a modulation disc), but phase and modulation will be different. We can assume that the excited state population is as follows,

$$N(t) = A + B \sin(\omega t - \theta) \tag{3.4}$$

Equation 3.5 also determines the relationship between lifetime and phase shift. Assume that the reduction in intensity following the δ- function trigger is a single exponential function,

$$I(t) = I_0 e^{(-t/\tau)} \tag{3.5}$$

Differential equation describing time-dependent intensity for a single exponential reduction function,

$$\frac{dI(t)}{dt} = -\frac{1}{\tau} I(t) + L(t) \tag{3.6}$$

Substituting Equation 3.4 in Equation 3.6,

$$\omega B \cos(\omega t - \theta) = -\frac{1}{\tau}[A + B \sin(\omega t - \theta)] + a + b \sin \omega t \tag{3.7}$$

This equation should always hold. The relationship between A, B, a and b values and τ may be achieved by expanding the sine and cosine functions. This ensures that the following equations are achieved.

$$a - (1/\tau)A = 0 \tag{3.8}$$

$$\omega \cos \theta - (1/\tau) \sin \theta = 0 \tag{3.9}$$

$$\omega \sin \theta + (1/\tau) \cos \theta = b/B \tag{3.10}$$

After Equation 3.9 is revised, the relationship between lifetime and phase angle is obtained.

$$\frac{\sin\theta}{\cos\theta} = \tan\theta = \omega\tau \qquad (3.11)$$

Lifetime calculations were made by using Equation 3.11. In order to be consistent, the phase angle must be changed as the modulation frequency changes. It may be mentioned that there is an exponential glow if this change is observed and the result is the same. In order to increase the measurement accuracy, life cycles were calculated by using different modulation frequencies. The lock-in amplifier showed the phase difference at a certain interval after it detected the signal. The error margin of the measurements was also calculated using this range. Phase angle and lifetime measurements according to different modulation frequencies are given in Table 3.10. The linear fit of these values is given in Figure 3.29. The lifetime was calculated as 4.38±0.31 ms. It was related to the rate of erbium in the device. Longer lifetime was an indication that the device could radiate at longer distances. This will be explained by the optical gain measurements.

Table 3.10. *Lifetime results according to different modulations*

Modulation Freq. (Hz)	**Phase Angle (θ)**	τ_{min}	τ_{max}	τ
19	27,5-28,5	4,36	4,55	4,45 ± 0,13
23	32,5-33,4	4,41	4,56	4,49 ± 0,11
25	33-34,5	4,13	4,38	4,25 ± 0,17
27	35,3-36,3	4,17	4,36	4,27 ± 0,13
33	42,5-43,5	4,42	4,58	4,49 ± 0,11

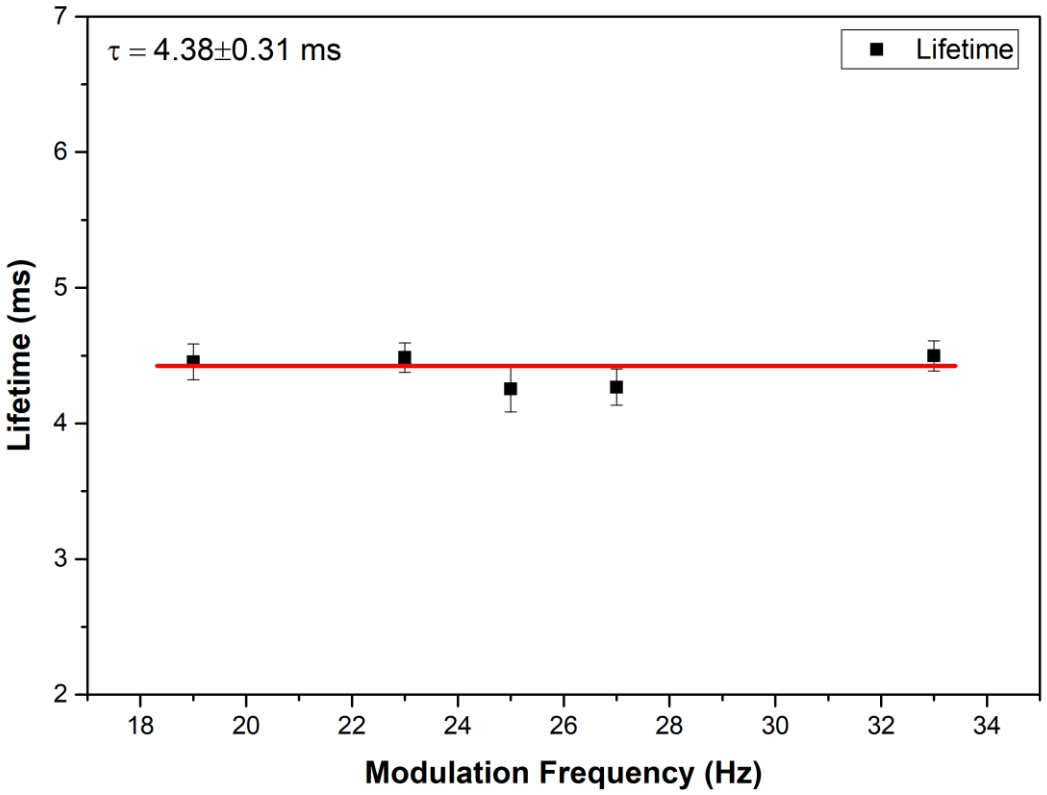

Figure 3.29. *A linear fit of the lifetime using different modulation frequencies.*

3.4.3. Optical gain measurement

After calculating the lifetime at 1550 nm, the effects of it on performance enhancement of the device were measured. By means of performance enhancement, a waveform device operating at a specific wavelength was coupled with the same optical path of operation wavelength into a second wavelength laser which we refer to as a pump, resulting in an optical gain. It was possible to measure this gain, unlike the TRPL setup, the operation and pump laser require simultaneous use. The schematic of the gain measurement setup is given in Figure 3.30.

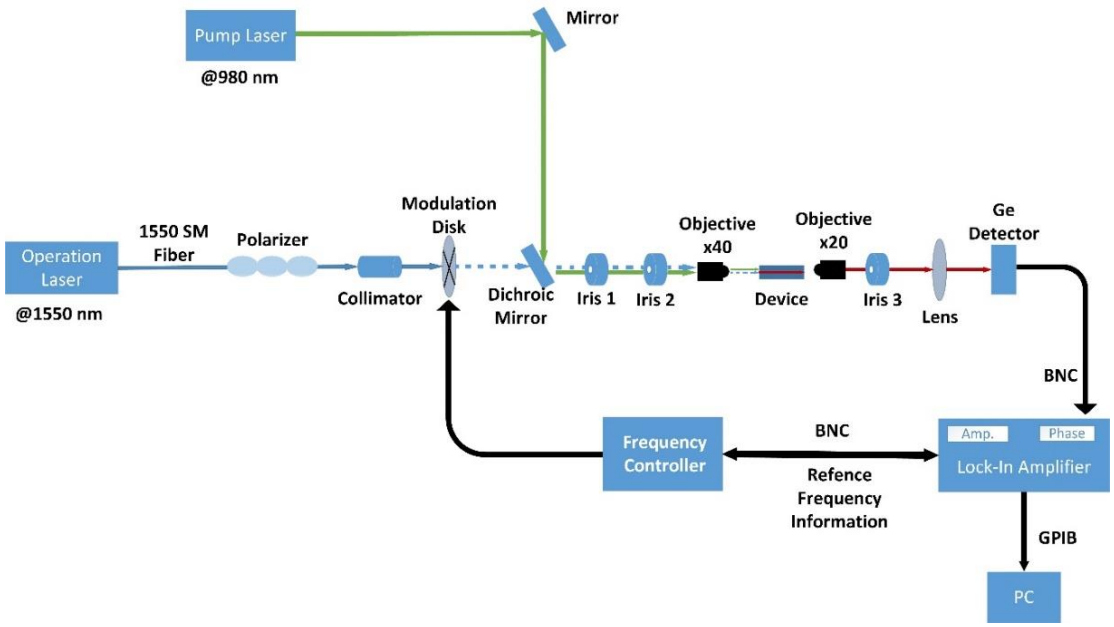

Figure 3.30. *Scheme of the optical gain measurement setup*

The dichroic mirror was used to bring the two different laser wavelengths to the same optical path. The characteristic of this mirror is that it reflects another wavelength laser in that range while transmitting up to a certain wavelength. Thanks to this mirror, the 1550 nm operation laser would be transmitted, but the 980 nm pump laser would be reflected. The 1550 nm operation laser was taken from the diode laser which could be adjusted with temperature. This source with the FC/PC output was equipped with fiber supporting single-mode at 1550 nm. The polarizer was used so that the mode could be set to TE or TM. This wavelength-compatible collimator was connected to the outlet of the fiber. At the exit of the collimator, the 1550 nm laser, which traveled in the air, first passed through the dichroic mirror after the modulation disk, then through the iris 1 and 2, respectively, to reach the x40 objective lens. Here only the operation laser was modulated. The main reason for this was to ensure a continuous gain without disrupting the pump laser. The pump laser could be modulated but not investigated. Unlike the TRPL setup, the pump laser was not taken from the diode laser but from the NKT white light source that provided more power. The pump laser reached the x40 objective lens after passing through 2 reflective mirrors, 1 dichroic mirror, and 2 irises, in this order, passing through the air path. The use of 2 irises was performed to align two different lasers. Simply mathematical properties were used where one linear line could be created by using 2 points somewhere in the space. The iris aperture was set to the minimum. Two such optical paths were reduced to a single optical path. This process can be achieved using a

pinhole. The most difficult part of the gain setup is to excite the waveguide device. Since the two lasers that were used were near-infrared, they could not be seen. For solving this problem, a single-mode 685 nm laser was connected via FC/PC fiber to the collimator. Actually, considering the collimator that was compatible with the 1550 nm laser, the reasonable loss was accepted for alignment. The point to be taken into account was the multiple reflections of the 685 nm laser as it passed through the dichroic mirror that was compatible with 980/1550 nm. Alignment should be done according to first order mode, and it fails otherwise. In fact, the 1550 nm laser faced a similar situation, but higher order modes were much weaker than the first order mode. After the waveguide was excited, the mode output was detected by means of the x20 objective lens placed on the output side of the waveguide. The duty of the x20 objective lens was to distinguish only the mode output by taking the signal from a certain depth of focus and distinguishing it from other signals. The x20 objective lens was placed on the XYZ stages so that the mode output could easily be directed to the desired location. Even if we could direct the mode to our request, the guided mode came with some reflected lasers that could not be coupled to the waveguide. Iris 3 was used to distinguish these. It actually only allowed the excited mode to pass. Whether or not the 1550 nm laser would be coupled to the device was determined by using the power meter attached to the iris 3 outlet. After the alignment of 1550 nm, an alignment of 980 nm was performed. While using the 685 nm laser, the 980 nm laser was sent at the same time, and the alignment was carried out using the detector card. Similarly, the power was switched on and off with the help of the power meter placed after iris 3, the change in power was observed, and the mode was determined. After coupling loss reduction and alignment were completed, the 685 nm laser was removed and the 1550 nm laser was connected. Thus, alignment and coupling loss reduction experiments were completed. The optical mode was focused on the active part of the Ge-detector using the 1550 nm compatible lens after all the wavelengths of alignment and coupling loss reduction were completed. This lens allowed focusing the lasers in the range of 1100-1550 nm and attenuated other lasers by reflecting. Pictures of the gain measurement setup from different perspectives are given in Figures 3.31, 3.32 and 3.33.

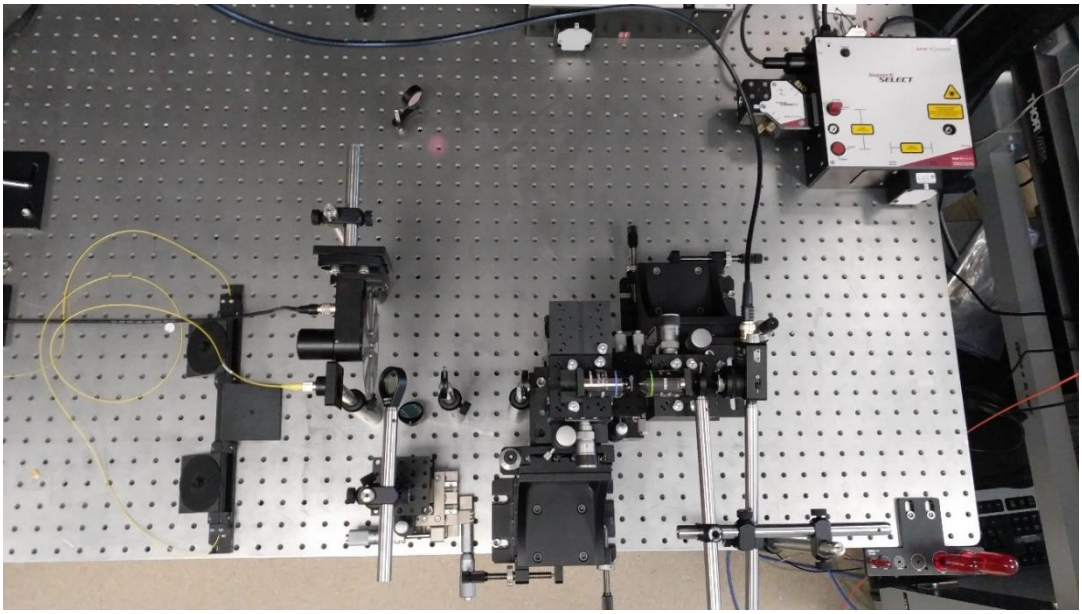

Figure 3.31. *Optical gain measurement setup 1*

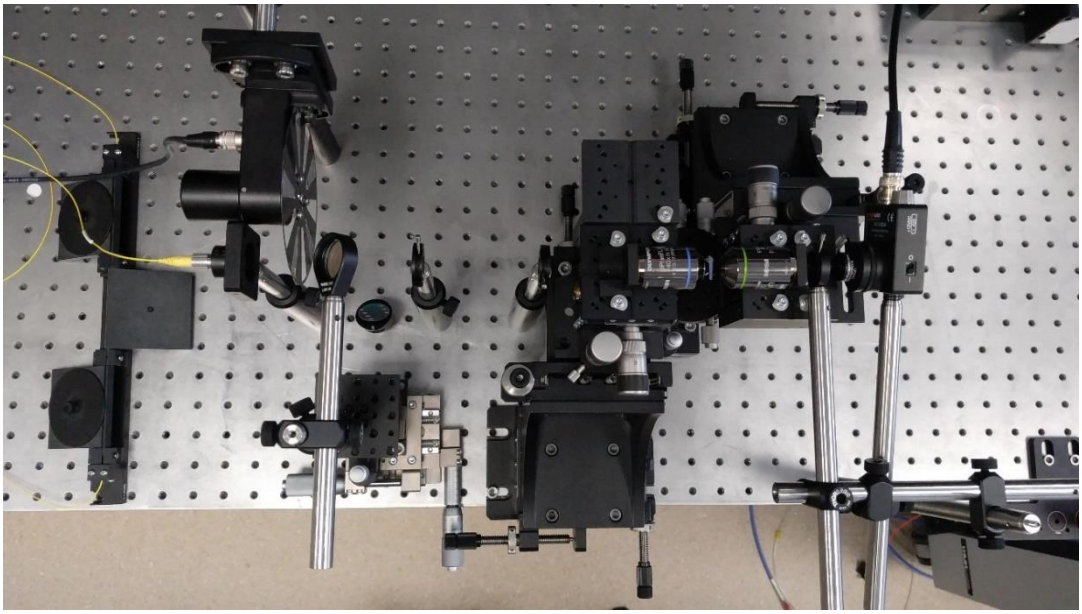

Figure 3.32. Optical gain measurement setup 2

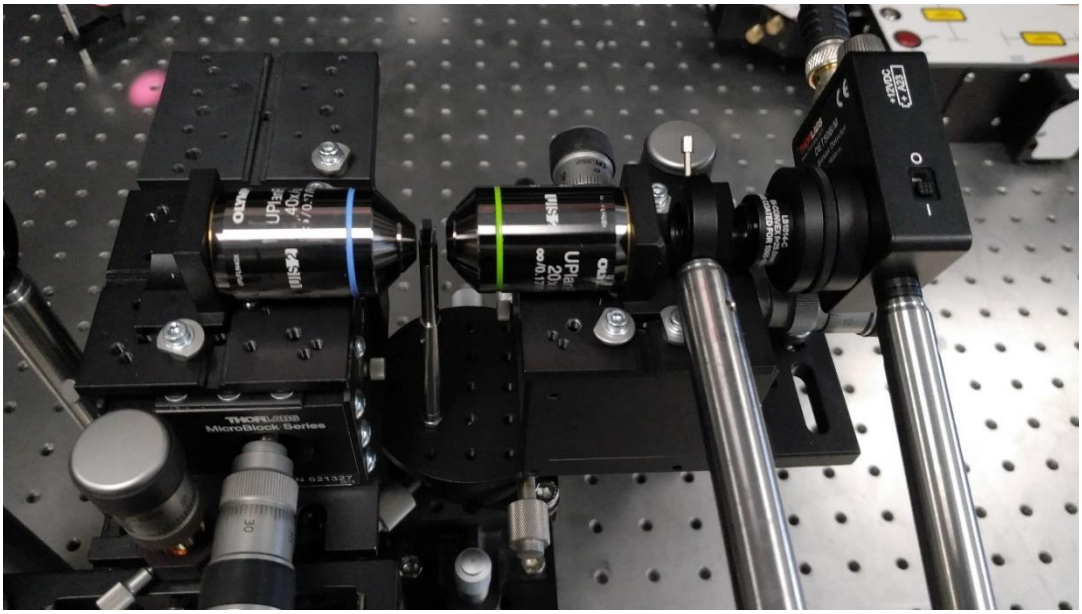

Figure 3.33. *Optical gain measurement setup 3*

The signal collected with the germanium detector was detected and amplified by the phase-sensitive detection technique using the lock-in amplifier. The internal net optical gain was calculated as follows by subtracting the propagation and absorption losses from the small signal gain coefficient at dB/cm.

$$Optical\ Gain\ (\lambda) = 10\left[\frac{\log_{10}\left(I_{on}/I_{off}\right)}{L}\right] - \alpha(\lambda) \qquad (3.12)$$

In Equation 3.12, I_{on} is the measured maximum amplitude when the pump signal is on, I_{off} when off, L is the active device length in cm and $\alpha(\lambda)$ is the wavelength-dependent propagation and absorption loss. According to studies in the literature, the propagation loss of a planar and the ridge waveguide device is approximately the same [27]. Based on this information, the propagation loss at 1550 nm of the planar active device was required. Previously, measurements of the passive device were made using a prism coupler for a similar active device. At 1550 nm, the optical mode was first found and the scattered light was measured using a fiber detector which was able to move along the propagation to measure the optical loss in dB/cm. The loss measurement of the active device is given in Figure 3.34. The average of the measurements from five different points was found to be 0.60 dB/cm. This loss value would be used in internal net gain calculations.

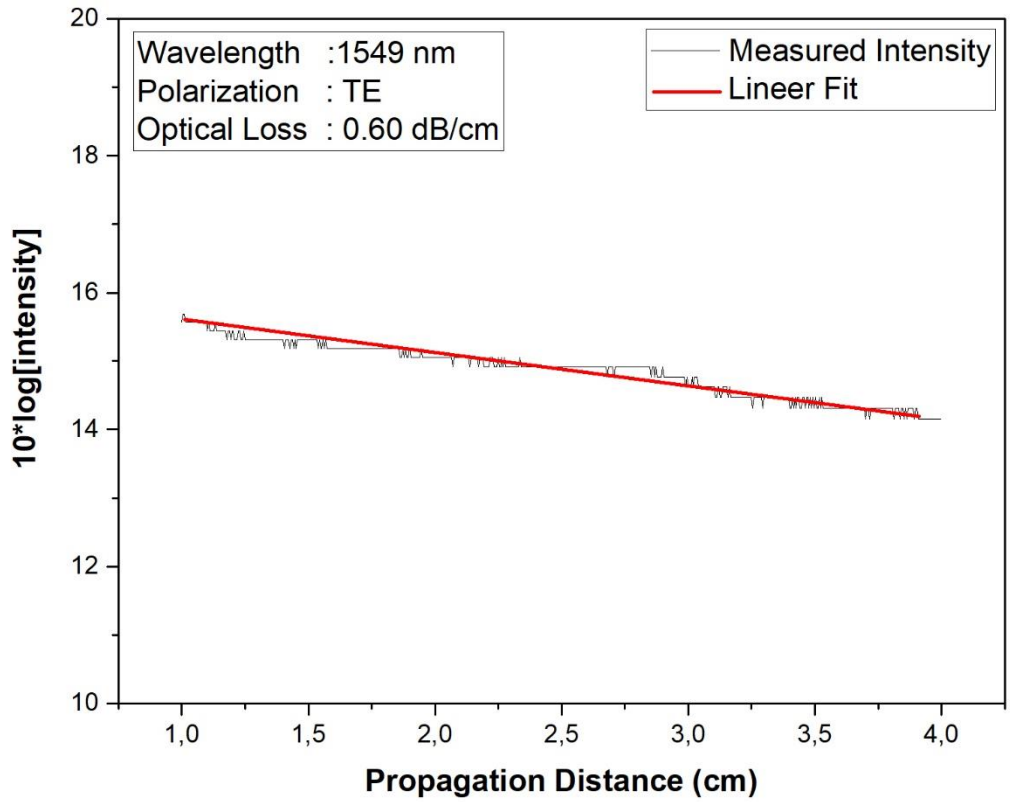

Figure 3.34. *Propagation loss measurement of the active device at λ=1550 nm*

The critical point to be taken into account in the gain calculation is the power of the operation signal. If we use high power (mW band), small amounts of gain cannot be determined by the Lock-in technique. Due to this limitation, the power of the 1550 nm laser at the focal point of the lens was set to 2 μW while modulating. The modulation frequency was 287 Hz. The maximum output power of the pump signal was 30 mW. Devices with two different lengths used for the gain measurements. Internal net gains were calculated for the different pump power values of these devices. Table 3.11 shows the measurement of the gain of the active device at different lengths and pump powers. The representation of the values given in the table is shown in Figure 3.35.

Table 3.11. *Gain measurements of 2- and 4-mm length devices at different pump powers*

Length of Device (mm)	Incoming Power (%)	Incoming Power (mW)	Input Power (mW)	Pump On/Off Rate	Internal Net Gain (dB/cm)
2	20	13,1	0,17	1,53	8,68
	40	16,9	0,22	1,64	10,09
	60	23,1	0,30	1,93	13,72
	80	27,7	0,36	1,92	13,57
	100	30	0,39	1,74	11,44
4	20	13,1	0,17	1,04	-0,21
	40	16,9	0,22	1,07	0,12
	60	23,1	0,30	1,12	0,65
	80	27,7	0,36	1,13	0,66
	100	30	0,39	1,19	1,32

Optical gain decreases as the device length increases. Gain values on a 2-mm device were measured in the range of 8.68-13.72 dB/cm. At 4 mm of length, it was (-0.21)-1.32 dB/cm. The highest gain was measured at 13.72 dB/cm with a pump power of 23 mW on the 2-mm device. In the 2-mm device, the gain with the pump power tended to decrease after increasing for a while. In the 4-mm device, there was a linear relationship. When the length was doubled, the gain value decreased considerably. The reason for this was that the 980 nm laser was absorbed very quickly, and it emitted at 1550 nm. Another reason was that the optical cleavage process could not be achieved properly, and it caused more reflection. This is because it is very important that the laser couples via a smooth surface and exits from a smooth surface. This is just a possibility. This is not the case if the input and output levels of the samples are considered ideal. In order to obtain gain values in longer samples, pump power should be increased.

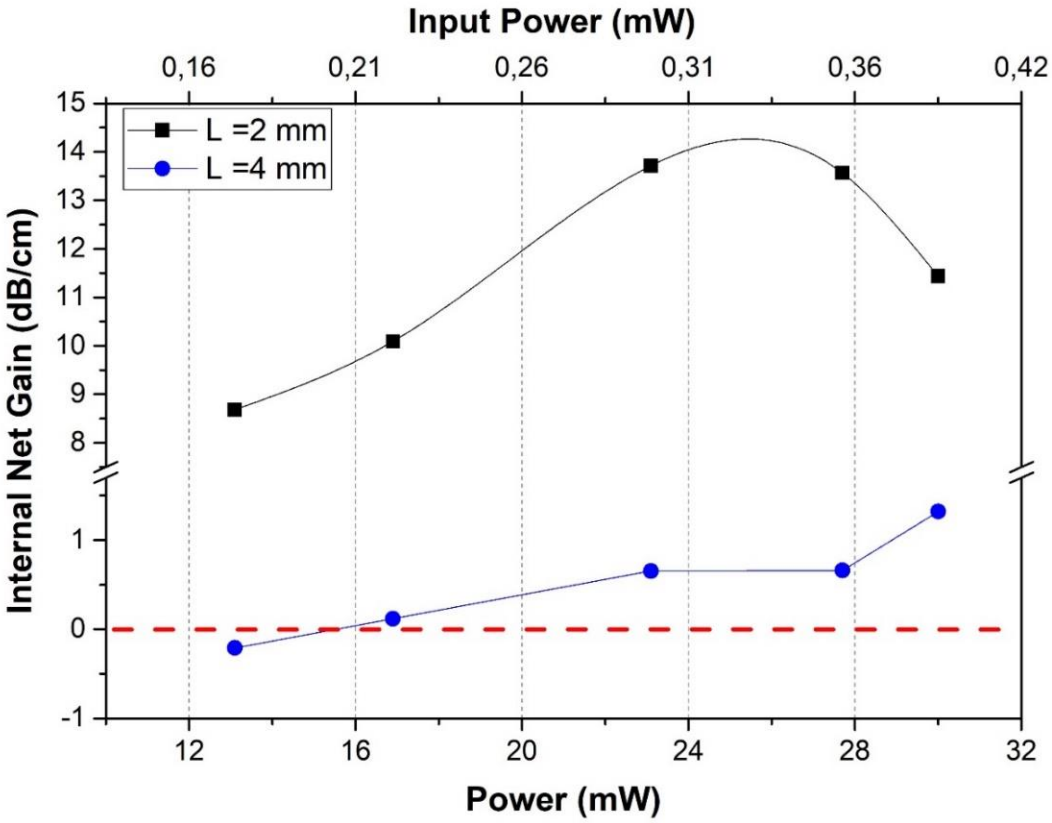

Figure 3.35. *Internal net gain measurement*

4. CONCLUSION

In this thesis, ALD deposited chip-scale single-mode Er^{3+} doped Al_2O_3 ridge waveguide amplifiers with small-signal gains of more than 13 dB/cm over the C-band have been reported. The reported high gain was possible due to optimization of the ALD grown doping of the waveguide layers. Several specific aims, including developing reliable and high-quality fabrication methods and demonstrating higher gain in Er^{3+} doped Al_2O_3 have been achieved.

As the first part of this work, undoped waveguide was demonstrated. An integrated optical planar waveguide was realized using Al_2O_3 layers over a large substrate. Thermal Atomic Layer Deposition is used to deposit Al_2O_3 layers. The device propagation losses were measured for both TE and TM polarization at visible and near-infrared wavelengths. For the C-band operation, the lowest reported propagation loss value of 0.04±0.02 dB/cm for the Al_2O_3 planar waveguides was reported. This part of the thesis will give direction to future research on improving the performance of low background loss required applications. Fabrication of ridge waveguide that supports single-mode was also performed.

A new fabrication method for depositing Er^{3+} doped Al_2O_3 thin films by Plasma Enhanced Atomic Layer Deposition was developed. Investigations showed that the resulting thin films have high thickness uniformity, tunable refractive indices could be deposited. The deposition could be performed on thermally oxidized silicon wafers or Si substrates. The Er_2O_3 layers were grown between the Al_2O_3 layers to achieve erbium ion doping with the homogenous distribution. By adjusting the cycle ratio Er concentration in the Al_2O_3 host material could be adjusted. The effects of the growth parameters of Al_2O_3 and Er_2O_3 including deposition temperature, RF plasma power, TMA pulse time, $Er(thd)_3$ pulse time and O_2 pulse time were optimized.

Based on the results reported in this thesis, Er^{3+} doped Al_2O_3 can be considered as a competitive active medium for integrated optics. The reliable deposition and structuring methods and high gain allow for the design and realization of many new active devices and applications. The first steps in terms of devices and applications have been demonstrated in this work.

5. REFERENCES

[1] Hunsperger, R. G. (1995). *Integrated optics*. Berlin, Heidelberg: Springer.

[2] Ready, J. F. (1997). *Industrial applications of lasers* 2nd ed. Elsevier Science.

[3] Pollock, C. R. and Lipson, M. (2003). *Integrated photonics*. USA: Springer.

[4] Xhoxhi, M. et al. (2015). Interferometric evanescent wave biosensor principles and parameters. *IOSR-JAP*, vol. 7, no. 6, pp. 84-96.

[5] Wartak, M. S. (2013). *Computational photonics: an introduction with MATLAB*. New York: Cambridge University Press.

[6] Zourob, M. et al. (2008). *Principles of bacterial detection: biosensors, recognition receptors and microsystems*. Springer Science & Business Media.

[7] Snyder, A. W. and Love, J. (2012). *Optical waveguide theory*. Springer Science & Business Media.

[8] Tippett, J. T. et al., "Optical and electro-optical information processing," Massachusetts Inst Of Tech Cambridge, 1965.

[9] Burns, W. et al. (1979). Ti diffusion in Ti: LiNbO3 planar and channel optical waveguides. *Journal of Applied Physics,* vol. 50, no. 10, pp. 6175-6182.

[10] Liu, J.-M. (2009). *Photonic devices*. Cambridge University Press.

[11] Agrawal, G. P. (2007). Optical Waveguides (OPT568). *Institute of Optics, University of Rochester*.

[12] Benaissa, K. and Nathan, A. (1998). Silicon anti-resonant reflecting optical waveguides for sensor applications. *Sensors and Actuators A: Physical,* vol. 65, no. 1, pp. 33-44.

[13] Prieto, F. et al. (2000). Design and analysis of silicon antiresonant reflecting optical waveguides for evanscent field sensor. *Journal of lightwave technology*, vol. 18, no. 7, p. 966.

[14] Brecht, A. and Gauglitz, G. (1995). Optical probes and transducers. *Biosensors and Bioelectronics,* vol. 10, no. 9-10, pp. 923-936.

[15] Salemink, H. et al. (1999). Silicon-oxynitride (SiON) for photonic integrated circuits. *MRS Online Proceedings Library Archive,* vol. 574.

[16] Chen, F. et al. (2007). Development of ion-implanted optical waveguides in optical materials: A review. *Optical materials,* vol. 29, no. 11, pp. 1523-1542.

[17] Davis, K. M. et al. (1996). Writing waveguides in glass with a femtosecond laser. *Optics letters,* vol. 21, no. 21, pp. 1729-1731.

[18] Parriaux, O. and Veldhuis, G. (1998). Normalized analysis for the sensitivity optimization of integrated optical evanescent-wave sensors. *Journal of lightwave technology*, vol. 16, no. 4, p. 573.

[19] Rönn, J. (2014). Fabrication and characterization of atomic-layer-deposited Er_2O_3 for optical amplifier devices. Ph.D. Thesis, School of Electrical Engineering, Aalto University, Espoo, Finland.

[20] Lipson, A. et al. (2010). *Optical physics*. Cambridge University Press.

[21] Svelto, O. and Hanna, D. C. (2010). *Principles of Lasers, Fifth Edition* (Principles of Lasers, Fifth Edition). New York: Springer (in English), pp. 1-620.

[22] Agrawal, G. P. (2010). *Fiber-optic communications systems Fourth Edition Introduction* (Fiber-Optic Communication Systems, 4th Edition). Chichester: John Wiley & Sons (in English), pp. 1-23.

[23] Kenyon, A. J. (2002). Recent developments in rare-earth doped materials for optoelectronics. *Progress in Quantum Electronics*, vol. 26, no. 4-5, pp. 225-284, doi: 10.1016/s0079-6727(02)00014-9.

[24] Pathmanathan, S. S. and Choudhury, P. K. (2010). Novel usage of erbium in optical communication systems–From fundamentals to performance characteristics, in *Erbium: Compounds, Production and Applications*: Nova Science Publishers, Inc., pp. 1-108.

[25] Trabelsi, I. et al. (2010). Crystal field analysis of Er^{3+} in Sc_2O_3 transparent ceramics. *Journal of Luminescence*, vol. 130, no. 6, pp. 927-931, doi: 10.1016/j.jlumin.2010.02.004.

[26] Mitschke, F. (2016). *Fiber optics*. Verlag Berlin Heidelberg: Springer.

[27] Bradley, J. D. B. (2009). Al_2O_3:Er^{3+} as a Gain Platform for Integrated Optics. Ph.D. Thesis, University of Twente.

[28] Zou, X. and Izumitani, T. (1993). Spectroscopic properties and mechanisms of excited state absorption and energy transfer upconversion for Er3+-doped glasses. *Journal of Non-Crystalline Solids*, vol. 162, no. 1-2, pp. 68-80.

[29] Kik, P. G. (2000). Energy transfer in erbium doped optical waveguides based on silicon.

[30] Keiser, G. (2003). Optical fiber communications. *Wiley Encyclopedia of Telecommunications*.

[31] Kim, H. S. et al. (1998). Actively gain-flattened erbium-doped fiber amplifier over 35 nm by using all-fiber acoustooptic tunable filters. *IEEE photonics technology letters,* vol. 10, no. 6, pp. 790-792.

[32] Wongpaibool, V. and Jacobs, I. (Year), Effect of dispersion on spectrum-sliced WDM systems, in *Conference Proceedings. LEOS'98. 11th Annual Meeting. IEEE Lasers and Electro-Optics Society 1998 Annual Meeting (Cat. No. 98CH36243)*, 1998 1998, vol. 1: IEEE, 1998, pp. 374-375.

[33] Kenyon, A. J. et al. (1994). Optical properties of PECVD erbium-doped silicon-rich silica: evidence for energy transfer between silicon microclusters and erbium ions. *Journal of Physics-Condensed Matter,* vol. 6, no. 21, pp. L319-L324, doi: 10.1088/0953-8984/6/21/007.

[34] Chryssou, C. E. and Pitt, C. W. (1998). Er^{3+}-doped Al_2O_3 thin films by plasma-enhanced chemical vapor deposition (PECVD) exhibiting a 55-nm optical bandwidth. *IEEE Journal of Quantum Electronics,* vol. 34, no. 2, pp. 282-285, doi: 10.1109/3.658711.

[35] Hubner, J. et al. (2001). Planar Er- and Yb-doped amplifiers and lasers. *Applied Physics B-Lasers and Optics,* vol. 73, no. 5-6, pp. 435-438.

[36] Mahnke, M. et al. (2001). Aluminum oxide doped with erbium, titanium and chromium for active integrated optical applications. *Aeu-International Journal of Electronics and Communications,* vol. 55, no. 5, pp. 342-348, doi: 10.1078/1434-8411-00051.

[37] Shuto, K. et al. (1993). Erbium-doped phosphosilicate glass waveguide amplifier fabricated by PECVD. *Electronics Letters,* vol. 29, no. 2, pp. 139-141, doi: 10.1049/el:19930094.

[38] Han, H. S. et al. (2002). Coefficient determination related to optical gain in erbium-doped silicon-rich silicon oxide waveguide amplifier. *Applied Physics Letters,* vol. 81, no. 20, pp. 3720-3722, doi: 10.1063/1.1520710.

[39] Multone, X. et al. (2008). Er-doped Al_2O_3 thin films deposited by high-vacuum chemical vapor deposition (HV-CVD). *Materials Science and Engineering B-Solid State Materials for Advanced Technology,* vol. 146, no. 1-3, pp. 35-40, doi: 10.1016/j.mseb.2007.07.086.

[40] Vasilief, I. et al. (2005). Propagation losses and gain measurements in erbium-doped fluoride glass channel waveguides by use of a double-pass technique. *Applied Optics,* vol. 44, no. 22, pp. 4678-4683, doi: 10.1364/ao.44.004678.

[41] Roberts, S. W. et al. (1996). The photoluminescence of erbium-doped silicon monoxide. *Optical Materials,* vol. 6, no. 1-2, pp. 99-102, doi: 10.1016/0925-3467(96)00013-4.

[42] Strohhofer, C. et al. (1998). Active optical properties of erbium-doped GeO_2-based sol-gel planar waveguides. *Thin Solid Films,* vol. 326, no. 1-2, pp. 99-105, doi: 10.1016/s0040-6090(98)00535-5.

[43] Dong, B. et al. (2007). Optical high temperature sensor based on green up-conversion emissions in Er^{3+} doped Al_2O_3. *Sensors and Actuators B-Chemical,* vol. 123, no. 2, pp. 667-670, doi: 10.1016/j.snb.2006.10.002.

[44] Almeida, R. M. et al. (1999). Er^{3+}-doped multicomponent silicate glass planar waveguides prepared by sol-gel processing. *Journal of Sol-Gel Science and Technology,* vol. 14, no. 2, pp. 209-216, doi: 10.1023/a:1008794202103.

[45] Yeatman, E. M. et al. (1999). Optical gain in Er-doped SiO_2-TiO_2 waveguides fabricated by the sol-gel technique. *Optics Communications,* vol. 164, no. 1-3, pp. 19-25, doi: 10.1016/s0030-4018(99)00171-6.

[46] Laliotis, A. and Yeatman, E. M. (2007). Multilayered waveguides for increasing the gain bandwidth of integrated amplifiers. *Journal of Lightwave Technology,* vol. 25, no. 6, pp. 1613-1620, doi: 10.1109/jlt.2007.895561.

[47] Huang, W. and Syms, R. R. A. (2003). Sol-gel silica-on-silicon buried-channel EDWAs. *Journal of Lightwave Technology,* vol. 21, no. 5, pp. 1339-1349, doi: 10.1109/jlt.2003.812417.

[48] Tang, H. S. et al. (2008). A semi-weakly confined erbium-doped waveguide amplifier with double-layered buffer/cladding. *Optics Express,* vol. 16, no. 13, pp. 9844-9849, doi: 10.1364/oe.16.009844.

[49] Shen, S. X. and Jha, A. (2004). The influence of F-ion doping on the fluorescence ($^4I_{13/2}$ -> $^4I_{15/2}$) line shape broadening in Er^{3+}-doped oxyfluoride silicate glasses. *Optical Materials,* vol. 25, no. 3, pp. 321-333, doi: 10.1016/j.optmat.2003.08.006.

[50] Psaila, N. D. et al. (2007). Er : Yb-doped oxyfluoride silicate glass waveguide amplifier fabricated using femtosecond laser inscription. *Applied Physics Letters,* vol. 90, no. 13, Art no. 131102, doi: 10.1063/1.2716866.

[51] Slooff, L. H. et al. (2001). Effects of heat treatment and concentration on the luminescence properties of erbium-doped silica sol-gel films. *Journal of Non-Crystalline Solids*, vol. 296, no. 3, pp. 158-164, doi: 10.1016/s0022-3093(01)00903-6.

[52] Yan, Y. C. et al. (1997). Erbium-doped phosphate glass waveguide on silicon with 4.1 dB/cm gain at 1.535 μm. *Applied Physics Letters*, vol. 71, no. 20, pp. 2922-2924, doi: 10.1063/1.120216.

[53] Facchini, G. et al. (2001). Erbium-doped crystalline YAG planar and ridge waveguides on quartz and sapphire substrates: deposition and material characterisation. *Optical Materials*, vol. 17, no. 1-2, pp. 251-254, doi: 10.1016/s0925-3467(01)00087-8.

[54] Shmulovich, J. et al. (1992). Er^{3+} glass waveguide amplifier at 1.5 μm on silicon. *Electronics Letters*, vol. 28, no. 13, pp. 1181-1182, doi: 10.1049/el:19920746.

[55] Ghosh, R. N. et al. (1996). 8-mW threshold Er^{3+}-doped planar waveguide amplifier. *IEEE Photonics Technology Letters*, vol. 8, no. 4, pp. 518-520, doi: 10.1109/68.491212.

[56] Choi, Y. B. et al. (2000). Er-Al-codoped silicate planar light waveguide-type amplifier fabricated by radio-frequency sputtering. *Optics Letters*, vol. 25, no. 4, pp. 263-265, doi: 10.1364/ol.25.000263.

[57] Song, Q. et al. (2007). Photoluminescence enhancement in Yb^{3+}: Er^{3+} co-doped eutectic Al_2O_3 : SiO_2 thin films by 980nm excitation. *Optics Express*, vol. 15, no. 7, pp. 3948-3954, doi: 10.1364/oe.15.003948.

[58] Kondo, Y. et al. (2005). Gain characteristics of 6cm-long Er-doped bismuthate waveguide. *Electronics Letters*, vol. 41, no. 6, pp. 317-318, doi: 10.1049/el:20058075.

[59] Kitagawa, T. et al. (1992). Amplification in erbium-doped silica-based planar lightwave circuits. *Electronics Letters*, vol. 28, no. 19, pp. 1818-1819, doi: 10.1049/el:19921159.

[60] Hattori, K. et al. (1993). Erbium-doped silica-based planar waveguide amplifier pumped by 0.98 μm laser diodes. *Electronics Letters*, vol. 29, no. 4, pp. 357-359, doi: 10.1049/el:19930241.

[61] Kohls, M. et al. (1999). A simple colloidal route to planar micropatterned Er@ZnO amplifiers. *Advanced Materials,* vol. 11, no. 4, pp. 288-292, doi: 10.1002/(sici)1521-4095(199903)11:4<288::Aid-adma288>3.0.Co;2-b.

[62] Kahn, A. et al. (2008). Amplification in epitaxially grown Er:(Gd, LU)$_2$O$_3$ waveguides for active integrated optical devices. *Journal of the Optical Society of America B-Optical Physics,* vol. 25, no. 11, pp. 1850-1853, doi: 10.1364/josab.25.001850.

[63] Serna, R. and Afonso, C. N. (1996). In situ growth of optically active erbium doped Al_2O_3 thin films by pulsed laser deposition. *Applied Physics Letters,* vol. 69, no. 11, pp. 1541-1543, doi: 10.1063/1.117998.

[64] Caricato, A. P. et al. (2007). Er-doped oxyfluoride silicate thin films prepared by pulsed laser deposition. *Optical Materials,* vol. 29, no. 9, pp. 1166-1170, doi: 10.1016/j.optmat.2006.04.014.

[65] Serna, R. et al. (1998). Optically active Er-Yb doped glass films prepared by pulsed laser deposition. *Journal of Applied Physics,* vol. 84, no. 4, pp. 2352-2354, doi: 10.1063/1.368304.

[66] Hoekstra, T. H. et al. (1993). Sputter-deposited erbium-doped Y_2O_3 active optical wave-guides. *Electronics Letters,* vol. 29, no. 7, pp. 581-583, doi: 10.1049/el:19930390.

[67] Fujii, M. et al. (1997). 1.54 μm photoluminescence of Er^{3+} doped into SiO_2 films containing Si nanocrystals: Evidence for energy transfer from Si nanocrystals to Er^{3+}. *Applied Physics Letters,* vol. 71, no. 9, pp. 1198-1200, doi: 10.1063/1.119624.

[68] Daldosso, N. et al. (2006). Refractive index dependence of the absorption and emission cross sections at 1.54 μm of Er^{3+} coupled to Si nanoclusters. *Applied Physics Letters,* vol. 88, no. 16, Art no. 161901, doi: 10.1063/1.2195773.

[69] Musa, S. et al. (2000). Characteristics of Er-doped Al_2O_3 thin films deposited by reactive co-sputtering. *IEEE Journal of Quantum Electronics,* vol. 36, no. 9, pp. 1089-1097, doi: 10.1109/3.863962.

[70] Worhoff, K. et al. (2009). Reliable Low-Cost Fabrication of Low-Loss Al_2O_3:Er^{3+} Waveguides With 5.4-dB Optical Gain. *IEEE Journal of Quantum Electronics,* vol. 45, no. 5-6, pp. 454-461, doi: 10.1109/jqe.2009.2013365.

[71] Yerci, S. et al. (2010). Visible and 1.54 μm Emission From Amorphous Silicon Nitride Films by Reactive Cosputtering. *IEEE Journal of Selected Topics in Quantum Electronics,* vol. 16, no. 1, pp. 114-123, doi: 10.1109/jstqe.2009.2032516.

[72] Schermer, R. et al. (2003). Optical amplification at 1534 nm in erbium-doped zirconia waveguides. *IEEE Journal of Quantum Electronics,* vol. 39, no. 1, pp. 154-159, doi: 10.1109/jqe.2002.806163.

[73] Van, T. T. and Chang, J. P. (2005). Controlled erbium incorporation and photoluminescence of Er-doped Y_2O_3. *Applied Physics Letters,* vol. 87, no. 1, Art no. 011907, doi: 10.1063/1.1984082.

[74] Solehmainen, K. et al. (2004). Erbium-doped waveguides fabricated with atomic layer deposition method. *IEEE Photonics Technology Letters,* vol. 16, no. 1, pp. 194-196, doi: 10.1109/lpt.2003.820484.

[75] Lin, C. H. et al. (1997). Preparation and characterization of aluminum oxide films by plasma enhanced chemical vapor deposition. *Surface & Coatings Technology,* vol. 90, no. 1-2, pp. 102-106, doi: 10.1016/s0257-8972(96)03100-3.

[76] He, G. and Sun, Z. (2012). *High-k gate dielectrics for CMOS technology*. John Wiley & Sons.

[77] Hu, B. F. et al. (2014). Optical properties of amorphous Al_2O_3 thin films prepared by a sol-gel process. *Ceramics International,* vol. 40, no. 9, pp. 14133-14139, doi: 10.1016/j.ceramint.2014.05.148.

[78] Zhang, L. et al. (2007). Annealing of Al_2O_3 thin films prepared by atomic layer deposition. *Journal of Physics D-Applied Physics,* vol. 40, no. 12, pp. 3707-3713, doi: 10.1088/0022-3727/40/12/025.

[79] Sohler, W. et al. (2005). Erbium-doped lithium niobate waveguide lasers. *IEICE transactions on electronics,* vol. 88, no. 5, pp. 990-997.

[80] Waldmann, M. et al. (2008). Erbium-doped fluoride glass waveguides. *Electronics Letters,* vol. 44, no. 20, pp. 1193-1195, doi: 10.1049/el:20081912.

[81] Mackenzie, J. I. et al. (2012). Er-doped Tellurite glasses for planar waveguide power amplifier with extended gain bandwidth, in *Solid State Lasers Xxi: Technology and Devices,* vol. 8235, W. A. Clarkson and R. K. Shori Eds., (Proceedings of SPIE.

[82] Li, S. F. et al. (2002). A numerical analysis of gain characteristics of Er-doped Al_2O_3 waveguide amplifiers. *Optical and Quantum Electronics,* vol. 34, no. 9, pp. 859-866, doi: 10.1023/a:1019923415661.

[83] Kik, P. G. and Polman, A. (2003). Cooperative upconversion as the gain-limiting factor in Er doped miniature Al_2O_3 optical waveguide amplifiers. *Journal of Applied Physics,* vol. 93, no. 9, pp. 5008-5012, doi: 10.1063/1.1565697.

[84] Bradley, J. D. B. and Pollnau, M. (2011). Erbium-doped integrated waveguide amplifiers and lasers. *Laser & Photonics Reviews,* vol. 5, no. 3, pp. 368-403, doi: 10.1002/lpor.201000015.

[85] Bradley, J. D. B. et al. (2010). Gain bandwidth of 80 nm and 2 dB/cm peak gain in Al_2O_3:Er^{3+} optical amplifiers on silicon. *Journal of the Optical Society of America B-Optical Physics,* vol. 27, no. 2, pp. 187-196, doi: 10.1364/josab.27.000187.

[86] Hattori, K. et al. (1998). Optical and structural properties of Er^{3+}-doped P_2O_5-SiO_2 and Al_2O_3-SiO_2 planar waveguides. *Materials Science and Engineering B-Solid State Materials for Advanced Technology,* vol. 54, no. 1-2, pp. 15-17, doi: 10.1016/s0921-5107(98)00118-4.

[87] Xiang, Q. et al. (2000). Optical properties of Er^{3+}-doped SiO_2-GeO_2-Al_2O_3 planar waveguide fabricated by sol-gel processes. *Thin Solid Films,* vol. 370, no. 1-2, pp. 243-247, doi: 10.1016/s0040-6090(00)00915-9.

[88] Camy, P. et al. (1996). Ion-exchanged planar lossless splitter at 1.5 μm. *Electronics Letters,* vol. 32, no. 4, pp. 321-323, doi: 10.1049/el:19960267.

[89] He, Z. et al. (2006). Er^{3+}/Yb^{3+} co-doped waveguide amplifier and lossless power splitter fabricated by a two-step ion exchange on a commercial phosphate glass. *Journal of the Korean Physical Society,* vol. 49, no. 5, pp. 2159-2163.

[90] Sckerl, M. W. et al. (Year), Loss-less planar waveguide 1: 4 power splitter at 1550 nm, in *25th European Conference on Optical Communication*, 1999.

[91] Jaouen, Y. et al. (1999). Eight-wavelength Er-Yb doped amplifier: Combiner/splitter planar integrated module. *IEEE Photonics Technology Letters,* vol. 11, no. 9, pp. 1105-1107, doi: 10.1109/68.784202.

[92] Peters, P. M. et al. (1999). Ion-exchanged waveguide lasers in Er^{3+}/Yb^{3+} codoped silicate glass. *Applied Optics,* vol. 38, no. 33, pp. 6879-6886, doi: 10.1364/ao.38.006879.

[93] Veasey, D. L. et al. (1999). Arrays of distributed-Bragg-reflector waveguide lasers at 1536 nm in Yb/Er codoped phosphate glass. *Applied Physics Letters,* vol. 74, no. 6, pp. 789-791, doi: 10.1063/1.123368.

[94] Sorbello, G. et al. (2001). Singlemode Er : Yb waveguide laser array at 1.5 μm. *Electronics Letters,* vol. 37, no. 16, pp. 1014-1015, doi: 10.1049/el:20010679.

[95] Feuchter, T. et al. (1992). Erbium-doped ion-exchanged wave-guide lasers in BK-7 glass. *IEEE Photonics Technology Letters,* vol. 4, no. 6, pp. 542-544, doi: 10.1109/68.141961.

[96] Demirtas, M. et al. (2018). Low Loss Atomic Layer Deposited Al2O3 Waveguides for Applications in On-Chip Optical Amplifiers. *Ieee Journal of Selected Topics in Quantum Electronics,* vol. 24, no. 4, Art no. 3100508, doi: 10.1109/jstqe.2018.2825880.

[97] MetriconCorporation, "Metricon Models 2010 and 2010/M Prism Coupler Operation and Maintenance Guide," Pennington, New Jersey, USA, 2003.

[98] Aslan, M. M. et al. (2010). Low-loss optical waveguides for the near ultra-violet and visible spectral regions with Al_2O_3 thin films from atomic layer deposition. *Thin Solid Films,* vol. 518, no. 17, pp. 4935-4940, doi: 10.1016/j.tsf.2010.03.011.

[99] Kassim, N. M. et al. (2004). *Single mode rib optical waveguide modeling techniques* (2004 RF and Microwave Conference, RFM 2004, Proceedings). pp. 272-276.

[100] Demirtas, M. et al. (2016). Extensive mode mapping and novel polarization filter design for ALD grown Al_2O_3 ridge waveguides. *Optical and Quantum Electronics,* vol. 48, no. 7, Art no. 357, doi: 10.1007/s11082-016-0629-4.

[101] Ozden, A. et al. (2015). Polarization insensitive single mode Al_2O_3 rib waveguide design for applications in active and passive optical waveguides. *Journal of the European Optical Society-Rapid Publications,* vol. 10, Art no. 15005, doi: 10.2971/jeos.2015.15005.

[102] Ronn, J. et al. (2016). Atomic Layer Engineering of Er-Ion Distribution in Highly Doped Er:Al_2O_3 for Photoluminescence Enhancement. *Acs Photonics,* vol. 3, no. 11, pp. 2040-2048, doi: 10.1021/acsphotonics.6b00283.

[103] Dingemans, G. et al. (2011). Er^{3+} and Si luminescence of atomic layer deposited Er-doped Al_2O_3 thin films on Si(100). *Journal of Applied Physics,* vol. 109, no. 11, Art no. 113107, doi: 10.1063/1.3595691.

[104] Paivasaari, J. et al. (2005). High growth rate of erbium oxide thin films in atomic layer deposition from (CpMe)(3)Er and water precursors. *Chemical Vapor Deposition*, vol. 11, no. 10, pp. 415-419, doi: 10.1002/cvde.200506396.

[105] Paivasaari, J. et al. (2004). Atomic layer deposition of rare earth oxides: erbium oxide thin films from beta-diketonate and ozone precursors. *Journal of Alloys and Compounds*, vol. 374, no. 1-2, pp. 124-128, doi: 10.1016/j.jallcom.2003.11.149.

[106] Blauwendraat, T. (2007). Characterization of sputtered Er:Al_2O_3 for active integrated optics. M.Sc. Thesis, University of Twente.